ISSN 2367-7570

Workshop
"Solar Influences on the Magnetosphere, Ionosphere and Atmosphere"

Book of Proceedings

Fourteenth Workshop
June, 2022

Organized by:
Space Research and Technologies Institute
Bulgarian Academy of Sciences

Editorial Board

Editors: **Katya Georgieva, Boian Kirov, Simeon Asenovski**

Acknowledgements

The Workshop's organizers acknowledge the support by the Bulgarian National Science Fund, Grant No KP-06-MNF/2, SCOSTEP/PRESTO scientific program, and the Bulgarian Academy of Sciences.

Scientific Organizing Committee

P r e f a c e

The Fourteenth Workshop "Solar Influences on the Magnetosphere, Ionosphere and Atmosphere" was held from June 6 to 10, 2022 in Primorsko, Bulgaria. 52 scientists from 12 countries participated in the workshop with 50 oral and poster presentations. 12 papers are included in these Proceedings.

The Scientific Organizing Committee and the Editors of the Proceedings thank all the participants in the Workshop and contributors to the Proceedings.

DOI: 10.31401/WS.2022.proc

CONTENT

Data Processing

Pre-Earthquake Anomalies in the Ionospheric and Geomagnetic Parameters

Adibekyan M.V.

Ministry of Emergency Situations of the Republic of Armenia Territorial Survey for Seismic Protection State Non-Commercial Organization
e-mail: adibekyan@yahoo.com

Abstract

Aiming at earthquake precursors apportionment the earthquake preparation displays of ERZRUM (Turkey, 28.03.2004, M=5.4) and NOEMBERYAN (Armenia, 20.06.2008, M = 3.4), earthquakes in time-series have been studied using the geomagnetic and ionosphere tools. Aiming at earthquake forecasting the anomaly in the ionosphere plasma is investigated by radio - astronomical method. There were received some results, allowing to make out the difference of seism genic anomalies of ionosphere between the longer anomalies connected to magnetic activity of ionosphere by the method of vertical reconnaissance of ionosphere. For the analysis of geomagnetic time-series used Pushkov's method. Results of the analysis observation have confirmed communication between earthquakes magnitude M > 3.0 and between and geomagnetic parameters. Have been investigated earthquakes of Noyemberyan (Armenia, 20.06.2008, M = 3.4). Have been used geomagnetic stations of observation Artik, Aruch and Djermuk. There have been used the time–series Saravand ionospheric station.

Keywords: Earthquake, precursors, ionosphere, time-series, geomagnetic

Introduction

It is known, that the geophysical environment, including seismically active zones, is made up of solid, liquid and gaseous phases. It is known as well that in the zone of two phases separation a Zone of Separated Changes (ZSC) is forming, or as they are called in physical chemistry, double ionic (electric) layers. Depending on their structure, each of the ZSC of geophysical environment is characterized by capacity inductivity and resistance [Balassanian, 1990].

The results obtained earlier allow to make out the difference between activity of ionosphere, by the method of vertical reconnaissance of ionosphere.

Radio astronomical monitoring method makes possible, along with immediate detection of electromagnetic emission from the Earth's depth in the selected frequency band, to observe other types of lithospheric impact on the atmosphere, such as aerosol, electrostatic, acoustical/gravitational, etc. Those sources ultimately create anomalies at different altitudes of the atmosphere, high affect the propagating radio astronomical signal. Radio astronomical monitoring method has the following clear advantages over the active sensing methods:

1) Cosmic radio sources (Galactic background, discrete radio stars, etc.) are used instead of man made radiation sources, often powerful, which are able to affect the observed layers of atmosphere;

2) Cosmic radio sources generate noise-like signals, which makes possible observation of the same source at several wavelengths (this is increasing the informative ness of monitoring);

3) Since the signals from the stellar radio sources pass through all layers of the atmosphere, their informative ness is high;

4) The radio astronomical instruments are highly sensitive and able to detect the smallest changes in the state of the atmosphere;

5) The method allows monitoring of solar activity by direct measurement of solar radiation density in the receiver waveband;

6) The cosmic source's power in the radio-frequencies range (over 10 MHz) is stable and known with high accuracy, while stability of the receiver system is provided by a controlled noise power source. This configuration allows reception of signals from point cosmic radio sources Swan and Cassiopeia-A, with nearly the same amplitudes of interference lobes. Time interval between these sources by the local meridian is 3 hours and 30 min.

The method and technique of research

A new Methodology has been elaborated that provides possibility to estimate the current Seismic hazard (its intensity, location and time) with a sufficiently big probability. The elaborated methodology was used for analysis of data received in the process of perpendicular ionosphere from "Swan- A" and "Cassiopeia - A" point radio sources by radio astronomy methods. The time – series of geomagnetic field tension of T full vector. Aiming at the earthquake forecasting the anomaly formations in the ionospheric plasma are investigated by a radio-astronomical method. For considering the geomagnetic field, the high accuracy proton magnetometers, which are measuring the T inductivity of geomagnetic field each 5 minutes are used for measuring the geomagnetic field [Badalyan, Petrosyan, Adibekyan. 2001]. This methodology has been used in an earlier study of the earthquakes in VARDENIS (Armenia, 29.04.2008, M=3.7) BORISAKHO (Georgia, 09.06.08, M =4.1) and NAKHITCEVAN (Azerbaijan, 02.09.2008, M=5.1) [Adibekyan, 2021]. Here we apply it for the ERZRUM (Turkey, 28.03.2004, M=5.4) and NOEMBERYAN (Armenia, 20.06.2008, M = 3.4) earthquakes.

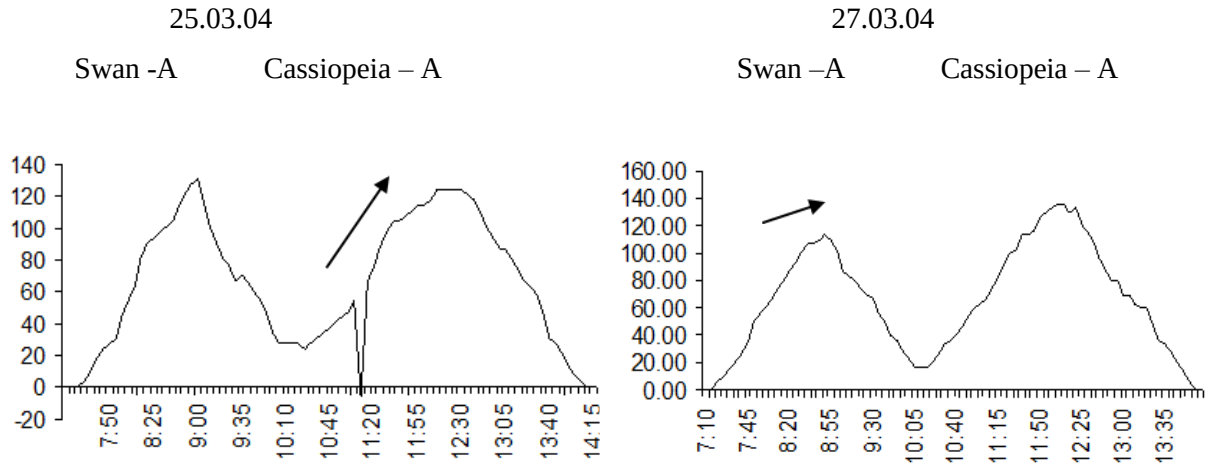

Fig.1. The time – series of the ionosphere field (Saravand station) obtained by Radio astronomic method for the ERZRUM (Turkey, 28.03.2004, M=5.4) earthquake.

Fig.2. The time – series of the geomagnetic fields (Aruch-Artik, Djermuk-Artik stations) for the Noyemberyan (Armenia, 20.06.2008, M = 3.4) earthquake.

Results

The results of the retrospective analysis of ionosphere observation data before ERZRUM (Turkey, 28.03.2004, M=5.4), revealed the following basic types of anomaly (Figure 1):

1. Blinking of ionosphere active radio-source Swan – A on the frequency of 74 MHz.
2. Anomaly of above – mentioned precursors is coming out up to 40 days before earthquake (Figure 2).

Conclusion

The results of analysis by used methods confirm the conclusion of [Adibekyan, 2021] that the anomalies generally appear on 1- 40 days before the earthquake.

References

Adibekyan M.V. (2021) Analyse of ionospheric and Geomagnetic Pre -earthquake Anomalies. Proceedings of the Thirteenth Workshop "Solar Influences on the Magnetosphere, Ionosphere and Atmosphere", September, 2021, p.1-3

Badalyan M., Petrosyan. H., Adibekyan M.V. (2001) Peculiarities of Magnetic Precursors of Earthquakes on the Territory of Armenia.Journal of Georgian Geophysical Society.Physics of SolidEarth, vol.5, Tbilisi, p.37-43, 2001.

Balassanian S. (1990), Dynamic Geo-electricity. Novosibirsk, "NAUKA", Siberian Department, pp.232.

Temporal and Latitudinal Distribution of anti-Hale Active Regions in the Synthetic Solar Cycle

Zhukova A.V.[1], *Khlystova A.I.*[2], *Abramenko V.I.*[1], *1, Sokoloff D.D.*[3,4,5]

[1] Crimean Astrophysical Observatory RAS, Nauchny, Russia;
[2] Institute of Solar-Terrestrial Physics SB RAS, Irkutsk, Russia;
[3] Department of Physics, Lomonosov Moscow State University, Moscow, Russia
[4] Moscow Center of Fundamental and Applied Mathematics, Moscow, Russia
[5] Pushkov Institute of Terrestrial Magnetism, Ionosphere and Radio Wave Propagation RAS, Troitsk, Moscow, Russia
E-mail: anastasiya.v.zhukova@gmail.com

1. Abstract.

The polarity of leading sunspots in active regions (ARs) is determined by the direction of the toroidal component of the global solar magnetic field. The vast majority of bipolar ARs have the certain leading sunspot polarity in accordance with the Hale’s polarity law, whereas some ARs have the opposite polarity (anti-Hale ARs). The number of such groups is relatively small (about 4%), which complicates some important tests. The data on 14838 ARs (including 367 anti-Hale groups) related to five 11-yr cycles (16–18 and 23, 24) were combined in a synthetic cycle of unique time length and latitudinal width. A specific routine was created for this purpose. Our analysis of the synthetic cycle shown that anti-Hale ARs follow the cycle and their time-latitude distribution quite uniform, which implies their genetic connection with the global dynamo. The higher values of anti-Hale ARs percentage near the equator may be explained by the misalignment between the magnetic and heliographic equators. The increase in the number and percentage of anti-Hale ARs that occurs in the second part of the cycle might indicate the relationship with the process of the polar field reversal. The increase in the percentage that found in the solar minimum and at the edges of the butterfly diagram (zones where the magnetic field is weakened) might indicate facilitation of the processes that distort flux tubes during their rising through the convection zone. In addition, the synthetic cycle compilation method might be used for studying other magnetic activity tracers with poor statistics.

Keywords: solar cycle; solar active regions; solar magnetic fields.

2. Introduction

The magnetic cycle models explain the phenomenon of the solar activity, however some aspects are not fully understood. According to modern concepts based on the classical models [*Parker,* 1955; *Babcock,* 1961], the solar magnetic fields generation implies the mutual transformation of the poloidal and toroidal components of the global solar magnetic field occurring inside the convection zone with approximate period of 11-yr. In each given solar cycle (SC), it is the direction of the toroidal field that determines the characteristics of active regions (ARs) that appear on the solar surface. In accordance with the Hale polarity law [*Hale et al.,* 1919], in even cycles, the bipolar ARs have the negative polarity of the leading sunspots in the north and positive in the south hemispheres; the polarity in the odd cycles is opposite. The appearance of ARs violating this rule (anti-Hale ARs) does not fit into the framework of the magnetic cycle models and cannot be explained by the global dynamo action in terms of the mean field dynamo theory [*Krause and Rädler, 1980*]. Note that ARs with violations from other empirical rules for sunspots groups (for example, Joy's law) are not considered here.

However, some essential tests cannot be carried out for anti-Hale ARs, since the relatively small number of such ARs does not provide the sufficient reliability of statistical studies. The relative number of anti-Hale groups is reported of about 4% by the authors, who tested each AR individually (see *Zhukova et. al.*, 2020 and references therein); the same results were shown in some studies on the base of automatic ARs extraction algorithms [*Stenflo and Kosovichev,* 2012]. To overcome the anti-Hale ARs statistical limitations, we propose combining the available data on the anti-Hale groups of five SCs (16–18 and 23, 24). Thus, the purpose of this work is to form a sample sufficient for a meaningful study of the time-latitude distribution of anti-Hale ARs.

3. Data and method

As data source on anti-Hale ARs of SCs 23 and 24, we used the Catalogue of bipolar ARs violating the Hale polarity law from 1989 to 2018 [*Zhukova et al.*, 2020], and its prolongation (2019–2020) at http://sun.crao.ru/databases/catalog-anti-hale. We also used the Summary of Mount Wilson magnetic observations of sun-spots (SMWMO) as the source of the information about reverse-polarity ARs for the period from 1925 to 1958 (SCs 16–18). The Summary was published in the Publications of the Astronomical Society of the Pacific. The SMWMO data are available in digital form at http://iopscience.iop.org/journal/1538-3873. Data on all ARs observed on the disk during these periods were obtained from the USAF/NOAA Solar Region Summary (SRS) at http://solarcyclescience.com.

The first task was to determine a hosting SC for each individual AR (the groups of both the preceding and following cycles appear on the disc simultaneously in the solar minimum). To define the boundaries between the cycles, we used the USAF/NOAA SRS data and the method proposed by *McClintock et al.* [*2014*]. The next task was to combine the cycles, taking into account their different duration and amplitude. Butterfly wings of different cycles don't match well as it is shown in Figure 1 (left panel) for SCs 23, 17. However, the cycles are known to be similar and can be stretched or compressed [*Hathaway,* 2015]. We performed a linear transformation of each of the separated cycles in both time and latitude coordinates so that the wings match (Figure 1, right panel). The moment when ARs of the cycle begin to emerge regularly (at least two or three ARs per month) was accepted as the zero-point T0. The equatorial line was accepted as the natural latitude divider and was marked as L0. The lines T1 and L1 bound the SC 23, whereas the lines T2 and L2 outline the SC 17.

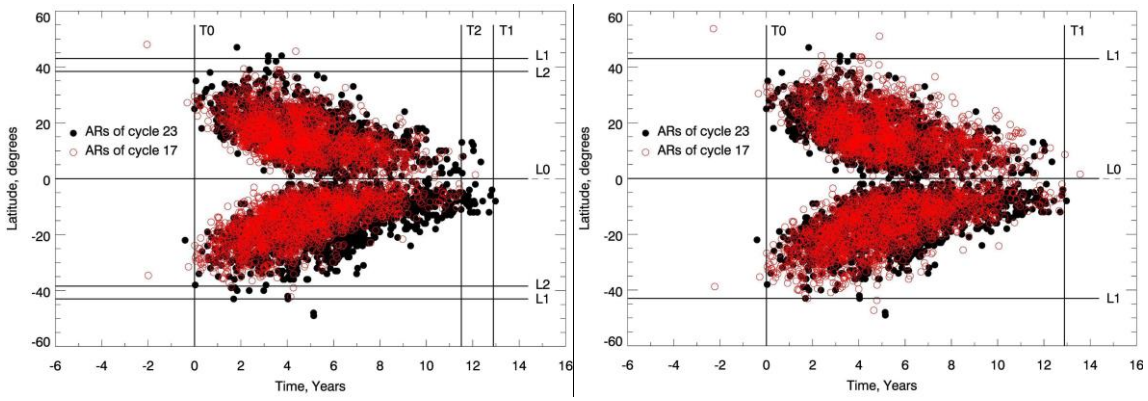

Figure 1. *Overlapping of ARs of SCs 23 (black) and 17(red) before (left panel) and after (right panel) the linear transformation.*

The same routine was also performed for the rest three cycles. More details can be found in *Zhukova et al.* [*2022*].

4. Results

The temporal variations of ARs in the synthetic cycle are presented in Figure 2. The beginning and end of the synthetic cycle correspond to the period of the real SCs overlapping (when low-latitude ARs of the previous cycle and high-latitude ARs of the following cycle appear on the disk simultaneously). Since that the duration of the synthetic cycle is slightly longer than 11 years (about 13 years). One can see that anti-Hale ARs follow the cycle, which implies their mutual connection with the global dynamo and organized toroidal flux system in the convection zone.

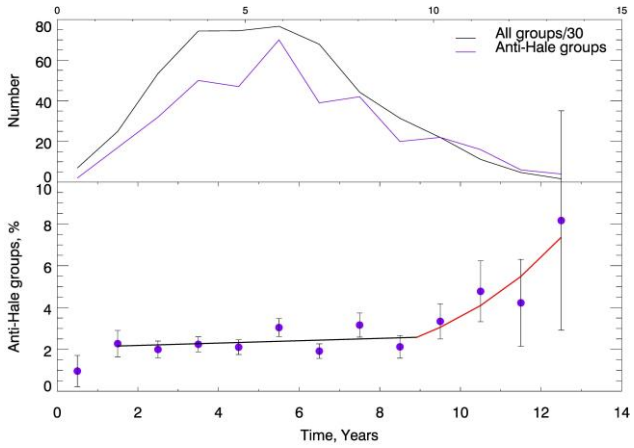

Figure 2. *Temporal variations of all ARs (thin black line) and anti-Hale groups (violet line) in the synthetic cycle (top panel). Yearly values of the relative number of Anti-Hale ARs are shown with violet circles (bottom panel). Thick black and red lines represent the fitting with linear and exponential functions, respectively.*

We also performed the coupling of two identical individual synthetic cycles, placing them one after the other (Figure 3). It allowed us to simulate the adjunction of cycles in the solar minima. We used different overlap intervals (one, two, three years). The intervals of one (Figure 3, left panel) and two (Figure 3, right panel) years are consistent with the real pattern for SCs, as it is following from the typical butterfly diagrams. Using both overlap intervals showed the peaks in the anti-Hale ARs percentage in the simulated minimum, which is consistent with findings by *McClintock et al.* [2014]; *Sokoloff et al*. [2015]. The increase in the anti-Hale ARs percentage in solar minima is interpreted by the authors of these works in different ways. *McClintock et al.* [2014] associated this phenomenon with misalignment between the magnetic and heliographic equators. At the same time, *Sokoloff et al.* [2015] discussed a possible small-scale cycle-independent dynamo action. Their idea was that such a process could be noticed at intervals when the global dynamo action is least pronounced.

The time-latitude distribution of anti-Hale ARs and their relative number in the synthetic cycle are presented in Figure 4 (left and right panels, respectively). It can be noticed that the fraction of anti-Hale groups is increased near the equator. This supports the hypothesis of the misalignment between the magnetic and heliographic equators [*McClintock et al.*, 2014]. Such a misalignment was found earlier by [*Zolotova et al.*, 2009]. However, the increase in the anti-Hale ARs percentage is also observed on different latitudes near the oncoming solar minimum.

It might be the evidence of the more complex shape of the equator, which was reported by [*Obridko et al.*, 2011].

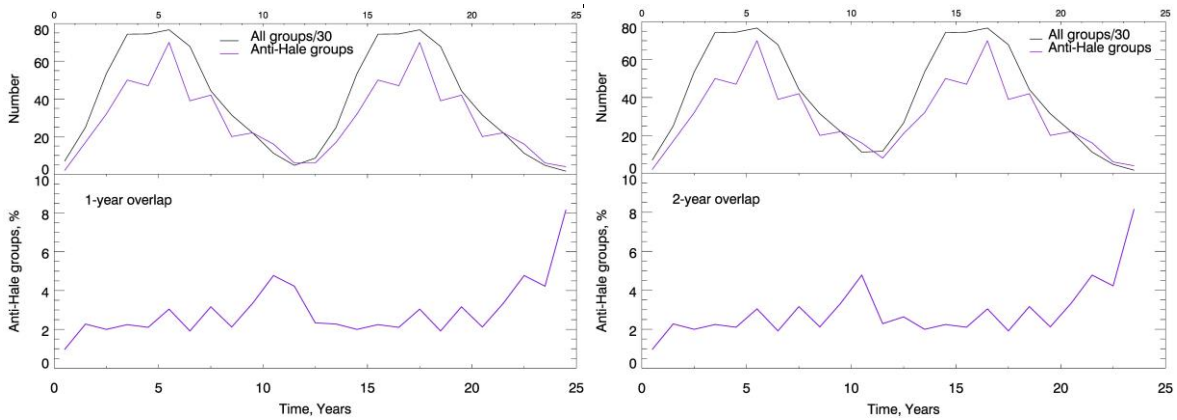

Figure 3. *Temporal variations of ARs in the doubled synthetic cycle with different overlapping intervals: one (left panel) and two (right panel) years.*

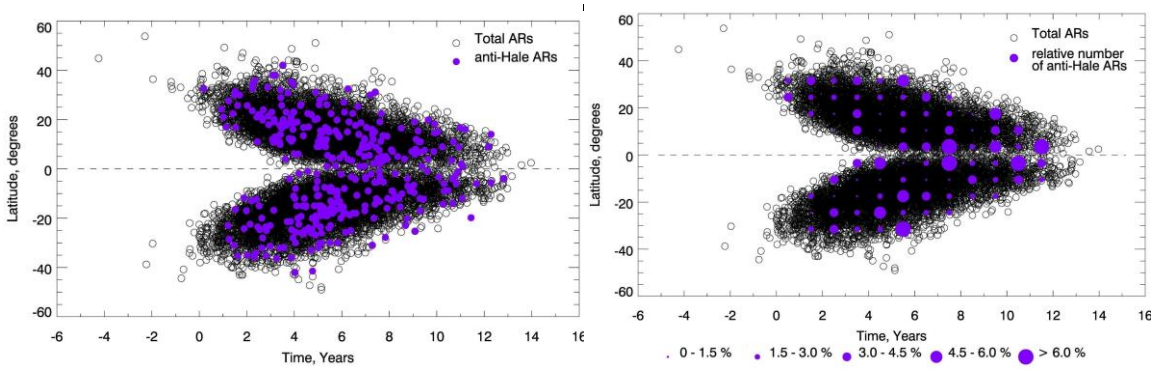

Figure 4. *Time-latitude distribution of ARs in the synthetic cycle: anti-Hale ARs (left panel), the relative number of anti-Hale ARs (right panel).*

We also found the increase in the anti-Hale ARs relative number at the edges of the butterfly diagram. The interval near the oncoming minimum is a zone of the weakening of the toroidal field and the smallest activity of the global dynamo, which was discussed by [*Sokoloff et al.*, 2015*; Abramenko et al.,* 2018]. The edges of the diagram are also implies the weakened field. We can assume that the weakening and loss of regularity of the toroidal field facilitate the manifestation of the mechanism(s) that distort magnetic flux tubes of ARs during their rising through the convection zone. Strong convective flows and magnetic field fluctuations and, hence, the turbulent component of the dynamo can cause the distortion of tubes [*Abramenko,* 2021].

Recall that the beginning and end of the synthetic cycle correspond to the period of the real SCs overlapping and relate to the solar minimum. At the beginning of the cycle, the fraction of anti-Hale ARs is very small, whereas at the end of the cycle the anti-Hale ARs percentage is increased (Figures 2, 4). We speculate that the strong regular toroidal field of the new cycle pushes to the surface the weakened toroidal field of the old cycle at that period, which leads to the increase in the anti-Hale ARs percentage.

In generally, the increase in the number and percentage of anti-Hale ARs occurs in the second part of the cycle, which is consistent with the idea of the relationship of the reverse-polarity ARs and the process of the polar field reversal [*Mordvinov et al.,* 2022].

5. Conclusions

Based on the results obtained we make the following conclusions:

1. The temporal variations of anti-Hale ARs are consistent with the cycle progress, which implies the genetic relationship with the global dynamo and the toroidal flux system in the convection zone.
2. The temporal variations of the relative number of anti-Hale ARs show the peak in the minimum simulated by the coupling of two identical individual synthetic cycles, which might mean the weakening of the produced by the global dynamo toroidal field and intervention mechanism(s) that distort magnetic flux tubes of ARs during their rising through the convection zone (for instance, the turbulent component of the dynamo).
3. The time-latitude distribution of the relative number of anti-Hale ARs shown the increase in the edges of the butterfly diagram and near the oncoming minimum of the synthetic cycle (zones of the weakening of the toroidal field), which might indicate facilitation of the mechanism(s) that distort magnetic flux tubes of ARs.
4. The increase in the anti-Hale ARs relative number near the equator at different latitudes might mean a displacement of the magnetic equator relative to the heliographic equator and, moreover, a complex shape of the magnetic equator.

The synthetic cycle compilation method might be used for studying the time-latitude distribution of other magnetic activity tracers with poor statistics (not only anti-Hale ARs).

Acknowledgment

This study is supported by the Russian Science Foundation (project 18-12-00131).

References

Abramenko V.I., Zhukova A.V., Kutsenko A.S. (2018). Contributions from Different-Type Active Regions Into the Total Solar Unsigned Magnetic Flux, Geomagn. and Aeronomy, Vol 58, No 8, pp.1159-1169, DOI: 10.1134/S0016793218080224.

Abramenko V. (2021). Signature of the turbulent component of the solar dynamo on active region scales and its association with flaring activity, Mon. Not. Royal Astron. Soc., Vol 507, Is 3, pp. 3698-3706, DOI: 10.1093/mnras/stab2404.

Babcock H.W. (1961). The topology of the Sun’s magnetic field and the 22-YEAR cycle, Astrophys. J., Vol 133, pp. 572-587, DOI: 10.1086/147060.

Hale G. E., Ellerman F., Nicholson S. B., Joy A. H. (1919). The Magnetic Polarity of Sun-Spots, Astrophys. J., Vol 49, pp. 153-185, DOI: 10.1086/142452.

Hathaway D. H. (2015). The Solar Cycle, Liv. Rev. in Solar Phys., Vol 12, Is 1, article id. 4, 87 pp., DOI: 10.1007/lrsp-2015-4.

Krause F., Rädler K.-H. (1980). Mean-field magnetohydrodynamics and dynamo theory, Oxford: Pergamon Press.

McClintock B.H., Norton A.A., Li J. (2014). Re-examining Sunspot Tilt Angle to Include Anti-Hale Statistics, Astrophys. J., Vol 797, Is 2, article id. 130, 10 pp., DOI: 10.1088/0004-637X/797/2/130.

Mordvinov A.V., Karak, B. B., Banerjee D, Golubeva E., Khlystova A.I., Zhukova A. V., Kumar P. (2022). Mon. Not. Royal Astron. Soc., Vol 510, Is 1, pp. 1331-1339, DOI: 10.1093/mnras/stab3528.

Obridko V.N., Chertoprud V.E., Ivanov E.V. (2011). `Active Longitudes' in the Heliomagnetic Reference Frame, Solar Phys., Vol 272, Is 1, pp. 59-71, DOI: 10.1007/s11207-011-9813-7.

Parker E.N. (1955). Hydromagnetic Dynamo Models, Astrophys. J., Vol 122, pp. 293-314, DOI: 10.1086/146087.

Sokoloff D., Khlystova A., Abramenko V. (2015). Solar small-scale dynamo and polarity of sunspot groups, Mon. Not. Royal Astron. Soc., Vol 451, Is 2, p.p. 1522-1527, DOI: 10.1093/mnras/stv1036.

Stenflo J.O., Kosovichev A.G. (2012). Bipolar Magnetic Regions on the Sun: Global Analysis of the SOHO/MDI Data Set, Astrophys. J., Vol 745, Is 2, article id. 129, 12 pp., DOI: 10.1088/0004-637X/745/2/129.

Zhukova A., Khlystova A., Abramenko V., Sokoloff D. (2020). A Catalog of Bipolar Active Regions Violating the Hale Polarity Law, 1989 – 2018, Solar Phys., Vol 295, Is 12, article id. 165, 16 pp., DOI: 10.1007/s11207-020-01734-9.

Zhukova A., Khlystova A., Abramenko V., Sokoloff D. (2022). Synthetic solar cycle for active regions violating the Hale's polarity law, Mon. Not. Royal Astron. Soc., Vol 512, Is. 1, pp. 1365-1370, DOI: 10.1093/mnras/stac597.

Zolotova N. V., Ponyavin D. I., Marwan N., Kurths, J. (2009). Long-term asymmetry in the wings of the butterfly diagram, Astron. and Astrophys., Vol 503, Is 1, pp. 197-201, DOI: 10.1051/0004-6361/200811430.

Supersubstorm on 20 December 2015: Spatial Geomagnetic Effects

Despirak I.V.[1], Lubchich A.A.[1], Kleimenova N.G.[1], Setsko P.V.[1], Werner R.[3]

[1]Polar Geophysical Institute, Apatity, Russia; e-mail: despirak@gmail.com
[2]Schmidt Institute of Physics of the Earth, RAS, Moscow, Russia
[3]Space Research and Technology Institute, BAS, Stara Zagora Department, Bulgaria

Abstract

We analyzed the supersubstorm (SML- index ~2100 nT) observed on December 20, 2015 (onset at ~ 16:10 UT) during the intense magnetic storm caused by the magnetic cloud (MC), which included a stable southward Bz IMF direction. It is shown that the ionospheric currents, corresponding to this supersubstorm, developed on a global scale, from the evening to the late morning sectors. During its development, the very intense westward electrojet was observed with the maximum in the morning sector (~06 MLT). In the evening sector (~18 MLT), the strong eastward electrojet was observed. During the expansion phase of the substorm in the evening sector, variations in the magnetic field were observed, corresponding to the appearance of an additional current wedge in the opposite direction. The development of the substorm was accompanied by the appearance of a large positive variation in the X component of the magnetic field at geomagnetic latitudes from ~60° to ~50°, which could lead to the observed pulse of the MPB index (Midlatitude Positive Bay index). Thus, this supersubstorm demonstrated its global behavior accompanied an addition substorm current wedge development.

Keywords: solar wind**,** supersubstorm, substorm current wedge, MPB index

1. Introduction

Our work is devoted to the study of spatial geomagnetic effects of substorms as important elements of the space weather. It is known that the westward electrojet occurs in the night side during the expansion phase. This electrojet is a part of substorm current wedge (SCW), the classical picture of SCW presented in the Figure 1a. The large-scale current pattern was obtained by analysis of the magnetic disturbances at the mid-latitudes [McPheron et al. 1973; Horning et al. 1974]. This system is called the "substorm current wedge" because of its form in a polar projection (Fig.1a). In its simplest form, a model of the SCW consists of a single loop with line currents into and out of the ionosphere (on dipole field lines connected by a westward ionospheric line current and by an eastward magnetospheric line current). The SWC produces a distinctive pattern of changes in the ground-based magnetic field components, as shown in the Figure 1b [Kepko et al. 2015]. North component of the magnetic field (H) is positive and symmetric about the central meridian of the SCW, while the East component (D) is antisymmetric. In the northern hemisphere the D- component is positive premidnight and negative postmidnight. Note, that for estimation of the SCW intensity was introduced a new index – the mid-latitude positive bay index (MPB- index), which calculated by magnetic field variations at mid-latitudes [McPherron and Chu. 2016, 2018].

In our work we considered some peculiarities in the electojets development during one event of very intense substorm, so-called supersubstorm (SSS). First the term of "supersubstorms" was introduced by investigations of intense magnetic substorms by data of the SuperMag magnetometers network, the events with high negative values of SML index (< - 2500 nT) were called "supersubstorms" [Tsurutani et al. 2015]. The purpose of this work is the analysis of spatial geomagnetic effects and possible mid-latitudes magnetic effects during supersubstorm on 20 December 2015 (SML index ~ -2100 nT).

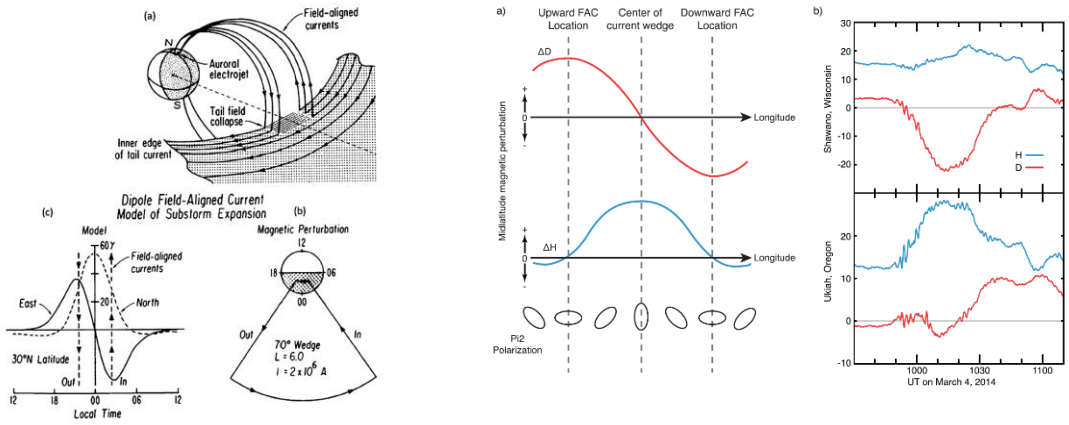

a) **b)**

F**igure 1**. *(a) dipole field-aligned current model of substorm expansion and ground-based magnetic perturbations (picture was taken from McPherron et al. 1973); (b) schematic pattern in the H- and D-components development as a result of SCW (picture was taken from Kepko et al. 2015)*

2. Data

The solar wind and IMF parameters are taken from OMNI database ftp://ftp.iki.rssi.ru/omni/ and the catalog of large-scale solar wind types ftp://ftp.iki.rssi.ru/pub/omni/catalog. Global magnetometer networks SuperMAG and IMAGE data were used for determination of the substorm development as at the midlatitudes well as at auroral latitudes. The IMAGE magnetometer data are taken from http://space.fmi.fi/image/. The global spatial distribution of electrojets was determined from the maps of magnetic field vectors obtained on the SuperMAG network. SML- index is taken from http://supermag.jhuapl.edu/. MPB index is taken from the Chu list (McPherron and Chu [2018]). To study the global distribution of ionospheric currents during SSS, we used magnetic registration data from 66 communication satellites of the AMPERE project (http://ampere.jhuapl.edu/products) as the maps of the distribution of geomagnetic disturbances summarized in 10 min with 2 min shift and the results of a spherical harmonic analysis of magnetic measurements.

3. Solar wind and IMF conditions

Figure 2 shown the variations of solar wind and interplanetary magnetic field (IMF) parameters and some geomagnetic indices on 20 December, 2015. It is seen that two consecutive structures in the solar wind were observed: SHEATH and magnetic cloud (MC). It is seen the passage of a magnetic cloud past the Earth, in front of MC there is a plasma compression region (SHEATH). Besides, solar wind was relatively slow, the speed does not exceed 500 km/s. In this event, a very high values of the solar wind density and dynamic pressure were registered. A stably negative Bz component of the magnetic field observed in the magnetic cloud (drops to -19 nT). As a result, the intense magnetic storm developed (SYM/H was -170 nT). Several substorms were observed during this magnetic storm. During one of them, at 16:13 UT, the SML index reach ~-2100 nT. At the Figure 2b the period on December 20, 2015 presented in more detail. It is seen, that before SSS the high values of the southern Bz component of the IMF (~-15 nT) were observed, By component of the IMF was positive, solar wind velocity was low (~400 km/s). Three peaks of MPB index were registered, first of them (~ 4000nT^2) correspond to SSS.

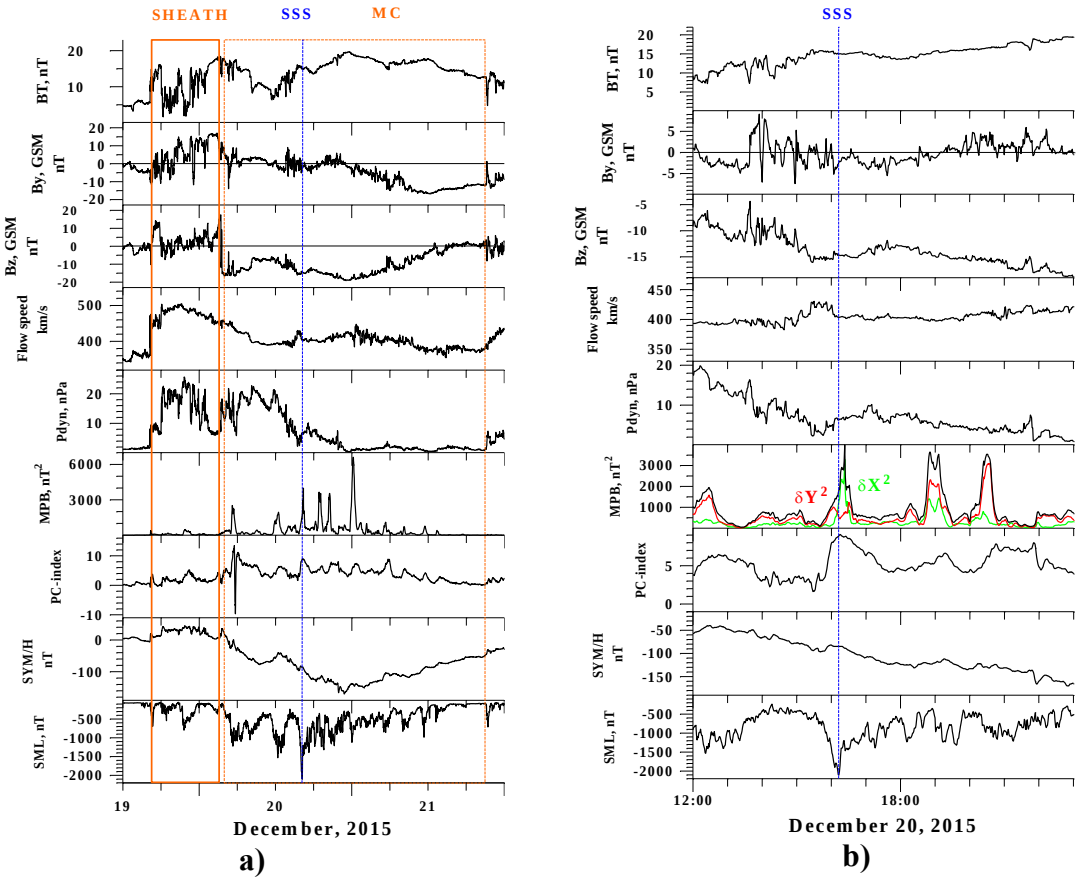

Figure 2. *Variations of the solar wind and IMF parameters (BT, By, Bz, V, Pdyn) and some geomagnetic indexes (MPB, PC, SYM/H, SML) from 12 UT on 19 December to 12 UT on 21 December 2015 (a) and from 12 to 23 UT on 20 December 2015 (b). The boundaries of the solar wind types are marked by red rectangles and inscriptions: SHEATH and MC. The moment of the SSS onset is shown by the vertical blue line.*

4. Magnetic field variations by ground-based magnetometers

Ground-based magnetic disturbances during SSS are shown in Figure 3. At the top panel shown the global maps of magnetic field vectors by SuperMag data for 5 time moments, from onset to maximal study of SSS development (Fig.3a). Magnetic vectors rotated to 90° clockwise and shown the direction of ionospheric currents. SuperMag maps also shown the locations of magnetic stations: IMAGE network was located in the evening sector, the station of Greenland and Canada - in the day sector, Siberia and Alaska stations- in the night and morning sector, respectively. It is seen that very strong disturbances were observed at the auroral zone in the postmidnight and morning sectors on the Alaska stations (Barrow, College and Yellowknife). The westward electrojet developed in a global scale in the longitude - from dawn to the dusk one.

Figure 3b presents the variations of X- component of magnetic field observed at the IMAGE magnetometers, at the left panel shown the map of IMAGE stations. An analysis of the IMAGE data showed that at the stations from Ny-Ålesund to Oulujärvi negative bays were observed in

the X-component of the magnetic field (~ -850 nT). At this time, to the South, from Mekrijärvi to Birzai, positive bays were observed, these stations are marked by yellow stars on the map.

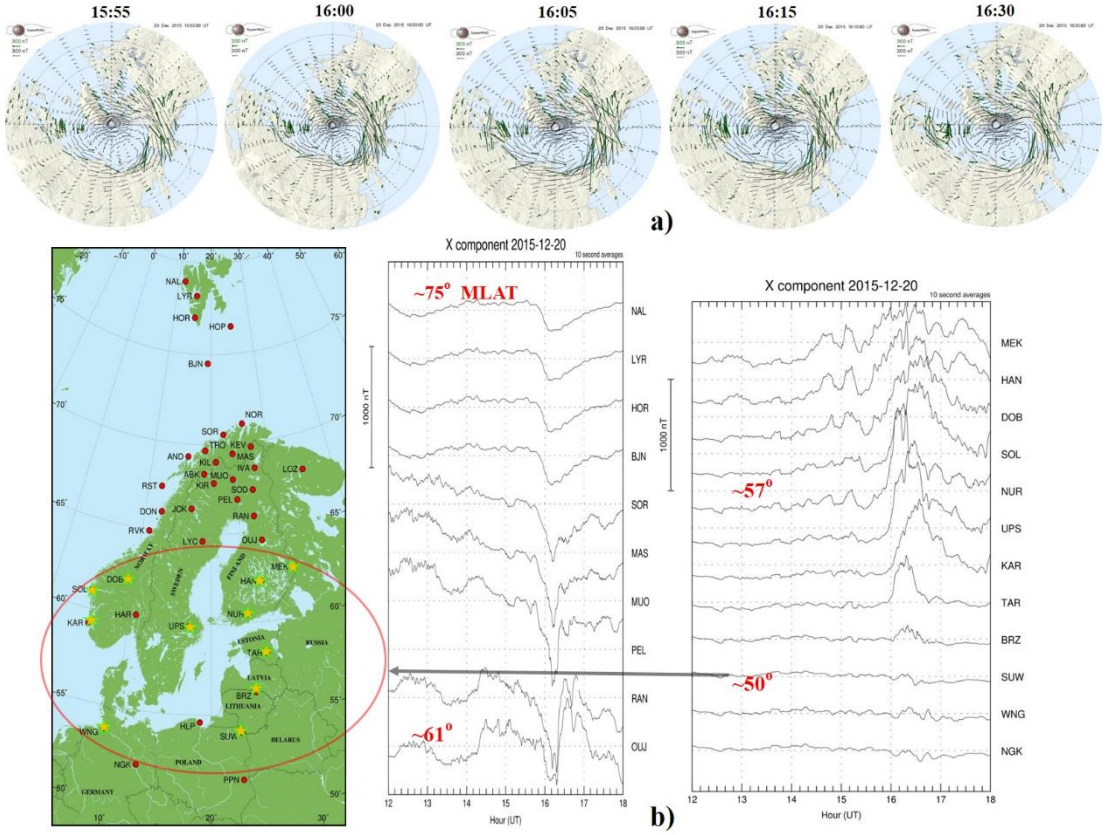

F**igure 3**. *(a) - Global maps of spatial distribution of magnetic field vectors from the SuperMAG network at 15:55, 16:00, 16:05, 16:15 and 16:30 UT (a);the map and magnetograms of some stations on IMAGE network from 12 to 18 UT on 20 December 2015 (b). Yellow stars are marked the stations, were observed the positive magnetic bays.*

Figure 4 shows some magnetograms by the SuperMAG data at different longitudes from 12 to 20 UT on 20 December 2015. It is seen that negative bays were observed from the North of Norway (AND) through Siberia to the North-West of the Canada (C07). The maximal disturbances were registered in the morning sector (BRW). At the right panel, you can see positive bays, which observed at station located at ~56 - 60° magnetic degrees from the North of Scotland (LER) through the South of Scandinavia to the South of the Arkhangelsk region (KLI). The positive bays were also registered at latitudes of ~52°, in Moscow, Kazan and near Yekaterinburg (~100 nT).

5. Ionospheric currents from AMPERE observations

Figure 5 presents some maps of magnetic field vectors, obtained by SuperMAG, spherical harmonic analysis of magnetic registrations and equivalent downward (upward) currents obtained by AMPERE project. Three panels corresponded to growth (a), expansion (b) and maximal (c) phases of SSS. It is seen that during expansion phase the magnitude of the westward electrojet strongly increases, and the electrojet observed at the global scale – from midnight to day sector. The eastward electrojet also intensifies. Then, in the evening sector, rotation of the magnetic vectors around the eastward electrojet begins to be observed. Better the vortex of magnetic vectors observed at middle maps of the Figure 5. During maximal development of SSS, the very strong vortex observed in the evening sector, corresponded the

increased upward currents. At the left panel the turn of vectors is carried out clockwise (counterclockwise), blue ovals indicated their longitudinal dimensions.

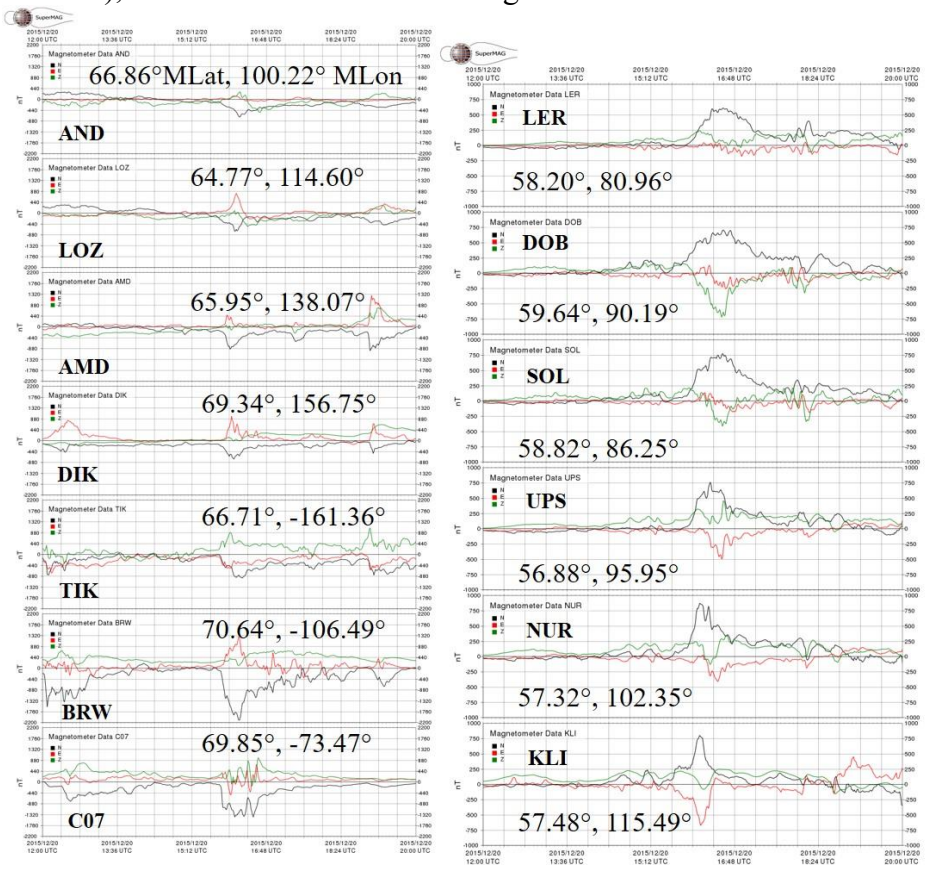

F**igure 4**. *Magnetograms of some stations by SuperMAG, where negative (a) and positive bays (b) were registered.*

6. Summary and discussion

Spatial geomagnetic effects of the supersubstorm on 20 December 2015 were analyzed using data from the global magnetometer networks SuperMAG, IMAGE and AMPERE project data. It is shown, that supersubstorm developed on a global scale: very intense westward electrojet was observed from the late morning to the evening sector, with the maximum in the morning sector (~06 MLT).

Moreover, the intense eastward electrojet was observed in the evening sector (~18 MLT). During the expansion phase of the substorm, a current structure was observed in the evening sector, which corresponded to the appearance of an additional current wedge of the opposite direction. This idea was proposed in earlier works, when authors considered another supersubstorm events [Zong et al, 2021; Despirak et al., 2022]. Note, that the enhancement of partial ring current simultaneously with formation of SCW indicated in the earliest works [Horning et al., 1974].

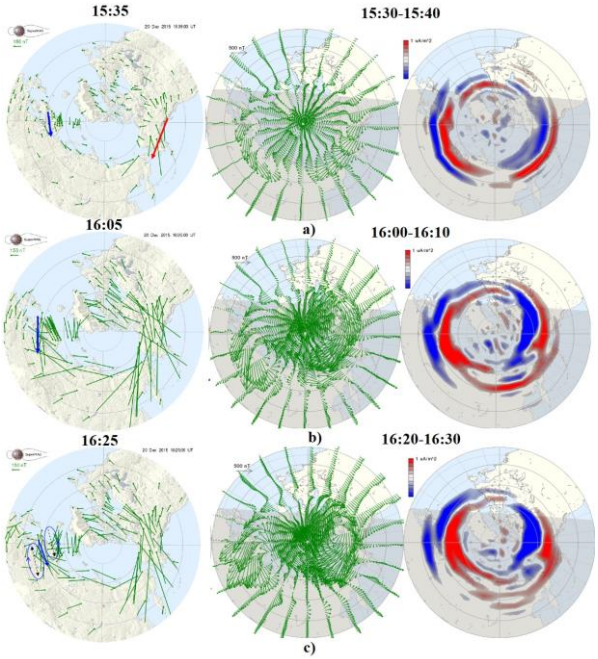

F**igure 5**. *Global maps of spatial distribution of magnetic field vectors from the SuperMAG network (left maps), spherical harmonic analysis of magnetic field vectors (middle maps) and field-aligned current distribution for three moments: at ~ 08:30 UT and ~ 08:55 UT on December 20, 2015 according to AMPERE data. The upward currents mark by red, the downward ones – by blue. Three panels corresponded to growth (a), expansion (b) and maximal (c) phases of SSS.*

Acknowledgments

This study was supported by the RFBR (project number 20-55-18003) and National Science Fund of Bulgaria (NSFB) (project number КП-06-Русия/15).

References

Anderson, B.J., Korth, H., Waters, C.L., Green, D.L. et al. (2014). Development of large-scale Birkeland currents determined from the Active Magnetosphere and Planetary Electrodynamics Response Experiment, Geophys. Res. Lett., Vol 41, No 9, pp. 3017-3015, https://doi.org/10.1002/2014GL059941

Despirak, I.V., Kleimenova, N.G., Lyubchich, A.A., Setsko, P.V., Gromova, L.I., Werner, R. (2022). Global development of the supersubstorm of May 28, 2011, Geomagn. Aeron., Vol 62, No 3, pp. 199-208. https://doi.org/10.1134/S0016793222030069

Horning, B.L., McPherron, R.L., Jackson, D.D. (1974) Application of linear inverse theory to a line current model of substorm current systems, J. Geophys. Res., Vol 79, No 34, pp. 5202-5210.

Kepko, L, McPherron, R.L., Amm, O., Apatenkov, S., Baumjohann, W., Birn, J., Lester, M., Nakamura, R., Pulkkinen, T.I., Sergeev, V.A. (2015) Substorm Current Wedge Revisited, Space Sci Rev., Vol. 190, pp. 1–46, https://doi.org/10.1007/s11214-014-0124-9

McPherron, R.L., Russell, C.T., Aubry, M.P. (1973), Satellite studies of magnetospheric substorms on August 15, 1968: 9. Phenomenological model for substorms, J. Geophys. Res., Vol 78, No 16, pp. 3131-3149, https://doi.org/10.1029/JA078i016p03131

McPherron R.L., Chu X. (2016). The mid-latitude positive bay and the MPB index of substorm activity. Space Science Reviews, 206(1–4), 91–122. https://doi.org/10.1007/s11214-016-0316-6

McPherron R.L., Chu X. (2018). The midlatitude positive bay index and the statistics of substorm occurrence. JGR Space Physics, 123, 2831–2850. https://doi.org/10.1002/2017JA024766

Tsurutani B.T., Hajra R., Echer E., Gjerloev J.W. Extremely intense (SML≤ −2500 nT) substorms: isolated events that are externally triggered? *Ann. Geophys.*, V. 33, P. 519–524, 2015.

Zong, Q.-G., Yue, C., Fu, S.-Y. (2021). Shock induced strong substorms and super substorms: Preconditions and associated oxygen ion dynamics, Space Science Review, V. 217. https://doi.org/10.1007/s11214-021-00806-x.

Polar Geomagnetic Disturbances and Auroral Substorms During the Magnetic Storm on 20 April 2020

Gromova L.I.[1], *Kleimenova N.G.*[2], *Despirak I.V.*[3], *Gromov S.V.*[1], *Lubchich A.A.*[3], *Malysheva L.M.*[2]

[1]Pushkov Institute of Terrestrial Magnetism, Ionosphere, and Radio Wave Propagation, Moscow, Troitsk, Russia; e-mail:ligromova@yandex.ru
[2]Schmidt Institute Physics of the Earth RAS, Moscow, Russia
[3]Polar Geomagnetic Institute, Apatity, Russia

Abstract

The global features of the spatial-temporal distribution of high-latitude geomagnetic disturbances have been studied during the first magnetic storm (20 April 2020) of the new, 25-th cycle of the solar activity. Basing on the ground-based measurements by the global networks SuperMAG, INTERMAGNET and IMAGE magnetometers, it was shown that the geomagnetic disturbances during this storm was significant (*Kp* = 5) despite the low speed of the magnetic cloud (MC) that caused this storm. So, in the storm initial phase, there was developed the high-latitude geomagnetic disturbances which were concentrated at the morning-dayside polar latitudes above ~ 65-70° Mlat. It was found the high-latitude vortices of the geomagnetic field which could indicate the local intensification of the Field-Aligned Currents. Two intense (> 1000 nT) auroral substorms were observed in the storm-main phase, caused by an appearance of large amplitudes of the southward IMF *Bz*. Thus, the magnetic storm geoeffectiveness depends more on the appearance of large values of the southward IMF than on the low values of the solar wind speed.

Keywords: magnetic cloud, magnetic storm, geomagnetic disturbances

1. Introduction

The storm on 20 April 2020 was the first magnetic storm of the new 25 solar cycle. It developed after the long period of the quiet solar wind and, correspondingly, weak geomagnetic activity (*Kp* ≤ 2) that it is shown in Figure 1. The storm was associated with a *slow* magnetic cloud (MC) approached the magnetosphere of the Earth. The detailed overview of the solar event caused this MC and, as a result, the considered magnetic storm, was reported in [Davies et al., 2021; O'Kane et al., 2021].

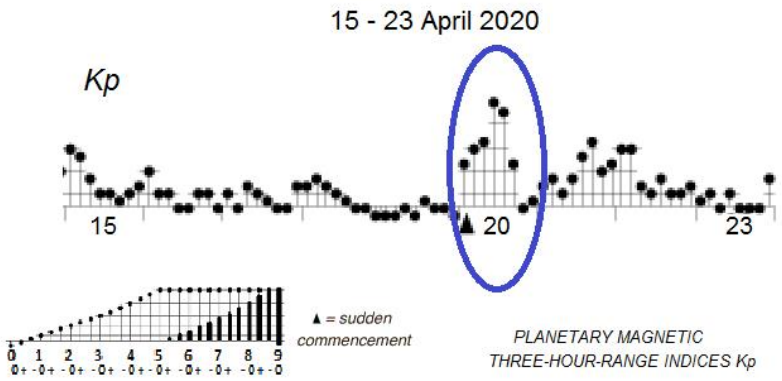

Figure 1. *Planetary geomagnetic index Kp before and during the magnetic storm on 20 April 2020. After https://wdc.kugi.kyoto-u.ac.jp/kp/*

Usually, geoeffectiveness of slow magnetic clouds is low, they do not cause intense storms [Richardson and Cane, 2012]. There are lot of works studying intense magnetic storms caused by *fast* magnetic clouds, e.g., [Tsurutani et al. 1992, Kleimenova et al. 2021 and references therein]. But magnetic storms associated with *slow* magnetic clouds have not been studied enough, e.g., [Nitta et al, 2021], as well as their high-latitude geomagnetic effects.

The aim of our paper is to study high-latitude geomagnetic disturbances during the magnetic storm of 20 April 2020 as a storm associated with the slow solar wind.

2. Space weather on 20 April 2020

The variations of the interplanetary magnetic field (IMF) and solar wind parameters on 20 April 2020 are shown in Figure 2. One can see that the magnetic cloud approached the Earth

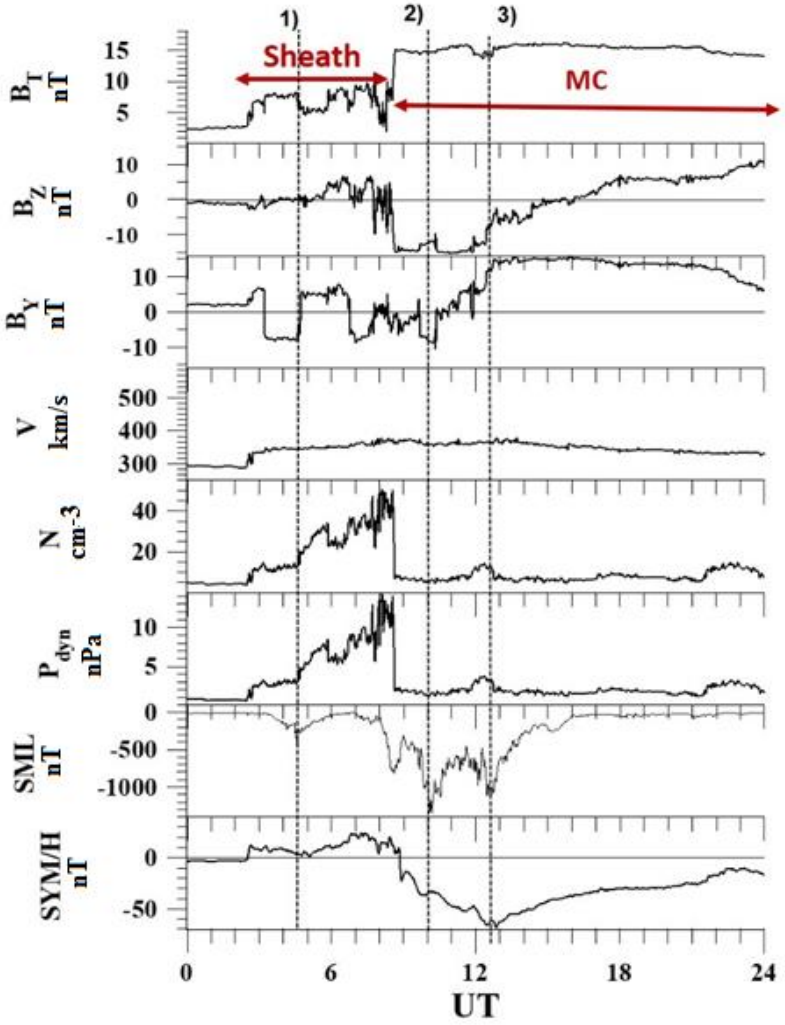

***Figure 2**. The variation of the IMF and solar wind parameters, planetary indices SML-index of the auroral activity and SYM/H–index of the storm The red horizontal arrows show the boundary of the large-scale streams of the solar wind (SHEATH and MC). Data from http://omniweb.gsfc.nasa.gov and http://supermag.jhuapl.edu/mag.*

with the low speed of the solar wind. The magnetic cloud was characterized by a low and practically unchanged speed of the solar wind, but with a significant amplitude of the southward Interplanetary Magnetic Field (*Bz* IMF reached -15 nT), which was not changed for about 4 hours. Apparently, this led to the development of a moderate magnetic storm with a maximum value of *SYM/H* ~ -70 nT. The low solar wind speed (~350-400 km/s) which did not change during the storm makes it possible, on the one hand, to reveal geomagnetic disturbances that

are not related to the solar wind speed, and, on the other hand, to consider the influence of the IMF components on them. Here we used *SYM/H*-index as 1-min analog of the 1-hour *Dst*-index, and *SML*-index of the auroral activity that shares the same methodology of *AL*-index and basing on the SuperMAG data [Gjerloev, 2012].

3. Initial phase of the magnetic storm on 20 April 2020

The storm initial phase started at 02:30 UT when the solar wind density and dynamic pressure increased significantly, from 5 to 50 cm^{-3} and from 1.5 to 15 nPa correspondingly as it can be seen in Figure 2 and Figure 3a. However, the solar wind speed remained low at V ~ 350 km/s, and the *Bz* and *By* components of the IMF varied slightly.

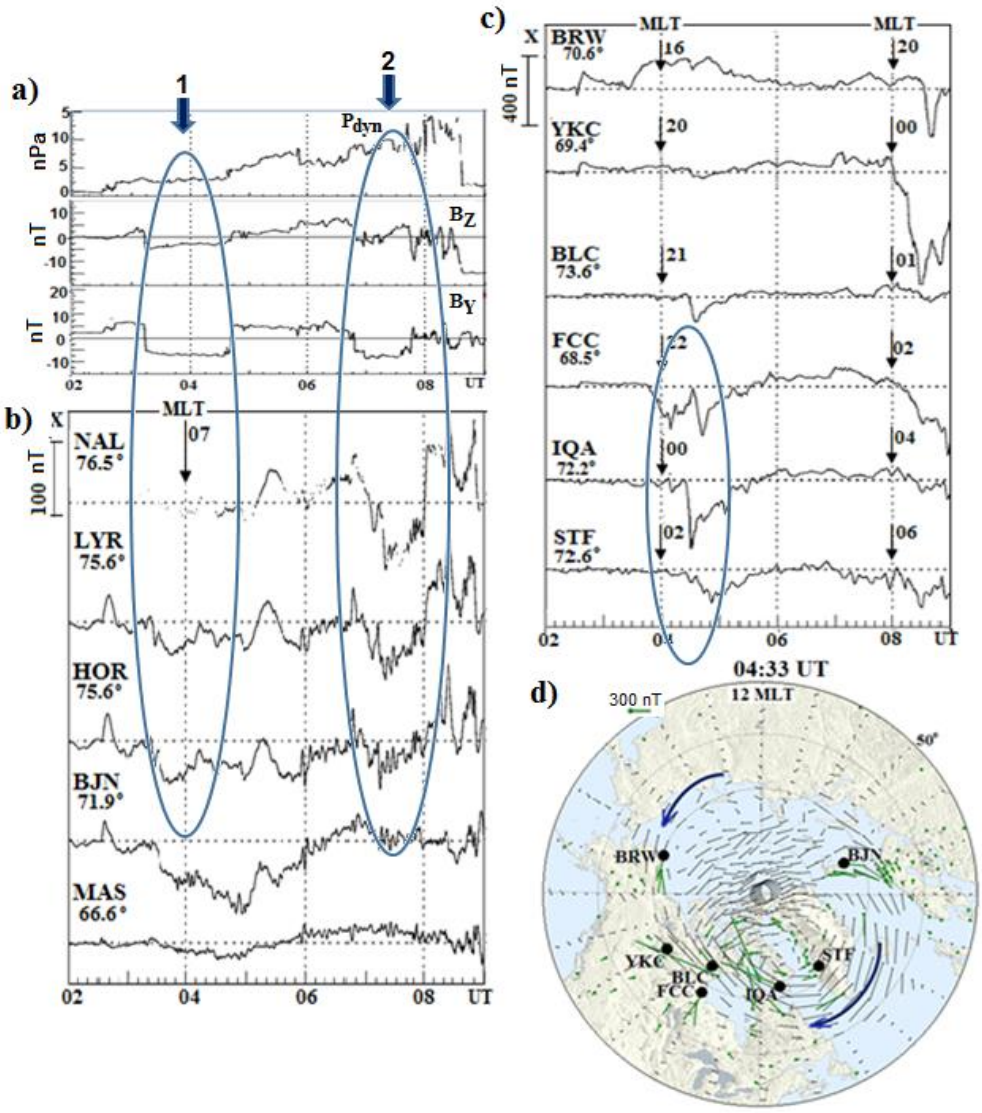

Figure 3. *Initial phase of the storm: a) the solar wind pressure and the IMF Bz and By; variations: (b) IMAGE stations located in the morning-daytime sector; (c) the same from the high latitude American stations located in the nighttime sector; d) the instantaneous (at the maximum of the magnetic bay-1 at 04:33 UT) map of the magnetic vectors from ground-based SuperMAG magnetometers. Vectors of the magnetic field were rotated 90° clockwise to indicate ionospheric equivalent current direction. Blue arrows show maximum of the bays under consideration. Data from http://omniweb.gsfc.nasa.gov, http://space.fmi.fi/image/ and http://supermag.jhuapl.edu/mag.*

In Figure 3b one can see the negative bay-like geomagnetic disturbances in the morning and early-daytime sectors at the high-latitudes IMAGE stations. The IMF *By* was dominant, so, it

controlled the sign of the magnetic bays which agrees with previous results [e.g., Gromova et al., 2016].

Note, the magnetic bay-1, pointed by vertical line (1) in Figure 2, was more intense at HOR and LYR stations, but the magnetic bay-2 was more intense at the higher latitudes, at LYR and NAL stations. In the case of the substortm-2, the solar wind dynamic pressure was almost 2 times higher than during the substorm-1. The shift of the magnetic bay-2 to higher latitudes may be the result of the daytime polar cusp expansion with increasing the solar wind dynamic pressure.

The SuperMAG map of the magnetic vector distribution, built in the substorm maximum, shows two large-scale magnetic field vortices with centers in the post-midnight and afternoon sectors marked by the black arrows. They could be as an indicator of the local increase of the Field-Aligned Currents (FAC) under the low and unchanged solar wind speed.

3. Main phase of the storm

The main phase of the storm was associated with approach the Earth of the magnetic cloud with the large IMF B_T (up to 15 nT) and with southward turn of the IMF *Bz.* The sign of the *SYM/H* variations changed from positive to negative. At the same time the dynamic pressure of the solar wind dropped sharply but the solar wind speed remained low, ~350-380 km/s.

Geoeffectiveness of the magnetic cloud expressed in the development of two intense (more than 1000 nT) magnetospheric substorms observed in the main phase of the storm. They are pointed by the vertical lines (2) and (3) in Figure 2.

The scenario of these substorms is similar to the scenario of supersubstorm developed during a large storm main phase [Despirak et al., 2021]. On the SuperMAG map, presented in Figure 4c, one can see the substorm-1 ionospheric currents expanding from the evening to early morning sector (Figure 3d), and the substorm-2 currents expanding from the local midnight to almost 08 MLT. The centers of the electrojets were observed in the near-midnight sector, (Figure 4b) at latitudes below 65º MLAT, as it is indicated by positive deviations of the *Z*-component of the magnetic field in BRW and in CMO.

We could assume that these substorms were caused by the appearance of large amplitudes of the southward IMF *Bz.*

4. Conclusion

The magnetic storm on 20 April 2020 caused by a *slow* magnetic cloud approached the magnetosphere of the Earth was first moderate magnetic storm of the new 25 solar cycle. Despite of the low solar wind speed, geomagnetic disturbances during this storm were significant (Kp = 5).

- In the initial phase of the storm was developed under SHEATH conditions. There it was found two high-latitude magnetic field vortices with centers in the post-midnight and afternoon sectors. These vortices could be an indicator of the local enhancement of the Field Aligned Currents in the polar latitudes.
- We found that in the initial phase of this magnetic storm, the intensification of the FACs was observed under low values of the solar wind speed.
- In the main phase of the magnetic storm, associated with approach the Earth of the MC with the large IMF B_T there were two intense magnetospheric substorms observed. Apparently, they caused by the appearance of large amplitudes of the southward IMF *Bz.*

Thus, the first magnetic storm in the new solar activity cycle, despite the low speed of the solar wind, led to the development of the significant geomagnetic activity due to large negative values of the IMF *Bz* in the main phase of this storm. We conclude that the geoeffectiveness of this magnetic storm depended more on the appearance of large values of the southward IMF than on the low values of the solar wind speed.

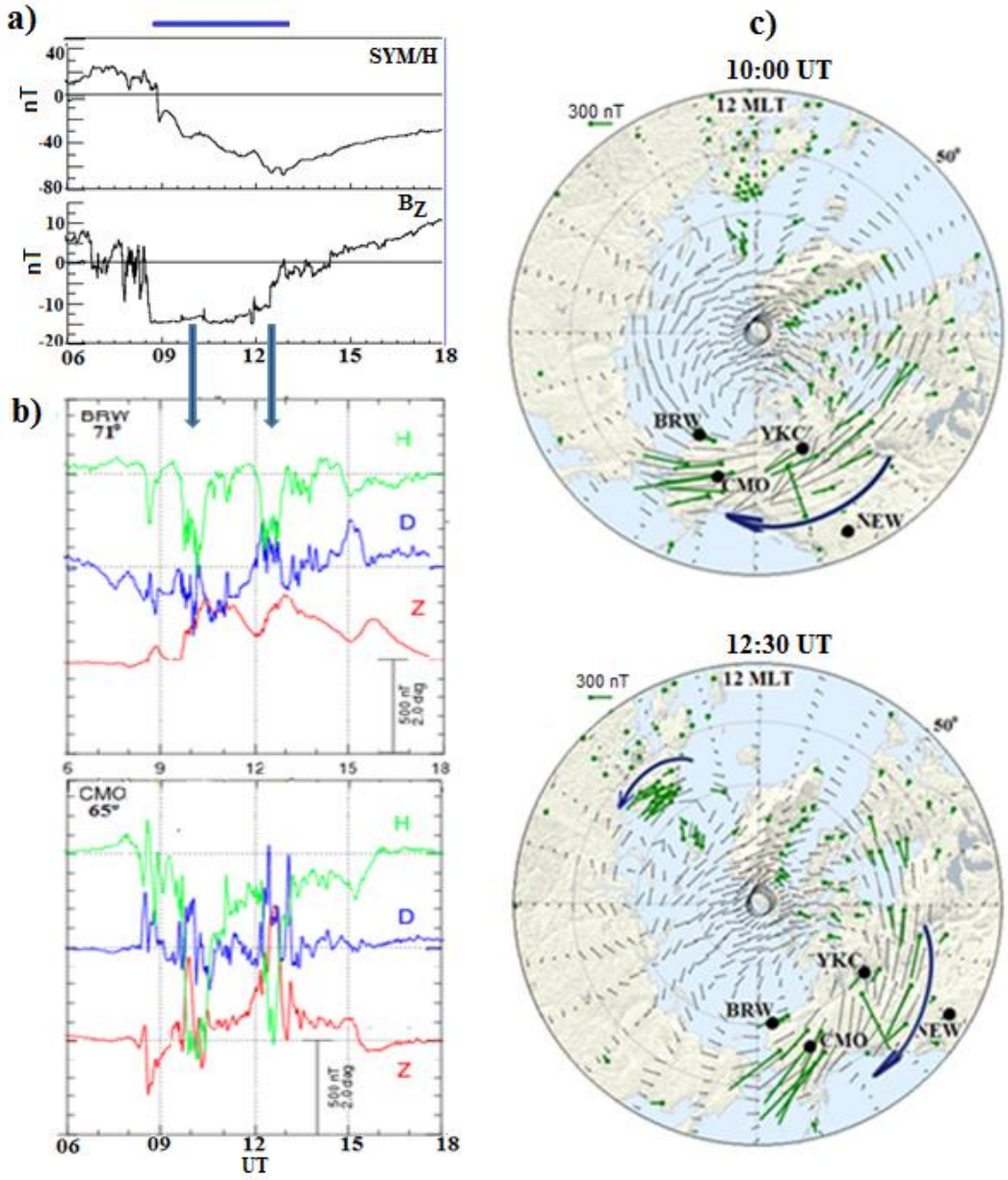

Figure 4. *Interplanetary conditions and variations of the geomagnetic field in the main phase of the storm: (a) SYM/H-index and the IMF B_Z; b) H-, D-, Z-components of the geomagnetic field at BRW and CMO stations (data from https://wdc.kugi.kyoto-u.ac.jp/plot_realtime/qu; c) the instantaneous map of the magnetic field vectors from ground-based SuperMAG magnetometers in the maximum of substorms under consideration, pointed by the blue arrows.*

Acknowledgments

The authors are grateful to the creators of OMNI (http://omniweb.gsfc.nasa.gov), SuperMAG (http://supermag.jhuapl.edu), IMAGE (http://space.fmi.fi/image/), Intermagnet (https://www.intermagnet.org/), World Data Center for Geomagnetism, Kyoto (https://wdc.kugi.kyoto-u.ac.jp/plot_realtime) for allowing to use these databases in our study.

References

Davies, E.E., Möstl, C., Owens, M.J. et al. (2021). In situ multi-spacecraft and remote imaging observations of the first CME detected by Solar Orbiter and BepiColombo, A&A, V 656, id. A2. https://doi.org/10.1051/0004-6361/202040113

Despirak, I.V., Lyubchich, A.A., Kleimenova, N.G. *et al.* (2021). Longitude Geomagnetic Effects of the Supersubstorms during the Magnetic Storm of March 9, 2012. Bull. Russ. Acad. Sci. Phys., (2021). V 85, pp.246–251. https://doi.org/10.3103/S1062873821030096

Gjerloev J.W. (2012). The SuperMAG data processing technique, J. Geophys. Res., V 117, A09213. https://doi.org/10.1029/2012JA017683

Gromova, L.I., Kleimenova, N.G., Gromov, S.V, Dremukhina, L.A., and Zelinskii, N.R., Daytime geomagnetic disturbances at high latitudes during a strong magnetic storm of June 21–23, 2015: The storm initial phase, *Geomagn. Aeron. (Engl. Transl.)*, 2016, V 56, No. 3, pp. 281–292.

Kliemenova, N.G., Gromova, L.I., Gromov, S.V. et al. (2021). High-Latitude geomagnetic disturbances and field-aligned currents in the recovery phase of the large magnetic storm, Geomagn. Aeronom. V 61, No 4, pp. 520-528. https://doi.org/10.31857/S0016794021040076

Nitta, N.V., Mulligan, T., Kilpua, E.K. (2021). Understanding the origins of problem geomagnetic storms associated with “Stealth” coronal mass ejections, Space Sci. Rev, V 217, id. 82. https://doi.org/10.1007/s11214-021-00857-0

O’Kane, J., Green, L. *Davies E.*, et al. (2021). Solar origins of a strong stealth CME detected by Solar Orbiter, A & A, V 656, id. L6. https://doi.org/10.1051/0004-6361/202140622

Richardson, I.G., Cane H. V. (2012). Solar wind drivers of geomagnetic storms during more than four solar cycle. J. Space Weather Space Clim., V. 2, A01. https://doi.org/10.1051/swsc/2012001

Tsurutani, B.T., Gonsalez W.D., Tang F. et al.(1992). Great magnetic storms, Geophys. Res. Lett. V. 9. – pp..73-76. https://doi.org/10.1029/91GL02783

Maps of the Spatial Distribution of the Variations in the X and Y Components of the Magnetic Field at European Midlatitudes During Substorms: A Case Study

Guineva V[1], *Werner R.*[1], *Bojilova R.*[2], *Atanassov A.*[1], *Raykova L.*[1], *Valev D.*[1]

[1]Space Research and Technology Institute (SRTI), Bulgarian Academy of Sciences, Stara Zagora Department, Bulgaria
[2]National Institute of Geophysics, Geodesy and Geography (NIGGG), Bulgarian Academy of Sciences, Sofia, Bulgaria
E-mail: v_guineva@yahoo.com

1. Abstract

The goal of this work is to present the utility of maps of the magnetic field components variations to define the characteristics of the magnetospheric substorms appearance at midlatitudes. To study the spatial distribution of the magnetic field components variations during substorms, an isolated substorm in non-storm conditions, the substorm on 22 March 2013 at ~23:07 UT with central meridian over Europe has been chosen. Magnetic field data from INTERMAGNET, SuperMAG and IMAGE databases have been used. The X and Y variations due to the substorm were computed for 56 stations based on the developed programs. Maps of the spatial distribution and latitudinal and longitudinal profiles of the magnetic variations have been created and some characteristics as the line of sign conversion latitude, the central meridian, the longitudinal and latitudinal extent of the midlatitude positive bays (MPB) and the latitudinal and longitudinal dependence of the variations at three times with maxima during the maximal development of the substorm have been estimated. The central meridian is near PAG (~37°MLAT, ~97°MLON): it is at ~84°MLON during the first part of the substorm and at ~106° MLON in the final stage. The sign conversion latitude is in the range 60°-67°MLAT, the latitudinal extent – from 46° to 53°, and the longitudinal extent – from 60° to 140° during the stage of the maximal development of the substorm. These results are typical for expanded substorms.

Keywords: magnetospheric substorm, midlatitude positive bay (MPB), perturbations maps

2. Introduction

Magnetospheric substorms are an important element of the space weather. During magnetospheric substorms, a considerable release of energy from the magnetospheric tail into the ionosphere and inner magnetosphere occurs [Akasofu, 1968]. They are the main reason for the specific disturbances of the magnetic field on the Earth surface. According to the present-day view, a current system forms, namely, the substorm current wedge (SCW) [McPherron et al., 1973]. At auroral latitudes, negative bays in the X component are observed, driven by the westward electrojet, and at midlatitudes, positive bays in the X magnetic component are seen, associated with the field aligned currents. The magnetic variations at midlatitudes can be used to study the magnetospheric substorms. For example, in a number of papers the onset of the midlatitude positive bays (MPB) has been used as indicator of the beginning of the substorm expansion phase [e.g. Mende at al., 1972, McPherron and Chu, 2017], the sign of the Y component was used by Meng and Acasofu [1969] to set the direction of the field aligned currents, a method to determine the geomagnetic longitude of the auroral substorm onset was worked out [Rostoker et al., 1980, Sergeev and Tsyganenko, 1980]. Different kinds of maps of the spatial or temporal distributions and profiles of the magnetic variations at midlatitudes have been constructed to determine some substorm parameters [e.g. Clauer and McPherron, 1974, Pothie et al., 2015].

In this work the magnetic field variations at midlatitudes during substorms have been examined based on maps of the spatial distribution and latitudinal and longitudinal profiles of the magnetic variations on the Earth surface. An isolated substorm in non-storm conditions, the substorm on 22 March 2013 at ~23:07 UT with central meridian over Europe has been chosen for the study. The constructed maps and profiles have been used to estimate some characteristics of the substorm as the line of sign conversion latitude, the central meridian, the longitudinal and latitudinal extent of the midlatitude positive bays (MPB) and the latitudinal and longitudinal dependence of the variations at chosen times of the substorm development.

3. Data

Magnetic field data from the databases INTERMAGNET, SuperMAG, and IMAGE have been used. Data from 53 European stations at auroral and midlatitudes and from 6 Asian stations have been used for the study of the magnetic disturbances due to the examined substorm. The following stations have been included in the study: BDV, BEL, BOX, BRZ, CLF, DUR, EBR, ESK, FUR, GUI, HAD, HLP, HRB, IZN, KIV, KRT, LER, LVV, MNK, MOS, NGK, NUR, OUJ, PAG, PEG, SFS, SPT, SUA, SUW, THY, UPS, VAL, WNG, ABK, BJN, DOB, HAN, HOP, IVA, JCK, KAR, KEV, LYC, LOZ, MAB, MEK, MUO, NOR, PEL, RVK, SOL, TRO, SOR, ARS, NVS, IRT, CNH, YAK, MGD.

4. Processing method

For the data processing, we applied the developed by us program for computing the perturbations of the magnetic field components on the earth surface, described in more detail in Werner et al. (2021a) and Werner et al. (2021b). The program tool is based on the McPherron and Chu algorithm (McPerron and Chu, 2017) and some new developments. In general, the main field and the mean Solar quiet magnetic variations are removed. The program was designed to process the magnetic field data from the Bulgarian station Panagjurishte (PAG) since 2007. Here it was applied to process the magnetic field components registered at a number of stations in order to examine the behavior of the magnetic field in a large area during a selected substorm event. Data for 25 consecutive days centered on the substorm day have been used. The variations of the X, Y components and the horizontal power have been computed.

5. Results

5.1.X component variations

In Figure 1 the variations of the X component of the magnetic field at different stations from 20 to 24 UT on 22.03.2013 are given. In panels a) and b) the result for chosen stations from the PPN-NAL IMAGE chain and its prolongation at midlatitudes is presented, and in panel c) – the X component variations at stations at different longitudes are shown. The station names are written at the left side of the graphs, and the magnetic coordinates – at the right side. Three typical times of the substorm development, at which maxima at some of the midlatitude stations were observed, namely 23:16 UT, 23:27 UT and 23:40 UT, have been selected to be used for the maps of the distribution and the profiles of the X and Y magnetic components construction. These times are shown by blue vertical lines in the graphs of Figure 1.

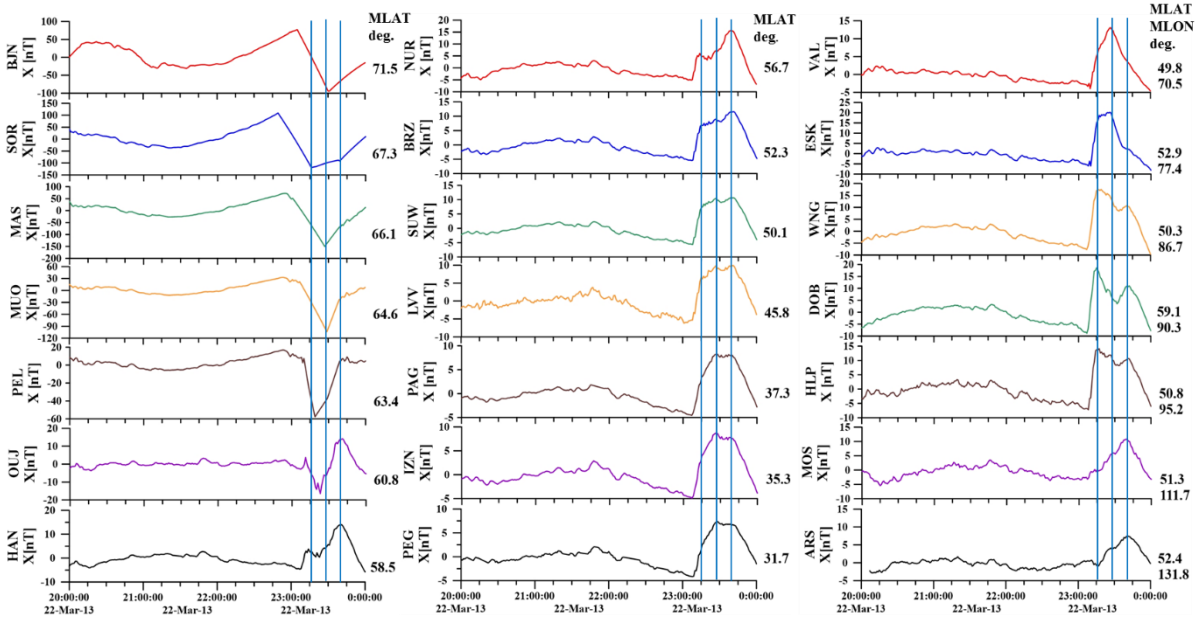

a) b) c)

Figure 1. *a), b): X magnetic variations during the substorm at ~23:07 UT on 22.03.2013 at chosen stations from the IMAGE PPN-NAL chain and its prolongation at midlatitudes (MLON interval 96°-108°); c) X magnetic variations at different longitudes. The blue lines indicate the chosen typical times of the substorm development.*

5.2.Maps of the X and Y components variations

Maps of the X and Y magnetic components spatial distribution at the selected times have been constructed. In Figure 2 the abbreviations of the names and the locations of the stations from which data for the maps creation have been used, are shown. The rectangular frame indicates the area for which the maps were constracted: 38°÷68° geogr. lat. and -5°÷35° geogr. lon.

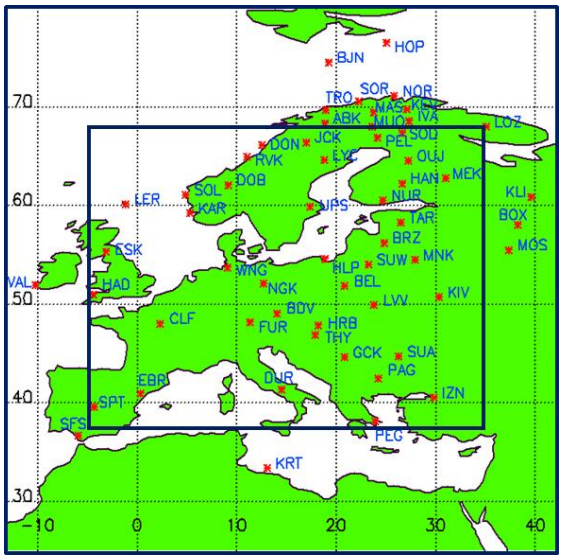

Figure 2. *Stations, used to compute the distribution of the magnetic variations on the Earth surface. The rectangular frame in the figure indicates the region for which maps of the spatial distribution of X and Y are constructed.*

The spatial distributions of the X and Y variations at the three chosen moments during the substorm development are presented in Figure 3, in the upper and lower panels, respectively. In the maps of the X magnetic variations (upper panels in Figure 3) the sign conversion boundary is clearly expressed. It is seen in the range 65°-68° geographic latitude or at about 60°-65° MLAT.

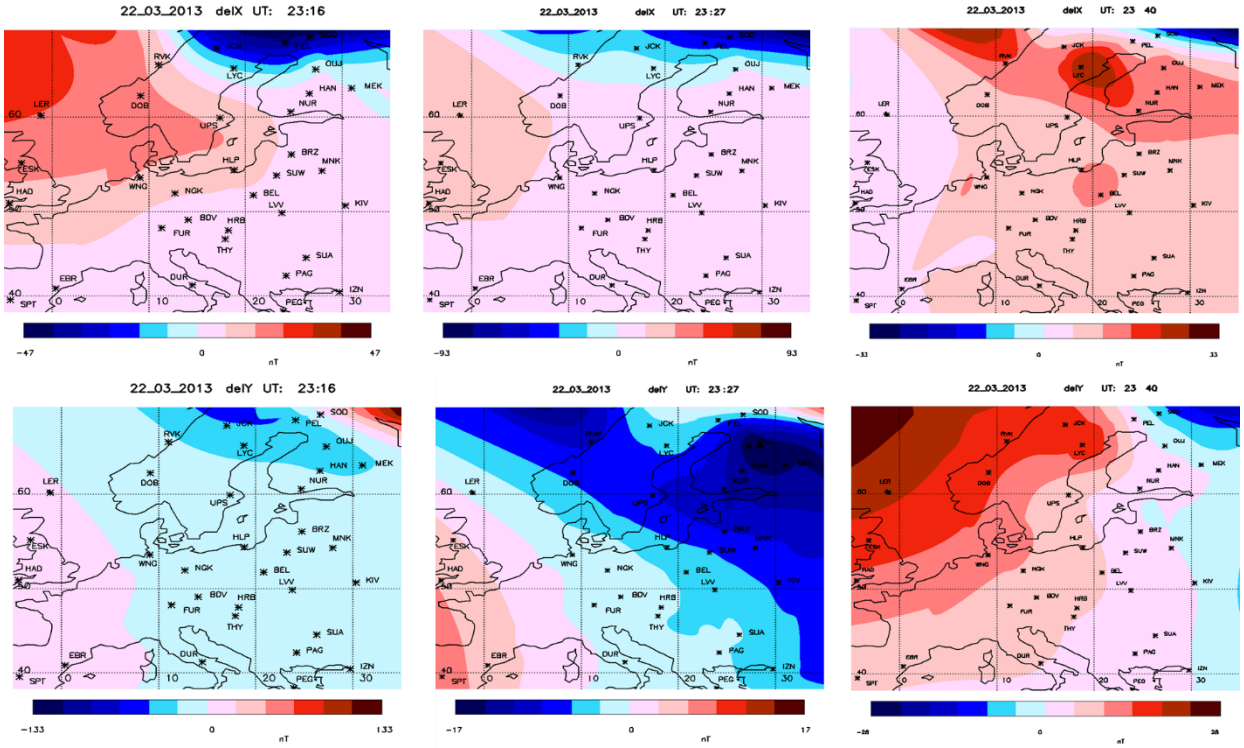

Figure 3. *Maps of the X (up) and Y (down) magnetic variations at the three chosen moments of maxima in X during the substorm development.*

In the maps of the Y magnetic variations (lower panels in Figure 3) the central meridian of the substorm arises, close to the sign conversion in Y.

5.3.Profiles of the X and Y variations

To examine the behavior of the midlatitude positive bays in more detail and over a larger area latitudinal and longitudinal profiles of the X and Y variations have been constructed. They are the dependences of the values of X or Y obtained from the examined stations at the three chosen times from the geomagnetic latitude/longitude. In view of the difference of the profiles at different longitudes/latitudes the data were distributed in groups pertained to the following intervals by geomagnetic longitude: 60°-80° MLON, 80°-95° MLON, 95°-100° MLON, 100°-105° MLON, and 105°-115° MLON to construct the latitudinal profiles and to the following intervals by geomagnetic latitude: 14°-30° MLAT, 30°-40° MLAT, 40°-50° MLAT, 50°-55° MLAT, 55°-60° MLAT to construct the longitudinal profiles. Data from all examined European and Asian stations are used. The obtained profiles are presented in Figure 4, namely: the upper panels display the latitudinal profiles of the X variations for the chosen times, the middle panels show the longitudinal profiles of the X variations, and the bottom panels – the longitudinal profiles of the Y variations. The data from every interval are drawn by markers with different form and colour. The extent of the positive bays is determined by two levels: where the X

variations become 0 nT (0 nT boundary), and where they reach 5 nT (5 nT boundary), presented in the two upper panels of Figure 4 by black and blue vertical lines, respectively. The interception of the 0 line in the X latitudinal profiles where the negative X bays turn into positive ones, gives the sign conversion latitude (upper panel in Figure 4. The interception of the 0 line of the Y variations longitudinal profile points the central meridian of the substorm. It is indicated by red vertical line in the bottom panels of Figure 4.

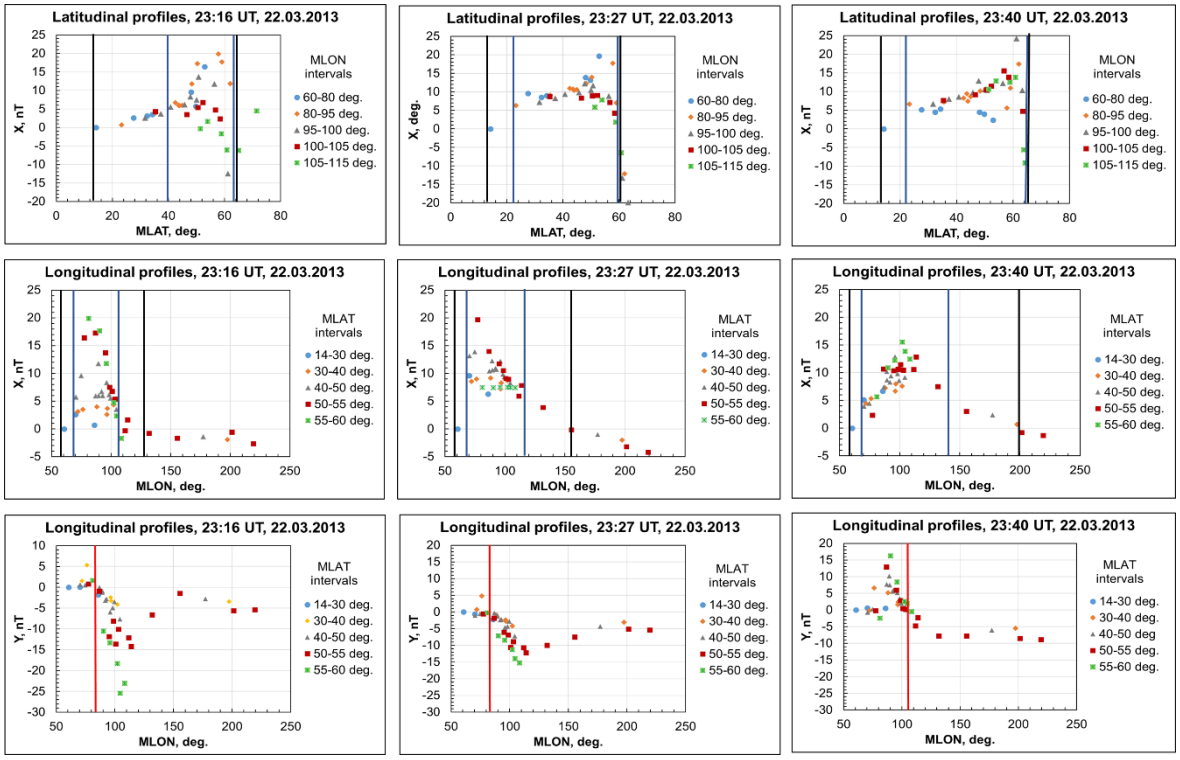

Figure 4. *Latitudinal and longitudinal profiles for given intervals, listed in the panels. The vertical blue lines indicate the latitudinal and longitudinal extent of MPB at the limit of 5 nT, and the black ones – the limit of 0 nT. The vertical red lines point out the location of the central meridian of the substorm.*

The results of the profiles examination are summarized in Table 1. In the rows from up to down the following quantities are given: the boundaries of the MPB presence by geomagnetic latitude, the latitude of the maximum value of the MPB and the interval of latitudes for the maxima in the different longitudinal intervals, the latitudinal extent of the MPB, the MPB boundaries by geomagnetic longitude, the longitude of the MPB maximal value, the longitudinal extent of MPB, and the geomagnetic longitude, where the Y variations cross the 0 line and from positive become negative.

From the upper panels of Figure 4 it is seen, that the latitudinal dependence of the X variations is as follows: after the sign conversion latitude X increases to the lower latitudes, reaches a maximum close to it, and decreases gradually. This confirms our previous results about the behavior of the MPB amplitude from the sign conversion latitude to lower latitudes (Guineva et al., 2021a, b). It is seen also, that the maximal value of X variations is located at different latitude for the different longitudinal intervals.

Table 1. *Results for the MPB latitudinal and longitudinal limits to 0 nT (black colour) and to 5 nT (blue colour), for the location of the maximal value and the central meridian of the substorm*

UT:	23:16	23:27	23:40
MLAT limits	~14°-67° ~40°-65°	~14°-60° ~23°-60°	~14°-63° ~23°-63°
Max at	58°(51°-59°)	53°(53°-58°)	61°(56°-62°)
Lat. extent	~53°(~25°)	46°(~37°)	~49°(~40°)
MLON limits	~60°-120° ~70°-104°	~60°-156° ~70°-120°	~60°-200° ~70°-140°
Max at	~82°	~82°	~102°
Long. extent	~60° (~34°)	~96°(~50°)	~140°(~70°)
Y_0	~84°	~84°	~106°

The latitudinal and longitudinal extent increase during the chosen interval of substorm development, which is during the substorm expansion phase.

In longitudinal direction, maximal variations are observed near the substorm meridian.

Development of the substorm to the West resulting from the westward electrojet progress is observed.

6. Conclusions

The development of the substorm at ~23:07 UT on 22.03.2013 is presented in detail. Maps of the X and Y magnetic components in the range 38°÷68° geographic latitude, -5°÷ 35° geographic longitude, as well as longitudinal and latitudinal profiles for 3 moments of the substorm development: 23:16 UT, 23:27 UT (max. development) and 23:40 UT have been constructed.

By the use of the maps and the profiles, the following the following parameters were estimated: the central meridian of the substorm, the sign conversion latitude, the longitudinal and latitudinal extent. The central meridian is near PAG (~37°MLAT, ~97°MLON): it is at ~84°MLON during the first two chosen times and at ~106° MLON at the third time. The sign conversion latitude is in the range 60°-67°MLAT, the latitudinal extent – from 46° to 53°, and the longitudinal extent – from 60° to 140° during the stage of the maximal development of the substorm.

Similar results were obtained in previous investigations of expanded substorms.

In latitudinal direction, after the sign conversion latitude X increases fast to the lower latitudes, reaches a maximum, and after decreases gradually. This confirms our previous results about the behavior of the MPB amplitude from the sign conversion latitude to lower latitudes.

In longitudinal direction, maximal variations are observed near the substorm meridian.

The latitudinal and longitudinal extent increase during the chosen time interval of the expansion phase of the substorm.

Acknowledgements. The authors are grateful to the creators of the databases OMNI (http://omniweb.gsfc.nasa.gov), IMAGE (http://space.fmi.fi/image/), INTERMAGNET (http://intermagnet.org/), SuperMAG (http://supermag.jhuapl.edu/), and the solar wind large-

scale phenomena catalog (http://www.iki.rssi.ru/omni/) for the opportunity to use them in this work.

This study was supported by the National Science Fund of Bulgaria (NSFB) (project number КП-06-Русия/15) and by the RFBR (project number 20-55-18003Болг_а).

References

Akasofu, S.-I. (1968). Polar and magnetospheric substorms, D,Reidel, Norwell, Mass., DOI: 10.1007/978-94-010-3461-6

Clauer, C.R., McPherron, R.L. (1974). Mapping the local time – universal time development of magnetospheric substorms using midlatitude magnetic observations, J. Geophys. Res., Vol. 79, No 19, pp. 2811-2820, DOI: 10.1029/JA079i019p02811.

Guineva V., Werner, R., Despirak, I., Bojilova, R., Raykova, L. (2021a). Mid-latitude positive bays during substorms by quiet and disturbed conditions, C. R. Acad. Bulg. Sci., 74(8), pp.1185-1193, DOI: 10.7546/CRABS.2021.08.10

Guineva V., Despirak, I., Werner, R., Bojilova, R., Raykova, L. (2021b). Mid-latitude effects of "expanded" geomagnetic substorms: a case study, EPJ Web of Conferences, Vol. 254, 01004, DOI: https://doi.org/0.1051/epjconf/202125401004

McPherron, R.L., Russel, C.T., Aubry, M. (1973). Satellite studies of magnetospheric substorms on August 15, 1968, 9: phenomenological model for substrms, J. Geophys. Res., Vol. 78, No16, pp.3131-3149, DOI: 10.1029/JA078i016p03131.

McPherron, R.L., Chu, X. (2017). The midlatitude positive bay and the MPB index of substorm activity, Space Sci. Rev., Vol 206, pp. 91-122, DOI: 10.1007/s11214-016-0316-6.

Mende, S. B., Sharp, R.D., Shelley, E.G., Haerendel, G., Hones, E.W. (1972). Coordinated observations of the magnetosphere: The development of a substorm, J. Geophys. Res., Vol. 77, No 25, pp.4682-4699, DOI: 10.1029/JA077i025p04682

Pothier, N. M., Weimer, D.R., Moore, W.B. (2015). Quantitative maps of geomagnetic perturbation vectors during substorm onset and recovery, J. Geophys. Res. Space Physics, Vol. 120, pp. 1197–1214, doi:10.1002/2014JA020602.

Rostoker, G., Akasofu, S.-I., Foster, J., Greenwald, R.A., Camide, Y., Kawasaki, K., Lui, A.T.Y., McPherron, R.L., Russell, C.T. (1980). Magnetospheric substorms – definition and signatures, J. Geophys. Res., Vol. 85, No A4, pp. 1663-1668, DOI: 10.1029/JA085iA04p01663

Sergeev, V. A., Tsyganenko, N. A. (1980). Magnitosfera Zemli. Nauka, p.174, (in Russian). .

Werner, R., Guineva, V., Atanassov, A., Bojilova, R., Raykova, L., Valev, D., Lubchich, A., Despirak, I. (2021a). Calculation of the horizontal power perturbations of the Earth surface magnetic field, Proc. Of the Thirteenth Workshop "Solar Influences on the Magnetosphere, Ionosphere and Atmosphere", pp. 159-164, DOI: 10.31401/ws.2021.proc.

Werner, R., Guineva, V., Lubchich, A., Despirak, I., Bojilova, R., Valev, D., Atanassov, A., Raykova, L. (2021b). Determination of power perturbations of the horizontal magnetic field on the Earth surface, Proc. Of the Seventeenth International Scientific Conference Space, Ecology, Safety, pp. 34-38.

Critical Frequency of Ionospheric F1 and F2 Layers and Comparison with Solar Flares Observed in the 24th Solar Cycle

Kilcik A., Tirnakci M.

Department of Space Science and Technologies, Akdeniz University Faculty of Science, 07058, Antalya, Turkey

Abstract

In this study, the number of X-ray solar flares (SFs) that observed during the solar cycle 24 (2008-2020) were compared with the ionospheric F_1 and F_2 layers critical frequencies (f_0F_1, f_0F_2). The temporal variations, cross-correlation and hysteresis analyses were applied. The monthly median ionospheric critical frequency values are taken from the UK Solar System Data Center-Sodankyla (67°N,26°E), while the X-ray Solar flare data are taken from the Laboratory for Experimental Astrophysics (LEA). We found following results; in the temporal variation analysis, especially the critical frequency of the F_1 layer and the total SF, C and X class SF seems to be quite compatible. The critical frequency of the F_2 layer and the number of total X-Ray solar flares show also good agreement with the number of SFs. Critical frequency of ionospheric F_1 and F_2 layers show meaningful positive correlation with total SF numbers (r=0.38, r=0.59, respectively). It has been observed that the separation between the hysteresis analysis and the path shows different cycles, the critical frequency of the F_1 layer has a wider cycle than the critical frequency of the F_2 layer.

Introduction

The sun is the main energy source of the solar system and emits radiation of all wavelengths intervals of electromagnetic spectrum from gamma to radio. Especially ultraviolet (UV) irradiance in the range of 115-420 nm, in the lower thermosphere, mesosphere and stratosphere have a significant effect on temperature distribution, photochemistry and all momentum balance (Ozguc et al., 2008). Ionosphere; since it occurs in the lower thermosphere, mesosphere and exosphere layers, and the energy coming from the Sun directly affects the ionospheric layers. Particularly, extreme UV (EUV) causes photoionization, and thus changes the electron density of the ionospheric layers (Ikubanni et al., 2013). The ionosphere divided into three layers as D, E and F according to the ionized components in these layers. Also, radiation coming from the sun split the F layer into two sublayers as F_1 and F_2. In the F1 layer NO^+ and O_2^+ are the principal ionized component and the main ionization source is EUV. Height of this layer varies with solar zenith angle, geomagnetic activity and seasonal variations. It is more evident primarily in the summer and is not usually observed at night and winter. The dominant charge transporter in the F2 layer is O^+. The main source of ionization in this layer is also photoionization process due to solar EUV radiation. This layer has highly variable nature and the most important property of this layer is existence for 24 hours under all solar-terrestrial conditions, which means it is a very important layer for radio communications. The F layers have a certain maximum frequency at which they can reflect back the radio waves sent from the Earth. This maximum frequency is called the ionospheric critical frequency.

In addition to EUV, the X-ray flux coming from the Sun with the solar flare causes an additional photoionization of all neutral components in the lower ionosphere, including excess elements in the atmosphere, e.g., oxygen, nitrogen (Whitten and Poppoff, 1965). It is known that amount of solar EUV and X-ray fluxes are dependent on solar activity (Ozguc et al., 1998).

Solar flares are sudden increases in brightness observed on the solar surface and are caused by the release of magnetic energy around sunspots. During SF, energy is emitted from the Sun at all wavelengths, but most of them fall outside the visible region as these are quite

high energies. They classified in two classification schemas depend on their observation as, Hα and X-ray classifications. Hα classification is based on the size of the flare region and the intensity of the brightness. Depending on the peak flux in X-ray wavelength interval (1-8 Å) they also classified in five different classes as A, B, C, M and X.
Sunspot number, which is the most obvious indicator of solar activity, was compared with X-ray SF by Hathaway (2015). The M and X class SF numbers seen in the 1.0–8.0 Å band tend to follow the sunspot number and they found that there is a trend for more SF to emergence in the descending phase of the sunspot cycle. Kilcik et al. (2011a) suggested that the maximum CME speed index (MCMESI) can be considered as an indicator of solar activity and geomagnetic activity. Again, Kilcik et al. (2020) found that the MCMESI showed a significant positive correlation with X-ray flare numbers and both data sets also had similar periodic behaviors.

In this study, solar X-ray flare numbers compared with foF1 and foF2 during the solar cycle 24. We describe data and methods used are given in Section 2, analysis and results are given in Section 3, and the discussion and conclusions are presented in Section 4.

Data and Methods

The ionospheric monthly median critical frequency values (f_0F_1 and f_0F_2) are taken from the UK Solar System Data Centre (https://www.ukssdc.ac.uk/wdcc1/iono_menu.html). We used Sodankylä (67°N, 26°E) station data due to the existence of complete f_0F_1 and f_0F_2 data during the solar cycle 24. The monthly median values exist for each hour in the data source and we chose the data for 14:00 local time (LT) for each month. Especially the F_1 layer is highly dependent on the seasonal variations and solar zenith angle there were lots of gaps in f_0F_1 data during the winter months for the investigated time period, while f_0F_2 data exists in all cases. Therefore, we used f_0F_1 data that have monthly median values during a year and used in correlation analysis. The f_0F_2 data are used directly in the study for the investigated time period.
Solar X-ray flare data are taken for each day from Laboratory for Experimental Astrophysics (LEA) (http://www.ioffe.ru/LEA/Solar/) for classes C, M, and X. Then, the number of daily X-ray flares and their monthly mean values were produced for above classes.
As a first step, to remove the small fluctuations and reveal the general trend the 11-step running average smoothing method were applied to all data sets. Thus, the temporal variation plots were produced (see Figure 1). To obtain the relationship between the number of X-Ray solar flares (total and separate classes) and ionospheric critical frequencies (f_0F_1 and f_0F_2) the cross-correlation analysis methods were applied directly to the monthly values. To measure the error levels of obtained correlation coefficients the Fisher test statistics were performed. This test gives us the upper and lower limits of obtained correlation coefficient with 95% confidence.
Finally, we plotted hysteresis behaviors of the number of X-Ray solar flares and the ionospheric critical frequencies. For this analysis the yearly average values were used. If there is a temporal offset between compared two parameters, then the scatterplot will exhibit a loop like structure and this kind scatterplot called hysteresis plot in the literature (Bachmann et al., 2004). The width of loops describes the amount of time delay and the direction of rotation show the which parameter following the other (Ozguc et al., 2016).

Analysis and Results

As a result of our analysis, temporal variation plots are produced as shown in Figure 1. According to this, f_0F_2 data show multiple peak structure like solar activity, while the f_0F_1 data do not.
There is a small peak in all classes flare number data around 2017 and f_0F_1 temporal profile show similar peak with about five-month delay.

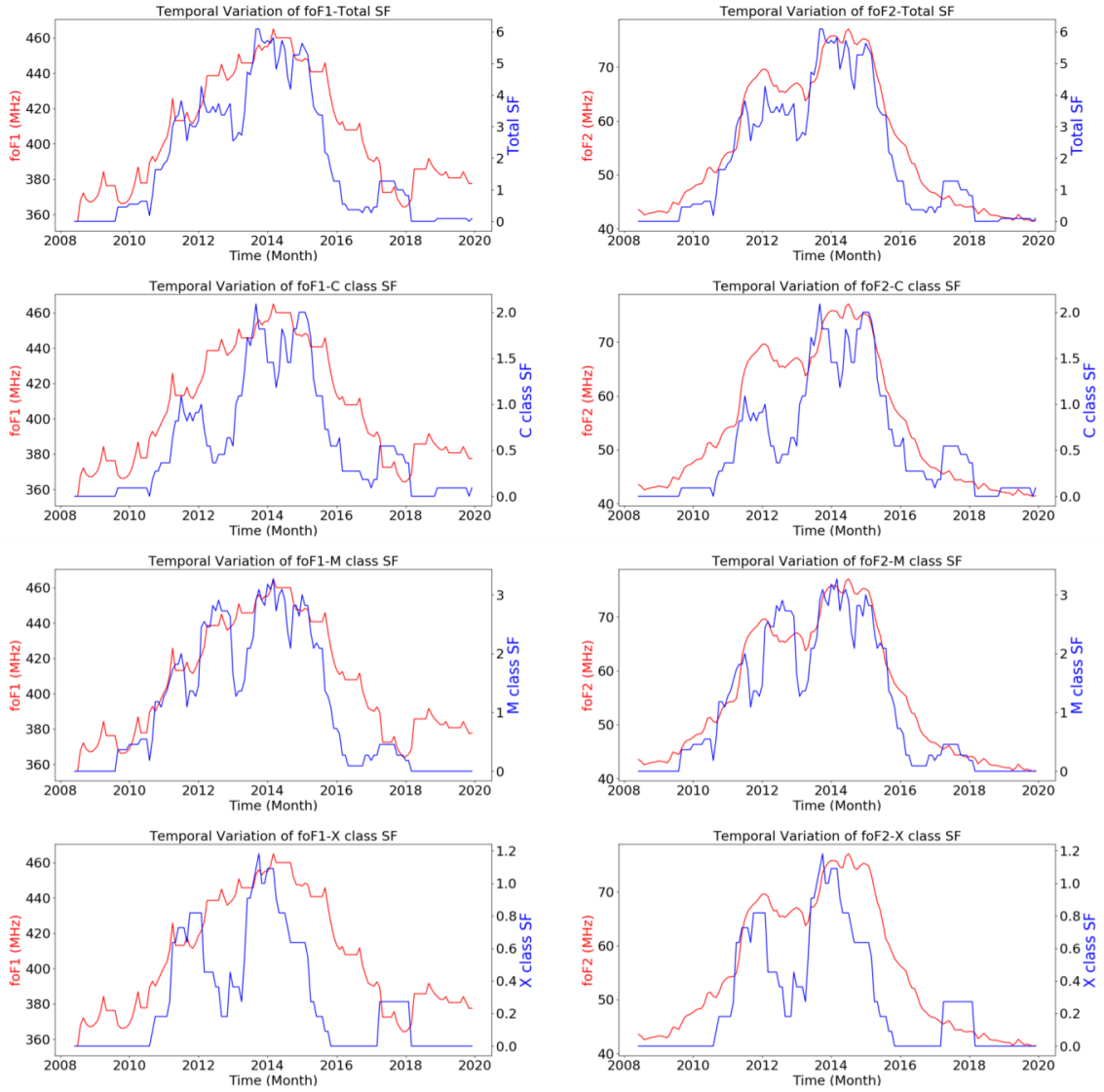

Figure 1. Temporal variation of all parameters used in this study.

Figure 2. shows the cross correlations of f_0F_1 - f_0F_2 and solar X-ray flares number. The results of these plots are also presented in Table 1.

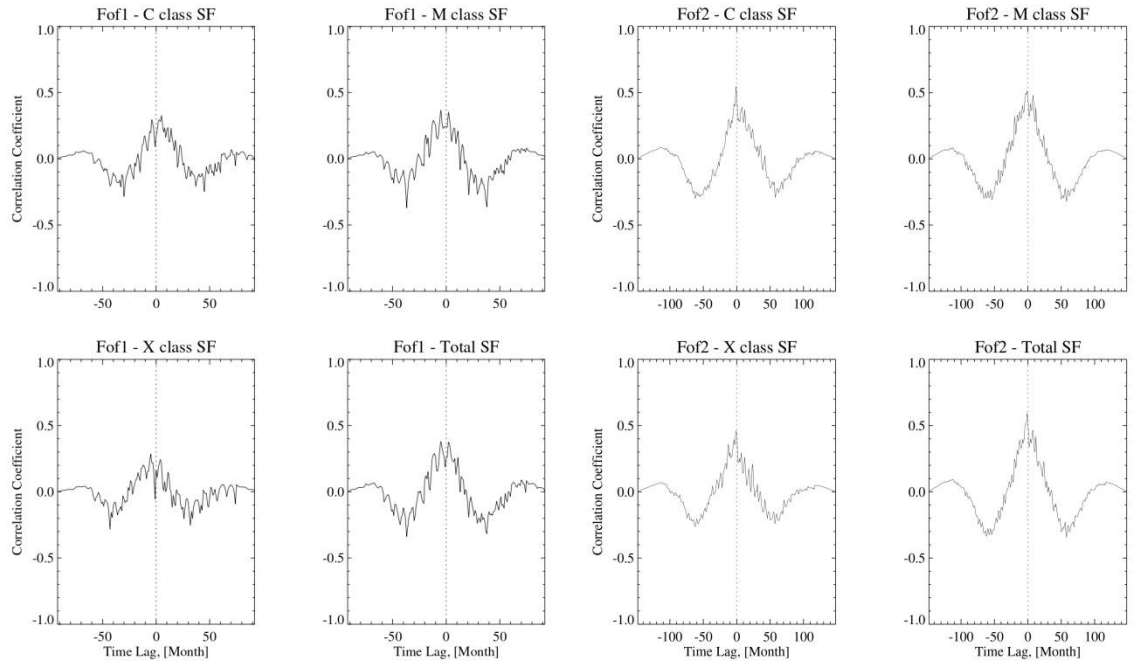

Figure 2. Cross-correlation analysis results between f_0F_1/f_0F_2 and the number of all solar X-ray flares.

Table 1. Cross-correlation coefficients and their corresponding time delays

	f_0F_1- Total SF	f_0F_1-C Class SF	f_0F_1-M Class SF	f_0F_1-X Class SF	f_0F_2- Total SF	f_0F_2-C Class SF	f_0F_2-M Class SF	f_0F_2-X Class SF
Cross Correlation Coefficient	0. 38±0.19	0.33±0.19	0.37±0.19	0.29±0.2	0.59±0.12	0.54±0.12	0.51±0.13	0.46±0.14
Time Delay (Month)	-5	5	-5	-5	-1	-1	-1	-1

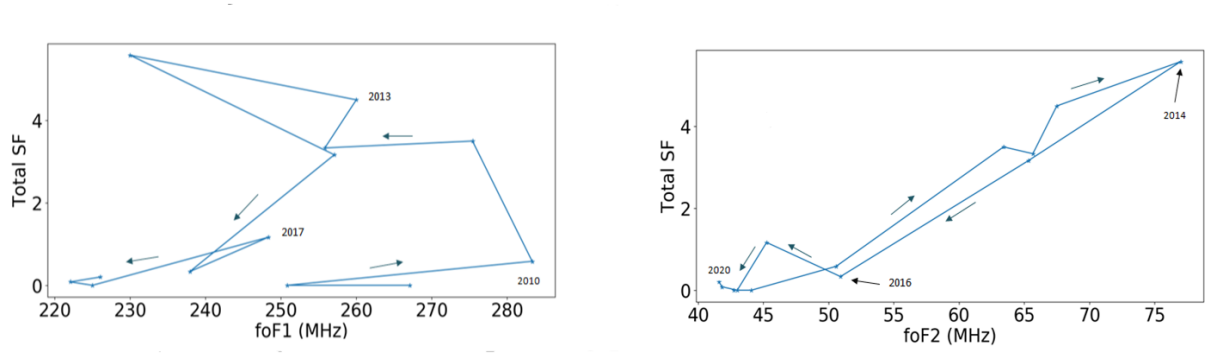

Figure3. Scatter plots showing the hysteresis phenomenon between f_0F_1/ f_0F_2 and the number of total X-Ray flares.

Figure 3 shows the hysteresis analysis results between the number of total X-ray flares and critical frequencies. From this figure we achieved following results; i) In general, the hysteresis cycle exhibit almost regular clockwise circulation for f_0F_2. This result indicates that f_0F_2 behind the X-Ray solar flares. The ascending phase shows higher track than the descending phase and

this confirm above result. The only hysteresis behavior appears around the end of declining phase, ii) for the f_0F_1 the situation is quite different; the hysteresis cycles exhibit counterclockwise circulation and very wide pattern. This means there is time lag between two parameters and the hysteresis patterns appear around minima.

Discussion and Conclusion

In this study, monthly median f_0F_1, f_0F_2 and the number of solar X-ray flares (C, M, and X classes) were investigated during the solar cycle 24. We obtained the following results:

1. f_0F_2 and all X-Ray SF classes show similar temporal behaviors with their double/multiple peak structures, while the f_0F_1 has a single peak structure.
2. In general, the number of total SF show higher correlation compared to separate classes and the f_0F_2 data has also stronger correlation than f_0F_1.
3. f_0F_1 shows more hysteresis behavior compared to f_0F_2
4. The hysteresis behaviors show opposite circulations; f_0F_2 has clockwise circulation, while f_0F_1 has counterclockwise.
5. In both cases the hysteresis behaviors appear mainly around the cycle's minima.

Active events such as solar flares and CMEs occur around large/complex active regions (Kilcik et al. 2011b). It is observed that solar cycle 24 had double peak structures. Thus, we may expect double peak structure for the temporal variation of ionospheric critical frequencies. Yiğit et al (2018) argued that f_0F_2 and hence the F_2 region is more sensitive to active sun (solar flares, CMEs), while f_0F_1 and hence the F_1 region is sensitive to quiet sun. Our findings in Figure 1 confirm their results. Kilcik et al (2018) found that during solar cycle 24 both critical frequencies were lower compared to cycle 23 (see Fig. 2 in their paper). This result indicates that the amplitude of the ionospheric frequencies (f_0F_1 and f_0F_2) is strongly correlated with the amplitude of solar activity. In addition, Burns et al (2007) emphasized that the ionospheric F_2 layer is more sensitive to geomagnetic activity and CMEs. Here we found that the number of X-ray flare show higher correlation with f_0F_2 compared to f_0F_1. Thus, we may confirm their results for solar cycle 24.

Solar flares and CMEs both are strong active events and some of them are related. High-latitude CMEs are closely associated with polar crown filaments, while low-latitude CMEs are mainly related to sunspots (Gopalswamy et al., 2010). Kilcik et al (2018) performed correlation analysis between MCMESI and f_0F_1 - f_0F_2 and found meaningful correlations (r=0.39, r=0.68, respectively) for Solar cycle 24. In this study, we obtained that the number of total solar X-Ray flares show almost the same level correlation (r=0.38, r=0.59, respectively). This result may confirm the relation between CMEs and X-ray solar flares and further we may speculate that CMEs are more effective for ionospheric critical frequencies.

In the hysteresis analysis, a large loop indicates time delay, while clockwise loops indicate that the variable on the x-axis lags behind the variable on the y-axis (Özgüç et al., 2016). Here we found 5-month time delay between f_0F_1 and solar ray flare (see Table 1) and counter-clockwise loop. For the f_0F_2 contrary results were obtained for rotation and much less time delay. The 1-month delay may explain the narrow cycle in Figure 3 and f_0F_2 follow behind the solar X-ray flares. Note that all hysteresis behaviors appear around the cycle minima. Özgüç et al. (2012) concluded that hysteresis may occur due to the fact that magnetic fields of different scales make different contributions to the total magnetic flux at various stages of the cycle. Here we confirm their results for solar cycle 24 and further suggest that the hysteresis behavior observed around minima may explained by using their argument.

References

Bachmann, K. T., Maymani, H., Nautiyal, K., & Te Velde, V. (2004). An analysis of solar-cycle temporal relationships among activity indicators. *Advances in Space Research*, *34*(2), 274-281.

Burns, A.G, Solomon, S. C., Wang, W., and Killeen. T. L. (2007). The ionospheric and thermospheric response to CMEs: Challenges and successes, J. Atmos. Sol.-Terr. Phys., 69, 77–85.

Gopalswamy, N., Akiyama, S., Yashiro, S., & Makela, P. (2010). in Magnetic Coupling between the Interior and Atmosphere of the Sun, ed. S. Hasan & R. J. Rutten (Berlin, Heidelberg: Springer Berlin Heidelberg), 289–307

Hathaway, David H. (2015). "The solar cycle." *Living reviews in solar physics* 12.1,1-87.

Ikubanni, S. O., Adebesin, B. O., Adebiyi, S. J., & Adeniyi, J. O. (2013). Relationship between F2 layer critical frequency and solar activity indices during different solar epochs. *94.20. dj; 96.60. qd*.

Kilcik, A., Yurchyshyn, V. B., Abramenko, V., Goode, P. R., Gopalswamy, N., Ozguc, A., & Rozelot, J. P. (2011a). Maximum coronal mass ejection speed as an indicator of solar and geomagnetic activities. *The Astrophysical Journal*, *727*(1), 44.

Kilcik, A., Yurchyshyn, V. B., Abramenko, V., Goode, P., Ozguc, A., Rozelot, J. P., & Cao, W. (2011b). Time distribution of large and small sunspot groups over four solar cycles, The Astrophysical Journal, 730, 30–37.

Kilcik, A., Ozguc, A., Yiğit, E., Yurchyshyn, V., & Donmez, B. (2018). Signature of a possible relationship between the maximum CME speed index and the critical frequencies of the F1 and F2 ionospheric layers: Data analysis for a mid-latitude ionospheric station during the solar cycles 23 and 24. J. Atmos. Sol.-Terr. Phys., *171*, 131-136

Kilcik, A., Chowdhury, P., Sarp, V., Yurchyshyn, V., Donmez, B., Rozelot, J. P., & Ozguc, A. (2020). Temporal and periodic variation of the MCMESI for the last two solar cycles; Comparison with the number of different class X-ray solar flares. *Sol. Phys.*, *295*(11), 1-17.

Özgüç, A., Tulunay, Y., ATAÇ, T. (1998). Examination of the solar cycle variation of foF2 by using solar flare index for the cycle 21. *Advances in Space Research*, 22.1: 139-142.

Özgüç, A., Ataç, T. and Pektaş, R. (2008). "Examination of the solar cycle variation of foF2 for cycles 22 and 23." J. Atmos. Sol.-Terr. Phys., 70.2-4, 268-276.

Özgüç, A., Kilcik, A. and Rozelot, J. P. (2012). "Effects of Hysteresis Between Maximum CME Speed Index and Typical Solar Activity Indicators During Cycle 23." *Sol. Phys.*, 281.2, 839-846.

Özgüç, A., Kilcik, A., Georgieva, K., & Kirov, B. (2016). Temporal Offsets Between Maximum CME Speed Index and Solar, Geomagnetic, and Interplanetary Indicators During Solar Cycle 23 and the Ascending Phase of Cycle 24. *Sol. Phys.*, *291*(5), 1533-1546.

Whitten R. C., Poppoff I. G. (1965). Physics of the Lower Ionosphere, Prentice- Hall, Inc. Englewood Cliffs, N. J.

Yiğit, E., Kilcik, A., Elias, A. G., Dönmez, B., Ozguc, A., Yurchshyn, V., & Rozelot, J. P. (2018). Critical frequencies of the ionospheric F_1 and F_2 layers during the last four solar cycles: Sunspot group type dependencies. J. Atmos. Sol.-Terr. Phys., *171*, 157-163.

Morning Polar Substorms and Their Possible Mid-Latitude Effects

Kleimenova N.G.[1], Despirak I.V.[2], Malysheva L.M.[1], Gromova L.I.[3], Gromov S.V.[3], Lubchich A.A.[2], Guineva V.[4], Werner R.[4]

[1]Schmidt Institute of Physics of the Earth, RAS, Moscow, Russia; e-mail: kleimen@ifz.ru
[2]Polar Geophysical Institute, Apatity, Russia
[3]Pushkov Institute of Terrestrial Magnetism, Ionosphere, and Radio Wave Propagation, Moscow, Troitsk, Russia
[4]Space Research and Technology Institute, Bulgarian Academy of Sciences, Stara Zagora Department, Bulgaria

Abstract

The specific type of high-latitude magnetospheric substorms (i.e., negative magnetic bays) have been found above ~70° MLAT in the local morning under the absence of the magnetic activity at the lower latitudes. Thus, they are observed on the contracted auroral oval as the nighttime polar substorms. But, unlike polar substorms, the morning polar bays were recorded under both positive and negative IMF *Bz* with different spatial distribution and nature. The high-latitude morning polar bays, observed under the negative IMF *Bz*, could be the result of an azimuthal expansion of the "classical" night substorms to the morning side of the Earth. The morning polar negative bays just like polar substorms were accompanied by mid-latitude positive bays. However, the morning polar bays, observed after a period of long lasting non-variable negative IMF *Bz* in the absence of "classical" night substorms, could be attributed to develop of, so called, "convection" substorms. In this case, there were no positive mid-latitude magnetic bays, i.e., the absence of a substorm current wedge, as well as in the case of the morning polar bays, recorded under the positive IMF *Bz* and being the result of an azimuthal expansion of the daytime polar magnetic bays.

Keywords: magnetic substorm, interplanetary magnetic field, mid-latitude positive bay

1. Introduction

It is well known that during the low magnetic activity, the night-side magnetosphere substorms and visible auroras are observed at the geomagnetic latitudes higher than the normal auroral oval location so that the auroral oval becomes contracted and poleward shifted. In earlier publications, these high-latitude substorms have been termed as "substorms on contracted oval" [e.g., Akasofu et al., 1973; Lui et al., 1976], later on they were known as "polar substorms" [Kleimenova et al., 2012; Despirak et al., 2014; Safargaleev et al., 2020].

Our study of the ground-based observations showed that the polar substorms are observed not only in the night, but also in the local morning as negative magnetic bays, recorded at the high-latitudes above ~70° MLAT in the absence of magnetic disturbances at the lower latitudes. We called such bays, "morning polar substorm" because they often demonstrate some typical substorm behavior. While there is a number of papers dedicated to the research of the different aspects of the evening polar substorms, the morning ones remain practically unknown.

The aim of this paper is to study the behavior and sources of the ***morning polar substorms*** basing on the IMAGE magnetometer data (http://space.fmi.fi/image/).

2. Main behavior of morning polar substorms and their occurrence

Figure 1a presents the geographic map of the IMAGE station on which our study was based, and Figure 1b shows the example of a morning polar substorm. It is seen that the negative magnetic bays are observed only at BJN-NAL stations. Their absence at lower latitudes indicates that these bays are not the result of the polar expansion of a 'classical' substorm. We found that morning polar bays are usually observed at low solar wind speeds (V < 450 km/s) like nighttime polar substorms.

We selected 112 cases of morning polar bays registered in 2006-2012. Their daily variations are shown in Figure 1c demonstrating the maximum of occurrence at 08-09 MLT, i.e., before the local magnetic noon. Unlike "classical" substorms, the morning polar substorms were characterized by small amplitudes (less than 200-300 nT) and the gentle onset and end.

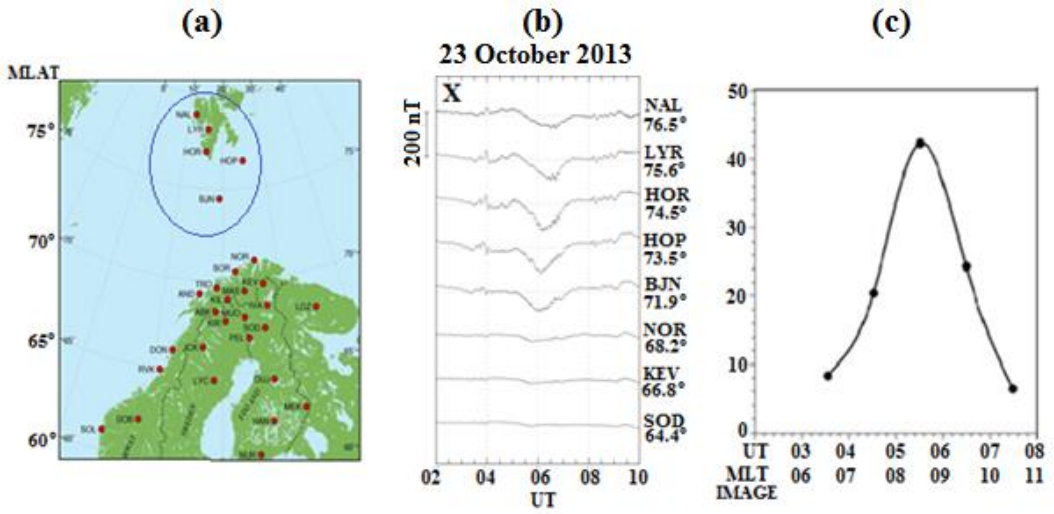

Figure 1. *(a) The map of the IMAGE magnetometer station location; (b) the example of a morning polar substorm at the IMAGE stations (c) the daily distribution of these substorms occurrence.*

To study the global distribution of geomagnetic activity during the morning polar bays, we used magnetic registration data from 66 communication satellites of the AMPERE (*Active Magnetosphere and Planetary Electrodynamics Response Experiment)* project, simultaneously operating at altitudes of 780 km [e.g., Anderson et al., 2014]. In our work, we used the AMPERE project data (http://ampere.jhuapl.edu/products) as the maps of the distribution of geomagnetic disturbances summarized in 10 min with 2 min shift and the results of a spherical harmonic analysis of magnetic measurements. The Field Aligned Currents (FAC) are calculated from these data: currents flowing into the ionosphere (inward currents) are shown in blue on the maps, and currents flowing out (outward currents) in red.

During 2010-2017 AMPERE measurements, we selected 48 events of the appearance of morning polar magnetic bays identified at the high-latitude IMAGE stations (BJN-NAL). The analysis of global geomagnetic activity during the studied morning polar substorms showed that their sources could be various perturbations in the magnetosphere, namely, "classical" nighttime substorms, convective bays and daytime polar negative bays.

3. Morning polar substorms under the southward IMF

Magnetospheric substorms developing in the nighttime sector may be also observed in a large longitudinal interval, from the local evening to the late morning. Thus, the morning polar magnetic bays recorded on the IMAGE profile can be the result of the azimuthal continuation of nighttime disturbances in the morning direction. The analysis of the global distribution of

magnetic activity based on the AMPERE data confirmed this assumption. We found 5 events of the morning polar substorms on the IMAGE profile, where the enhanced electrojet and FACs were recorded in the night and morning according to AMPERE data. An example of such event on October 23, 2013 is shown in Figure 2a.

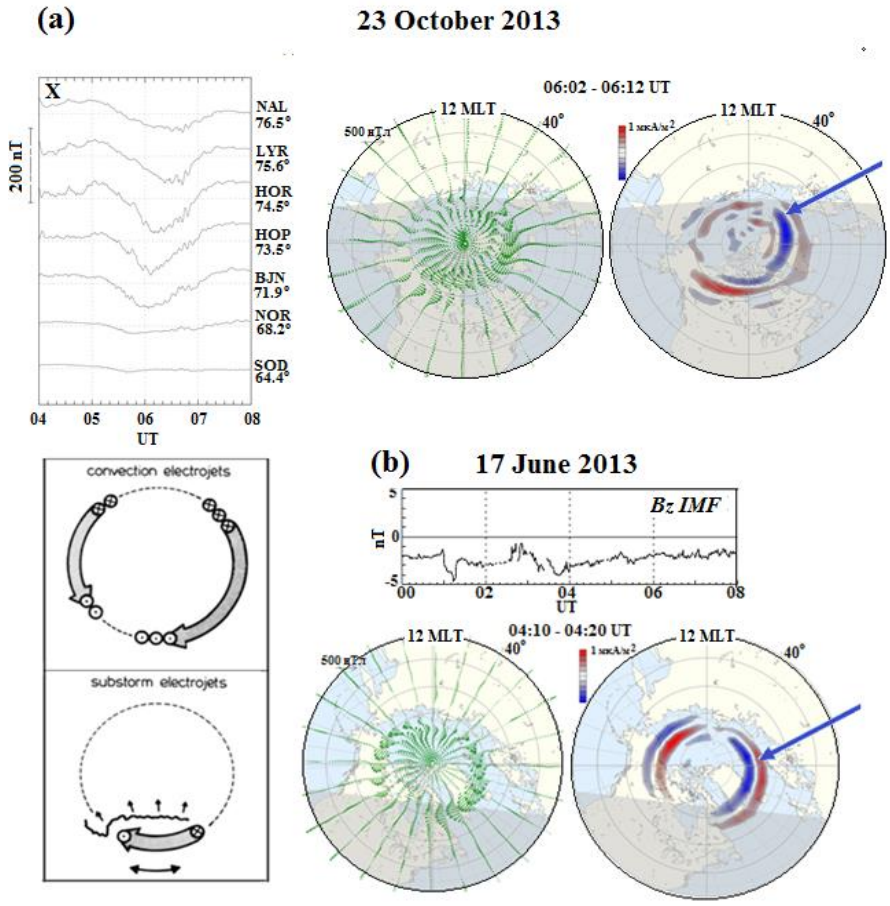

F**igure 2**. *(a) - The IMAGE magnetogram and AMPERE maps of results of the spherical harmonic analysis of magnetic measurements and distributions of the Field Aligned Currents on 23 October 2013; (b) – the convection and substorm currents diagram adopted from [Baumjohann, 1983] and AMPERE maps for event on 17 June 2013.*

The AMPERE maps (Figure 2a, right) show that at this time, the westward electrojet (a "classical" substorm) and enhanced FACs were observed from the evening sector to the late morning sector (IMAGE meridian). Before midnight (at 20-23 MLT), the high-latitude westward electrojet was accompanied by a lower-latitude eastward electrojet, which is a substorm current wedge (SCW) typical of a “classical” substorm [McPherron et al., 1973; Rostoker et al., 1980].

It is well known that in the high-latitude ionosphere, plasma convection is almost constantly observed, which has the form of a two-vortex structure [e.g., Heppner, 1977] with vortex centers in the morning and evening sectors, and increases with an increase in the southward IMF. Long periods (several hours) of the stable state of the southern IMF contribute to the continuous supply of energy to the magnetotail and the establishment of the regime of the so-called "steady magnetospheric convection" discussed in many papers [e.g., Yahnin et al., 1994; Sergeev et al., 1996]. Some of its intensifications were called "convective bays" [Pytte et al., 1978; Baumjohann, 1983]. The convective bay represents the development of a two-vortex current system with vortex centers in the morning (the westward electrojet) and evening (the

eastward electrojet) sectors, as shown in the diagram in Figure 2b adopted from [Baumjohann, 1983].

We found 6 events when magnetic disturbances were observed simultaneously at the morning and afternoon sectors in their absence in the local night, that is typical for the enhanced convection. One of such events on June 17, 2013 is shown in Figure 2b. All morning convective negative bays were not accompanied by positive magnetic bays at the middle latitudes.

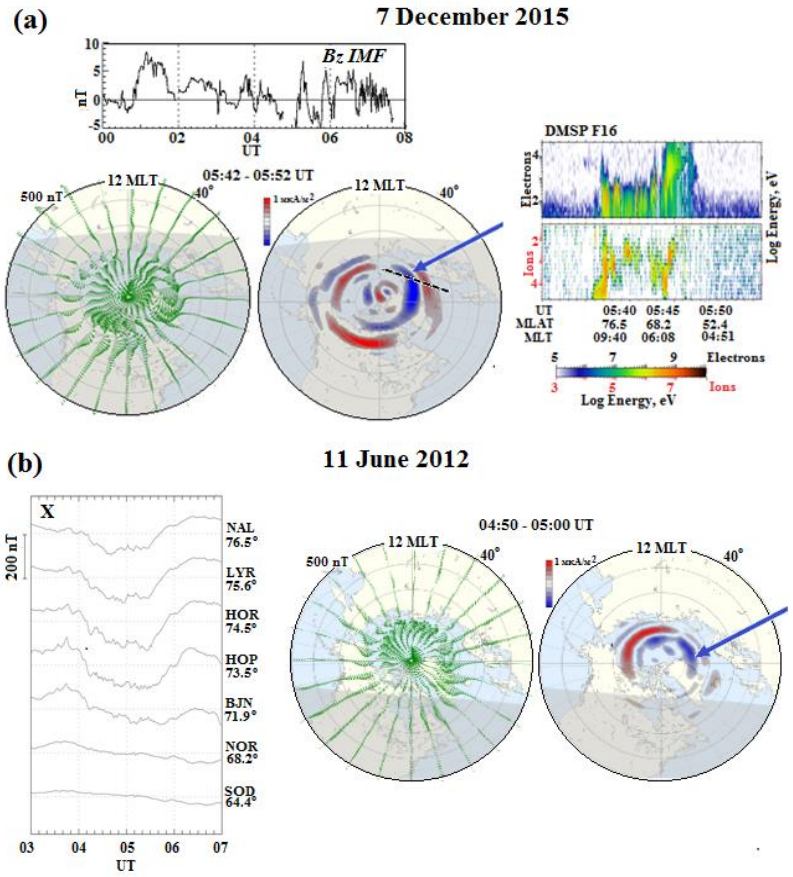

Figure 3. *(a)- An example of the global distribution of magnetic disturbance and field-aligned currents according to AMPERE data, as well as variations in IMF Bz on 7 December 2015 and the spectrograms of precipitating electrons and ions measured by the low-apogee DMSP F16 satellite (http://sd-www.jhuapl.edu/Aurora/spectrogram); (b) - the same as in Figure 2a but on 11 June 2012.*

An analysis of the observational data showed that most (32 events out of 48) of the morning polar substorms were a superposition of disturbances caused by the interaction of nighttime substorm and convective phenomena, the separation of which is a very complex, not always solvable problem, especially in disturbed conditions. Figure 3a shows an example of such complex case (December 7, 2015), when geomagnetic disturbances were recorded by the AMPERE data simultaneously in the morning, evening, and afternoon sectors.

At that time, the low-apogee (~830 km) DMSP F16 satellite [Redmon et al., 2017] measured the fluxes of precipitating particles over Svalbard at the beginning of the morning polar substorm. In Figure 3a, the descending part of the orbit is shown schematically; the satellite first crossed the region of downward FACs (shown in blue), and then the region of upward ones (shown in red). The AMPERE data shows that at that time, an intense eastward current was observed in the nighttime sector southward from the westward electrojet. That is a typical

picture of the development of the substorm current wedge. It stretches across North America, from the west to the east.

4. Morning polar substorms under the northward IMF

Under the northern IMF direction, magnetic bay-like high-intensity disturbances can be observed in the near-noon sector of the polar latitudes [e.g., Friis-Christensen et al., 1985, Levitin et al., 2015; Gromova et al., 2017, 2019], the time variations and sign of which are usually controlled by the IMF *By* component. An analysis of the AMPERE data showed that the ionospheric electrojet and enhanced field-aligned currents can be observed in a fairly wide daytime longitudinal region from the morning sector to afternoon one as it is shown in Figure 3a. It is seen that the morning negative bay could be the result of the azimuthal expansion of the daytime polar electrojet into the morning sector and they did not accompany by positive magnetic bays at the middle latitudes.

4. Possible mid-latitude effect of morning polar substorms

It is well known that the main feature of a substorm current wedge (SCW) is the development of mid-latitude positive magnetic bays. The most considered morning polar negative magnetic bays associated with an azimuthal expansion of "classical' night-side substorms have been found accompanied by positive mid-latitude magnetic bays in the *X*-component, but with a strong negative amplitude of the *Y*-component. That can indicate that the center of SCW is located far eastward. One of such events is presented in Figure 4. The *X*-component was stronger at BEL (47.7° MLAT) than at PAG (42.6° MLAT).

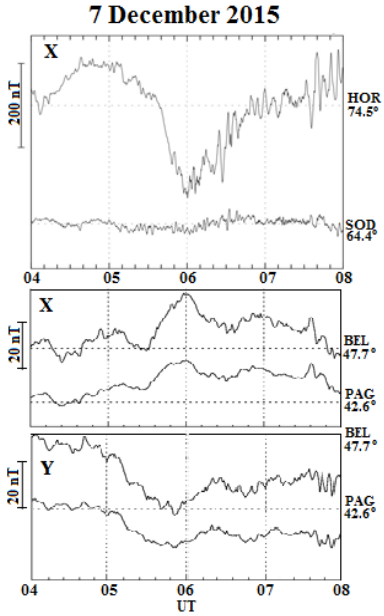

***Figure 4**. Magnetograms from polar- and mid-latitude stations on 7 December 2015.*

5. Summary

At latitudes above ~70° MLAT, the polar substorms can be observed not only in the evening, but in the morning as well with the maximum of occurrence at ~08-09 MLT. The morning events are recorded both under the negative and positive IMF *Bz*.

Under the negative IMF *Bz*, the *morning* polar substoms can be a result of an azimuthal expansion of *nightside* "classical" substorms (in that case they are accompanied by mid-latitude positive magnetic bays) as well as a result of an enhancement of the magnetosphere convection without the mid-latitudes effects.

Under the positive IMF *Bz*, the *morning* polar substoms are a result of an azimuthal expansion of *dayside* polar magnetic bays controlled by IMF *By*).

The majority of the morning polar substorms are a superposition of “classical” substorms and convective negative bays.

Acknowledgments

This study was supported by the RFBR (project number 20-55-18003) and National Science Fund of Bulgaria (NSFB) (project number КП-06-Русия/15).

References

Akasofu, S.-I., Perreault, P.D., Yasuhara, F., Meng, C.I. (1973). Auroral substorms and the interplanetary magnetic field, J. Geophys. Res.. Vol 78, No 31, pp. 7490-7508, https://doi.org/10.1029/JA078i031p07490

Anderson, B.J., Korth, H., Waters, C.L., Green, D.L. et al. (2014). Development of large-scale Birkeland currents determined from the Active Magnetosphere and Planetary Electrodynamics Response Experiment, Geophys. Res. Lett., Vol 41, No 9, pp. 3017-3015, https://doi.org/10.1002/2014GL059941

Baumjohann, W. (1983). Ionospheric and field-aligned current systems in the auroral zone: A concise review , Adv. Space Res. Vol 2, No 10, pp. 55-62. https://doi.org/10.1016/0273-1177(82)90363-5

Despirak, I.V., Lyubchich, A.A., Kleimenova, N.G. (2014). Polar and high latitude substorms and solar wind conditions, Geomagn. Aeron., Vol 54, No 5, pp. 575-582. https://doi.org/10.1134/S0016793214050041

Friis-Christensen, E., Kamide, Y., Richmond, A.D, Matsushita, S. (1985). Interplanetary magnetic field control of high-latitude electric fields and currents determined from Greenland magnetometer data, J. Geophys. Res.. Vol 90, No A2. pp. 1325-1338, https://doi.org/10.1029/JA090iA02p01325

Gromova, L.I., Kleimenova, N.G., Levitin, A.E. et al. (2017). High-latitude daytime magnetic bays as effects of strong positive IMF Bz: case study , Sun and Geosphere, Vol 12, No 7, pp.125-131.

Gromova, L.I., Gromov, S.V., Kleimenova, N.G., Dremukhina, L.A. (2019). Response of the high-latitude daytime magnetic bays to the IMF By: Case study, Sun and Geosphere, Vol 14. No 7, pp. 31-36, https://doi.org/10.31401/SunGeo.2019.01.05

Heppner, J.P. (1977). Empirical model of High-latitude electric field, J. Geophes. Res. Vol 72, No 7, pp. 1115-1125, https://doi.org/10.1029/JA082i007p01115

Kleimenova, N.G., Antonova, E.E., Kozyreva, O.V et al. (2012). Wave structure of magnetic substorms at high latitudes, Geomagn. Aeron., Vol 52, No 6, pp. 746-754, https://doi.org/10.1134/S0016793212060059

Levitin, A.E., Kleimenova, N.G., Gromova, L.I. et al. (2015). Geomagnetic disturbances and pulsations as a high-latitude response to considerable alternating IMF variations during the magnetic storm recovery phase (Case study: May 30, 2003) .Geomagn. Aeronom. Vol 55, No 6, pp. 755-768, https://doi.org/10.1134/S0016793215060092

Lui, A.T.Y., Akasofu, S.-I., Hones, E.W., et al. (1976). Observation of the plasma sheet during a contracted oval substorm in a prolonged quiet period, J. Geophys. Res.. Vol 81, No 7, pp. 1415-1419, https://doi.org/10.1029/JA081i007p01415

McPherron, R.L., Russell, C.T., Aubry, M.P. (1973), Satellite studies of magnetospheric substorms on August 15, 1968: 9. Phenomenological model for substorms, J. Geophys. Res., Vol 78, No 16, pp. 3131-3149, https://doi.org/10.1029/JA078i016p03131

Pytte, T., McPherron, R.L., Hones, E.W., West, I. (1978). Multiplesatellite studies of magnetospheric substorms: Distinction between polar magnetic substorms and convection-driven negative bays, J. Geophys. Res., Vol 83, No 11, pp. 5256-5268. https://doi.org/10.1029/JA083iA11p05256.

Redmon, R.J., Denig, W.F., Kilcommons, L.M., Knipp D.J. (2017). New DMSP database of precipitating auroral electrons and ions, J. Geophys. Res. Space Physics, Vol 122, pp. 9056-9067, https://doi.org/10.1002/2016JA023339.

Rostoker, G., Akasofu, S.-I., Foster, J. et al. (1980). Magnetospheric substorms: Definitions and signatures, J. Geophys. Res., Vol. 85, pp.1663-1668, https://doi.org/10.1029/JA085iA04p01663

Safargaleev, V.V, Kozlovsky, A.E., Mitrofanov, V.M. (2020). Polar substorm on 7 December 2015: preonset phenomena and features of auroral breakup, Ann. Geophys., Vol 38, No 4, pp. 901-917. https://doi.org/10.5194/angeo-38-901-2020

Sergeev, V.A., Pellinen, R.J., Pulkkinen, T.I. et al. (1996). Steady magnetospheric convection: review of recent results , Space Sci.. Rev., Vol 75. pp. 551-604, https://doi.org/10.1007/BF00833344

Yahnin, A.G., Malkov, M.V., Sergeev, V.A. et al. (1994). Features of Steady Magnetospheric Convection, J. Geophys. Res., Vol 99, pp. 4039-4951, https://doi.org/10.1029/93JA02868

Dependence of the Ionospheric Scintillations Intensity of Cosmic Radio Sources on their Position in the Sky

Lytvynenko O., Panishko S., Derevyagin V.

URAN-4 Observatory, Institute of Radioastronomy NASU; uran4@te.net.ua

1. Abstract

Our report presents the results of the experimental dependence of the ionospheric scintillations intensity of cosmic radio sources on their position in the visible celestial hemisphere. The results refer to the mean geographical latitudes and decameter range of radio waves. The intensity of ionospheric scintillations is represented by the index S_4. We used the data obtained by us from long-term systematic observations of a group of compact space sources at the URAN-4 radio telescope. The selected space sources have right ascension coordinates that differ by 5 ... 7 hours, which ensures continuous radio astronomy monitoring of the ionosphere.

We used long series of data and statistical analysis. This was due to the strong stochastic variability of the ionospheric scintillations intensity in time intervals from an hour to several days and the seasonal-daily effect

For suppress the seasonal-diurnal influence data smoothing was applied over a time interval equal to a year. The obtained dependence of the scintillation index on the position of cosmic radio sources in the visible celestial hemisphere was demonstrated of the dominant role of the geomagnetic field.

Keywords: radio sources; ionospheric scintillations; geomagnetic field

2. Introduce

The presence of irregularities of the electron concentration in ionospheric plasma caused the scattering of radio waves which propagate through the ionospheric layer. As a result, on the Earth's surface the interference pattern occurs which moves and changes in time. Thereby amplitude and phase of received signal fluctuates. This is called amplitude and phase ionospheric scintillations. On the one hand, the scintillations carry information about heterogeneous structure of ionosphere and their dynamics. This is used in the investigations on physics of the ionosphere and cosmic weather. On the other hand, scintillations are interfering factor in the operation of the radio communication, radar, satellite navigation systems and also in the fulfilling of the radio astronomical studying.

Despite more than half a century of history of ionospheric scintillation investigations [Crane R. K., 1977, Aarons J., 1982, Yeh K. C., Liu C.H., 1982] and the successes achieved this topic remains relevant, including for improving efficiency of observations and data processing in decametric radio astronomy.

Purpose of this work was the experimental studying of the dependence of intensity of ionospheric scintillation of cosmic radio sources from their position on the celestial hemisphere. Research is related to the middle latitudes and decametric range of radio waves.

The scintillation index S_4 was used as a characteristic of the scintillation intensity:

$$S_4 = \langle u(t)\rangle^{-1}\sqrt{\langle(u(t) - \langle u(t)\rangle)^2\rangle},$$

u (t) – output signal of the radiometer that is proportional to flux density of radiation.

For space-homogeneous fluctuations of the electron concentration in the range F_{max} и E_s the model is known in which scintillation index is proportional to thickness of the scattering layer:

$$S_4 \propto h_0 \frac{1}{\cos\theta},$$

θ – zenith angle of cosmic source, h_0 – thickness of the scattering layer при θ = 0.

Space anisotropy of ionospheric irregularities that conditioned by geomagnetic field is another factor which influences on the character of radio wave scattering [Jun Liang, Weixing Wan, 1997, Bezrodny V.G., 1987]. Known results of the studying of influence of ionospheric irregularities anisotropy on scintillation intensity in general relate to the upper geographical latitudes [Bezrodny V.G. et al., 2008] and exposure experiments on ionosphere by powerful radiation [Erukhimov L.M. et al., 1979, Alimov V.A. et al., 2011], and also to another wave ranges [Milikh G. et al., 2008].

In this work it is considered experimental dependences of the ionospheric scintillation index S_4 from zenith angle θ of radio source and angle δ between geomagnetic field vector and line of sight of the radio source. Initial data was obtained during the long-term observations of group of the power cosmic radio sources on the RT URAN-4.

Radio telescope URAN-4 is an element of VLBI network of radio telescopes of decametric wave range «URAN» (Ukraine Radio Interferometers of Academy of Sciences) and it is placed near Odessa, Ukraine (geographical coordinates 46° 23' 50"N, 30° 16' 24"E). Frequency range of RT is 10-30 MHz. Phased array antenna consists from 128 broadband turnstile dipoles with two orthogonal linear polarizations. Antenna array has sizes 240 m along East-West direction and 28 m along Nord-South direction. Maximum effective area is 7300 square meters. The width of direction pattern in zenith direction at the frequency 25 MHz is 24° x 3°. Broadband phasing system of the antenna array provides automatic switching of the direction pattern within visible hemisphere. Used radiometer implemented as a short-base interferometer that allows suppressing the galactic noise.

Figure 1 shows the projection on a geographical map of the transillumination area of ionosphere during observations of radio sources on RT URAN-4. In the plane of geomagnetic meridian, Figure 2 presents the geometry of considered task about the dependence of intensity of radio source ionospheric scintillations from their position on the sky. For similar figure in the plane of geographical meridian the angle values will differ little from angle values in Figure 2, and instead of line of sight and geomagnetic field vector their projection on plane of the geographical meridian will used.

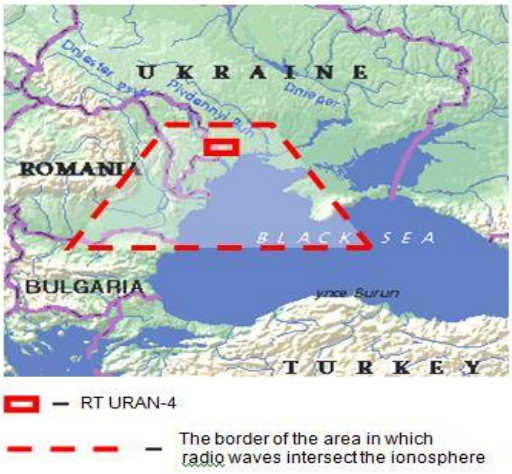

Figure 1. *Area of the ionosphere monitoring during the observation of power cosmic radio sources on the RT URAN-4. Limits of this area marked by dashed line and the rectangle – location of the RT URAN-4*

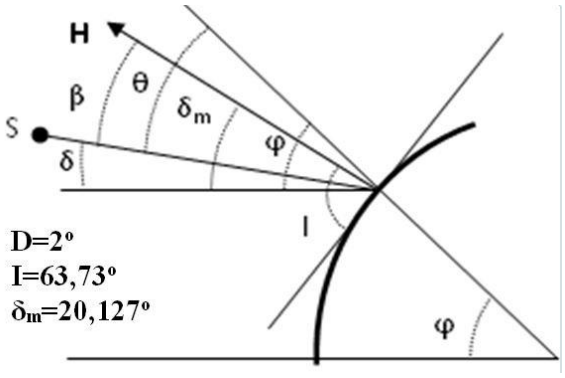

Figure 2. *Geometry of the considered effect. Here marked: D –magnetic declination; I – magnetic inclination;* ***H*** *– geomagnetic vector;* δ_m *– angle between* ***H*** *and equator plane,* $\delta_m = I - (90^o - \varphi)$*;* $\varphi_g \approx \varphi$ *– geographical latitude; S – source line of sight;* θ *– zenith angle of source;* δ *– angle between line of sight and equator plane;* β *– angle between* ***H*** *and line of sight*

3. Observations and data processing method

Observations of a source on the RT URAN-4 carry out simultaneously at two frequencies (20 and 25 MHz) by switching of antenna direction pattern (DP) to fixed positions on the line of source transit. These positions correspond to given hour angles of source and follow through fixed time intervals. As a result a source repeatedly crosses DP, example of observation of one radio source during day presents on the Figure 3. Each of such crossing (scan) registered by the receiving equipment.

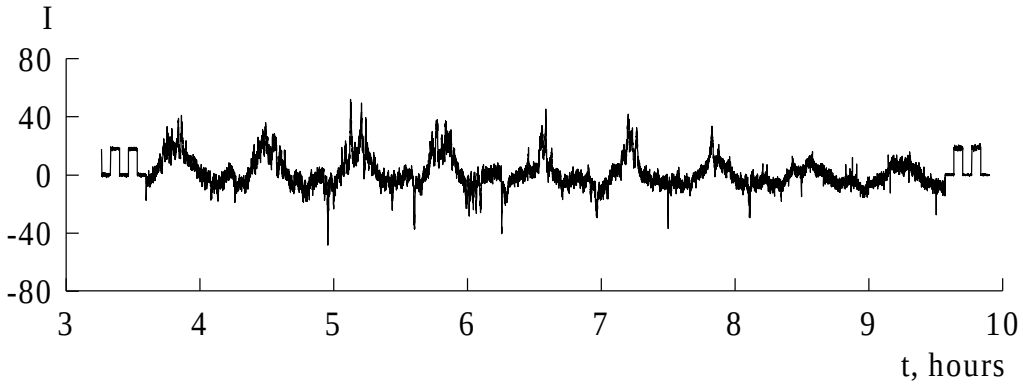

Figure 3.*Example of the record of the radio source 3C 274 passage through fixed positions of the RT direction pattern (scans) during day 05.01.2004 at the frequency 20 MHz. Impulse in the beginning and in the end of scans – calibration.*

Intensity of the ionospheric scintillations depends on many factors. These are direct influence of solar radiation, processes related with cosmic weather changes, interaction with troposphere and magnetosphere, anthropogenic influence, own dynamic processes in the ionosphere. Thus changes of scintillation characteristics in general have random character. The statistical approach is widely used in connection with this for studying of dependences in the scintillation behavior. Figure 4 shows separated radio source scans with weak and strong intensity of ionospheric scintillations that reflects the state of ionosphere during observations.

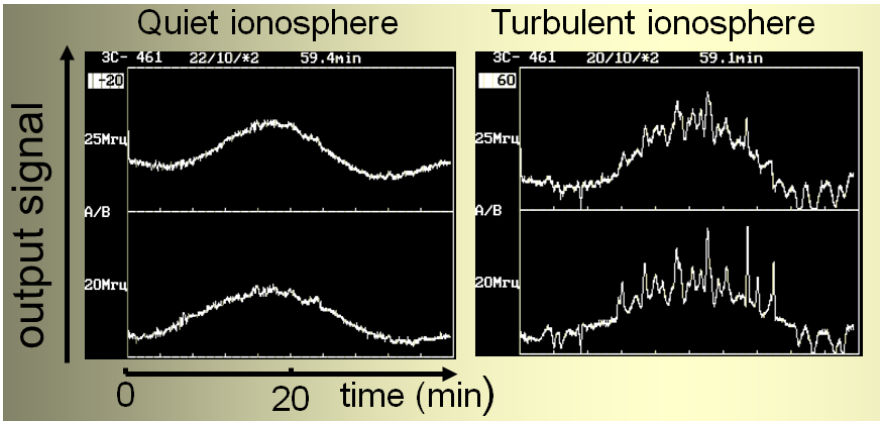

Figure 4. *Examples of separate records of radio source 3C 461 passage through RT direction pattern.*

Further the method of DP fitting used for processing of each individual scan that allows the determination of the radio emission flux and scintillation parameters including the one discussed here index S_4 (Figure 5). Moreover, the DP fitting allows suppressing some kind of interference.

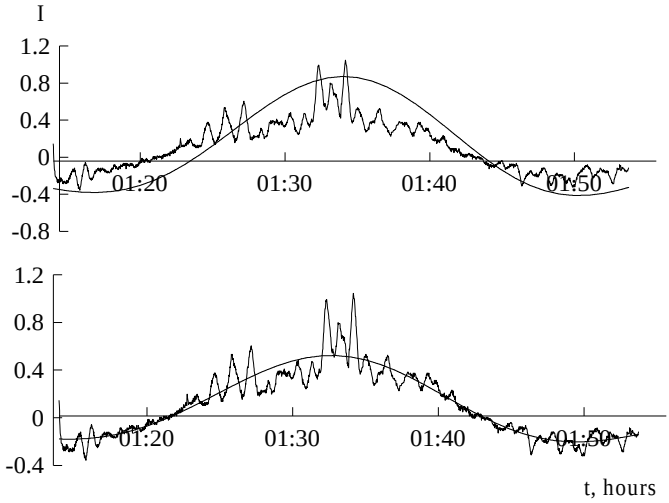

Figure 5. *Example of fitting of RT direction pattern function at the processing of the separate record*

In monitoring mode on the RT URAN-4 the long-term observations of group of the power cosmic radio sources were carried out among them two supernova remnants 3C 144 (Taurus A), 3C 461 (Cassiopeia A) and two radio galaxies 3C 274 (Virgo A), 3C 405 (Cygnus A). The radiometer as a short-base interferometer was used which suppresses the galactic noise. Data obtained on the radiometer was applied for the estimation of the ionosphere scintillation characteristics. Distances between sources on the right ascension are about 6-7 hours. This allows the carrying out observations around the clock. The general characteristics of the observed radio sources are presented in Table 1 such as equatorial coordinates (right ascension α and declination δ), flux density at two frequencies F, distance R, and also zenith angle in culmination time θ_0 and angle with magnetic field in culmination time $\beta_0 = \delta - \delta_m$.

Table 1. *General characteristics of observed radio sources*

Radio source	Coordinates, epoch 2000		F, Jy		R	θ_0	β_0
	α	δ	20 MHz	25 MHz			
3C 144	$05^h34^m31.4^s$	22°00'54"	3420	3420	2 кпс	24.4°	1.84°
3C 274	12 30 49.4	12 23 30	5300	4700	12 Мпс	34.0	7.36
3C 405	19 59 28.4	40 44 00	32000	31500	260 Мпс	5.7	20.54
3C 461	23 23 41.0	58 52 00	58000	51000	3400 кпс	-12.4	38.52

4. Results and their analysis

Analyzing the obtained data, we tried to elucidate the role of two effects in the distribution of the scintillation intensity of cosmic radio sources in the celestial hemisphere. The first effect is the dependence of the scintillation intensity on the thickness of the scattering layer (the thickness depends on the zenith angle of the source). The second effect is the features of radio wave scattering by anisotropic ionospheric inhomogeneities due to the presence of the geomagnetic field.

The first thing that can be done is for each source to obtain the dependence of the flicker index on the hour angle of the source (the hour angle of the middle of the scan).

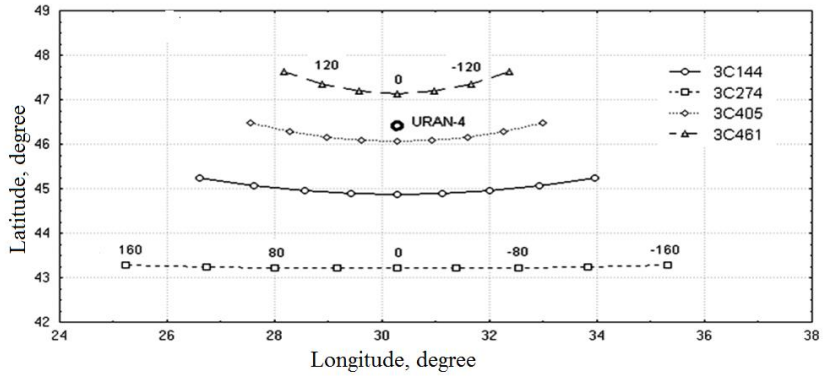

Figure 6. *Geodetic coordinates of points in which radio track of source-radio telescope crosses conditional surface $F2_{max}$ in ionosphere*

The lines in Fig. 6 are the tracks of the sounding of the ionosphere by the radio astronomical method. The icons are the fixed positions of the radio telescope beam, the numbers next to them are the values of the hour angles in minutes. Finding the beam in a fixed position (scan duration) for 3C 461 is 60 min., for other radio sources - 40 min.

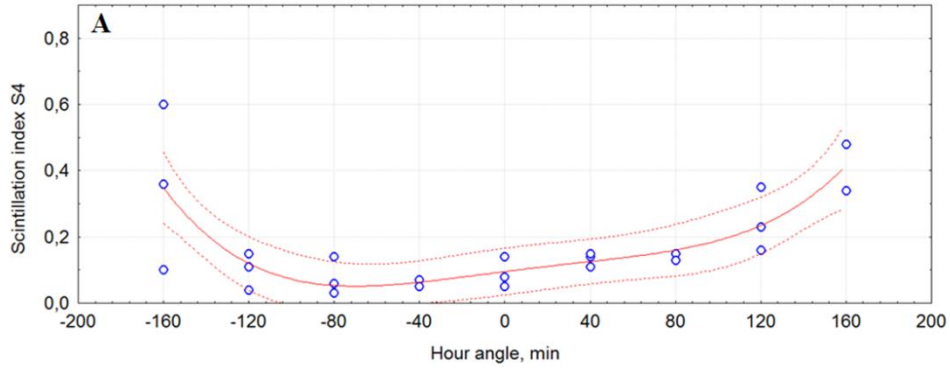

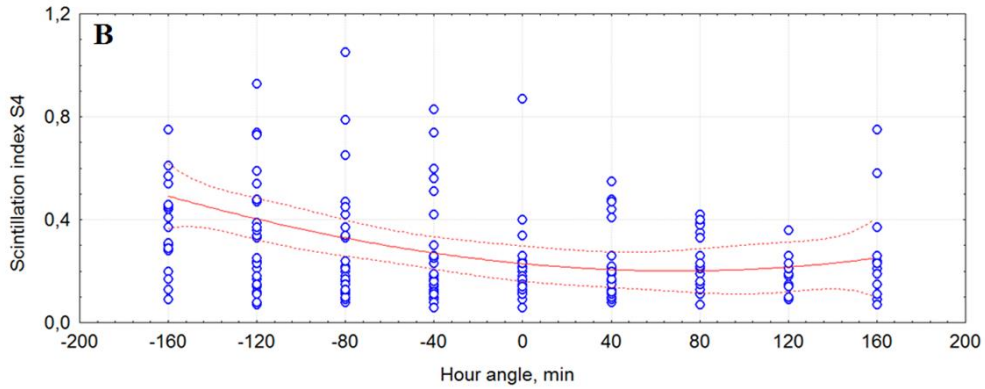

Figure 7. *Dependence of the scintillation index from hour angle for radio source 3C 405: left – sampling per first quarter of year; right – half-year sampling*

Figure 7 shows the dependences of the scintillation index on the hour angle of the source. We can expect a symmetric picture with respect to the zero hour angle if the changes in S4 were stationary over the observation period.

Data in panel A refer to the spring season Data in panel B mainly refer to the second half of the year. At short time intervals, S4 variations are strongly pronounced. As the time interval increases, the variations in S4 decrease. These variations are due to the strong seasonal-daily influence on the scintillation intensity, which violates the stationary nature of the change in S4. This is well confirmed by the long-term data series shown in Fig. 8 obtained with the URAN-4 radio telescope, in which the seasonal-diurnal effect is clearly manifested.

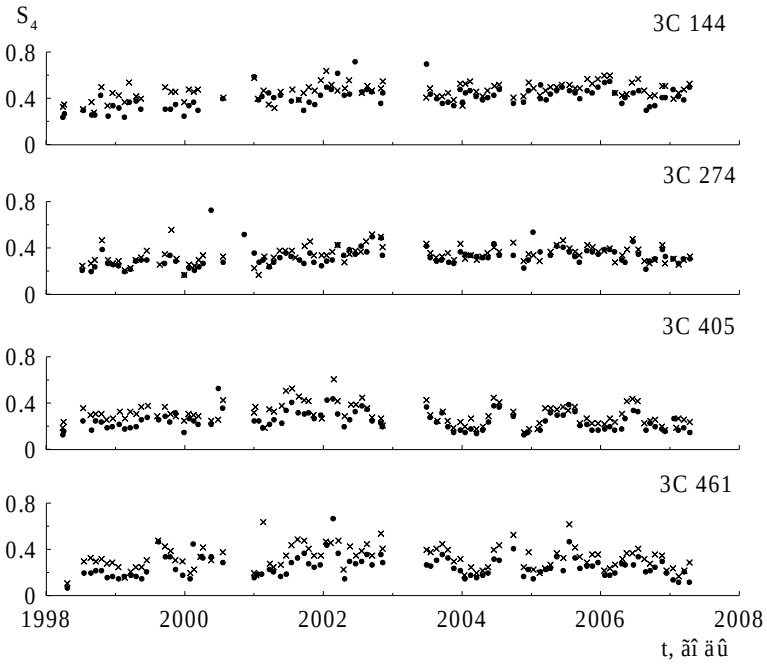

Figure 8. *Effect of seasonal-daily dependence for ionospheric scintillations intensity*

To reveal the dependence of the scintillation intensity on the position of the source in the celestial hemisphere, it is necessary to get rid of the seasonal-daily influence on the observation results. This can be done using samples that are multiples of one year. In this case, the averaged data will not depend on the seasonal-daily effect.

On Fig. Figure 9 shows the dependence of the mean values of the scintillation index on the hour angle of the source, obtained from a one-year sample. The symmetry of the graph indicates

the suppression of the seasonal-daily effect. The data presented below were obtained from samples of several full years.

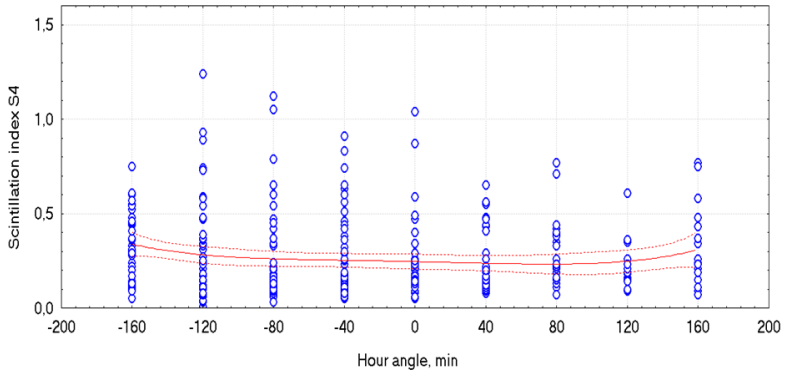

Figure 9. *Yearly sampling obtained for radio source 3C 405.*

The experimental dependence of the scintillation index on the zenith angle (Figure 10) for sources with a large angle β is close to the calculated curve obtained for the effect of changing the thickness of the scattering layer. For sources with β < 15o, the experimental dependence does not correspond to the calculated curve (it can be assumed that in this case the effect of anisotropy of ionospheric inhomogeneities, caused by the influence of the geomagnetic field, dominates).

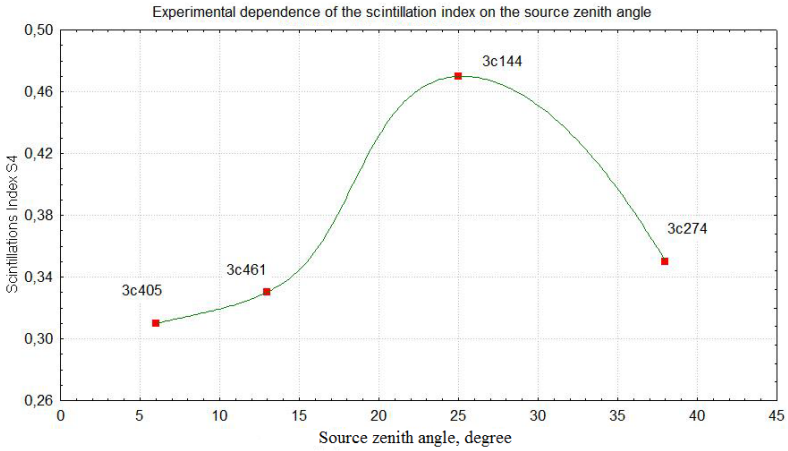

Figure 10. *Experimental dependence of scintillation index from source zenith angle obtained from observations on the RT URAN-4 during 1998-2007:*

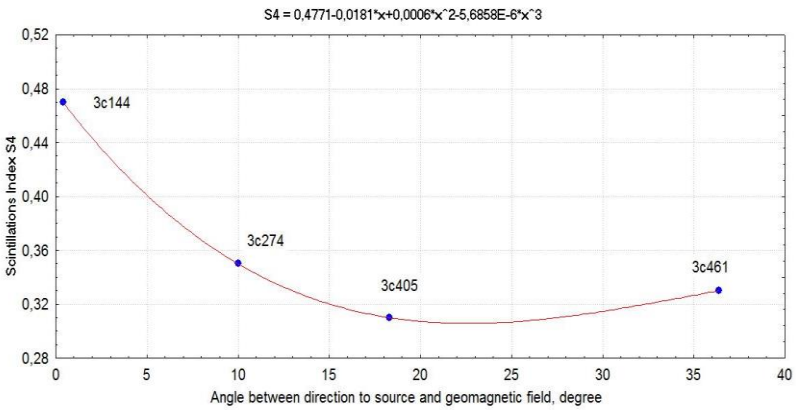

Figure 11. Experimental dependence of the average annual values of S4 on the angle β between the line of sight of the radio source and the geomagnetic field vector, obtained from observations on the URAN-4 RT from 1998 to 2007

It should be noted that the deviation of the line of sight of the source from the direction of the geomagnetic field β and the zenith angle of the source θ are related by a functional dependence, and the plots S4(β) and S4(θ) contain information about both the influence of the scattering layer thickness and the anisotropy of inhomogeneities. It is difficult to separate these influences on the basis of the results presented, but the analysis of the graphs shows that each of them has a monotonous section, which can be interpreted as related to the dominance of one of the influencing effects. The boundary of these sections lies in the region $\beta = 15^o$. Therefore, when estimating the scintillation intensity depending on the position of the radio source in the celestial hemisphere, one should use the graph S4 (θ) for $\beta > 15^o$, and the graph S4(β) for $\beta < 15^o$

5. Conclusions

1. To analyze the dependence of the intensity of ionospheric scintillations on the position of the radio source in the celestial hemisphere, we used data from long-term observations on the URAN-4 RT (geographic latitude 46o, decameter wave range).

2. Experimental dependences of the intensity of ionospheric scintillations on the zenith angle of the radio source θ and on the angle between the line of sight and the geomagnetic field vector β are obtained.

3. The boundary value β is determined, separating the positions of the source on the celestial hemisphere, for which either the effect of the thickness of the scattering layer or the effect of anisotropy of ionospheric inhomogeneities dominates.

References

Aarons, J. (1982). Global morphology of ionospheric scintillation, Proc. IEEE, Vol. 70, pp. 360-378.

Bezrodny V.G., Charkina O.V., Galushko V.G., Groves K, Kashcheyev A.S., Watkins B., Yampolski Y.M., Murayama Y. (2008). Application of an imaging HF riometer for the observation of scintillations of discrete cosmic sources, Radio Sci., DOI:10.1029/2007RS0037.

Crane R. K. (1977). Ionospheric Scintillation, Proc. IEEE, Vol. 65, No. 2, pp. 180-204.

Liang Jun, Wan Weixing. (1997). HF propagation and scattering in a turbulent ionosphere with an anisotropic and inhomogeneous background, Radio Science, Vol. 32, No. 3, pp. 1011-1021.

Milikh G., Gurevich A., Zybin K., Secan J. (2008). Perturbations of GPS signals by the ionospheric irregularities generated due to HF-heating at triple of electron gyrofrequency, Geophysical Research. Letters, Vol. 35, L22102, DOI:10.1029/2008GL035527

Yeh, K. C., Liu C. H. (1982). Radio wave scintillation in the ionosphere, Proc. IEEE, Vol. 70, No. 4, pp. 324-360.

Alimov V.A., Zynychev V.A., Mytiakov N.A., Mytiakov S.N. (2011). Small scale turbulence in the upper ionosphere, Izvestia vuzov. Radiophyzika, Vol. LIV, No. 10, pp. 741-745.

Bezrodny V.G. (1987). Scintillations of radioastonomical sources on the anisotropic irregularities of the ionospheric plasma, Izvestia vuzov. Radiophyzika, Vol. 30, No. 8, pp. 939-946.

Erukhimov L.M., Metelev S.A., Mytiakova E.E. at al. (1979). Experimental investigations of the artificial ionospheric turbulence, in book «Thermal non-linear phenomena in plasma», Gorky: IPP AS SSSR, pp. 7-45.

Overview of the Space Radiation Extreme Events Observed with Liulin Type Instruments

Dachev T.P.[1], Tomov B.T.[1], Matviichuk Y.N.[1], Dimitrov P.G.[1], Mitev M.G.[1], Semkova J.V.[1] Koleva R.T.[1], Jordanova M.M.[1], Bankov N.G.[1], Krastev K.[1], Malchev S.[1], Mitrofanov I.[2], Litvak M.[2], Kozyrev A.[2], Golovin D.[2], Benghin V.V.[3], Shurshakov, V.A.[3]

[1]Space Research and Technology Institute BAS, Sofia, Bulgaria, E-mail: tdachev@bas.bg
[2]Space Research Institute, Russian Academy of Sciences, Moscow, Russia
[3]State Research Center Institute of Biomedical Problems, Moscow, Russia

1. Abstract The paper presents the space radiation extreme events observed with Liulin type instruments. The following events, characterized by fast increase of the dose rate were classified as extreme: solar energetic particles (SEP) events, relativistic electron enhancements (REE) and burst type REE in the outer radiation belt (ORB). We compare the dose rates data from 4 SEP events in 1989, 2012, 2015 and 2022, 2 REE events in 2010 and 2015 and 1 burst type REE in 2015. All data were selected to cover periods of 6 hours and 30 minutes that are the average continuation of the extra vehicle activities (EVA) on the ISS. The time intervals were chosen to coincide with the maximum of the observed dose rates during different events. Only the REE1 event data was chosen simultaneously with real EVA-1 of STS-131 astronauts on April 9 2010. The dose rates data in the inner and the outer radiation belt maxima measured by RADOM instrument in 2008 at about 3,000 and at about 20,000 km altitude, respectively, are compared with the extreme events data.

2. Introduction

In the other space two radiation sources are observed - galactic cosmic ray (GCR) and solar energetic particle (SEP). Both sources are populated mainly by high-energy protons. In the near Earth space environment two additional radiation sources exists-the inner (mainly energetic protons) (IRB) and other (mainly relativistic electrons (ORB) radiation belts. We study the fast enhancements in proton and electron sources and call them "Extreme".

The source selection procedure described by [Dachev et al. 2017] was used and the result of the separation of the four radiation sources is seen in Figure 1b. In the Figure 1a the variations of the disturbance storm-time (Dst) index (in nanotesla) are presented (https://wdc.kugi.kyoto-u.ac.jp/index.html). From Fig. 1b, is seen that the most stable are the daily dose rate variations in the GCR source with a heavy black dotted line in the bottom of Fig. 1b. The next relatively 'stable' source is the IRB source, seen with a moving average green line over two points in the lower part of Figure 1b. The most dynamic is the ORB source. Well seen anti correlation with the Dst index is observed because the ORB source is filled up by relativistic electrons during magnetic storms. Two of the fast enhancements "Extreme" in the ORB source named REE2 and Burst REE are object of study in the paper.

There are two major measurement systems developed by the Bulgarian team until this moment [Dachev et al., 2015]. The first one is based on one detector and is known as Liulin type Deposited Energy Spectrometer (DES) [Dachev et al., 2002, 2017, 2020], while the second one is dosimetric telescope (DT) by 2/3 detectors [Semkova et al., 2007, 2012, 2018]. The cited above papers are easy accessible that is why we will not go in details for the instrumentation description in this paper. The Liulin experiments names used here are LIULIN, Liulin-5, Liulin-MO, RADOM, R3DR1 and R3DR2.

3. Overview of the extreme events observed with Liulin type instruments

3.1. SEP event observed by LIULIN instrument on MIR SS on 30 September 1989

The first observation of SEP event was made with the Bulgarian-Russian dosimeter-radiometer LIULIN (see Fig. 2), which was installed in the working compartment of the MIR

space station [Dachev et al., 1989]. The detector unit (LIULIN-DU) is a miniature, portable, self-indicating device. The LIULIN-microcomputer unit (LIULIN-MCU) is an eight-bit microprocessor unit. (One of the first microcomputers in the Bulgarian space instrumentation practice.) The LIULIN-DU use a surface-barrier silicon detector in the form of a 0.3 mm thick disk with an area of 2-cm^2 and dose sensitivity of 10^{-9} Gy/pulse. LIULIN was in active operation on MIR space station from 1989 to 1994.

The period of September-October 1989 was marked by a series of 3 SEP events, which were the most significant over the period of observations since the known SEP of August 1972 [Shurshakov et al., 1999]. The most powerful was the SEP on 19 October 1989. Unfortunately, there are LIULIN data only fort the first part of this SEP. That is why here we analyze the data obtained on 30 September 1989. Also, the SEP maxima on 24 June 2015.

Fig. 2 presents 10-sec resolution data obtained in the time interval between 00:30 and 07:00 hour UT on 30 September 1989 when the maximal SEP dose rate was observed [Dachev et al. 1972]. The vertical axes covers seven orders of magnitude and is same for all figures in the paper to allow easier comparison among them. Two correlating parameters are plotted in the figure – the measured dose rate and the L-value of the point of observation. The dose rate data are selected to be larger than 20-μGy h^{-1} that is why eight coinciding maxima are seen in both parameters.

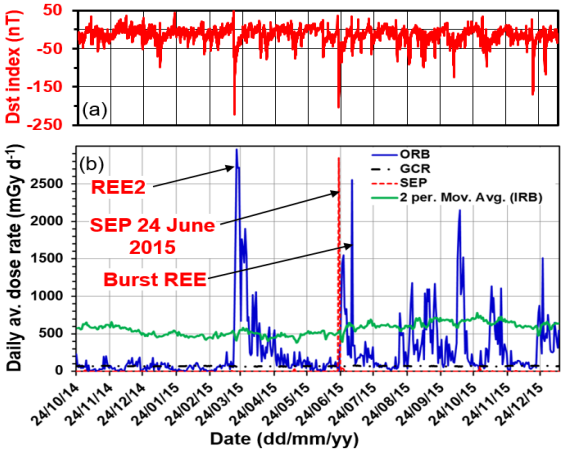

Fig. 1.

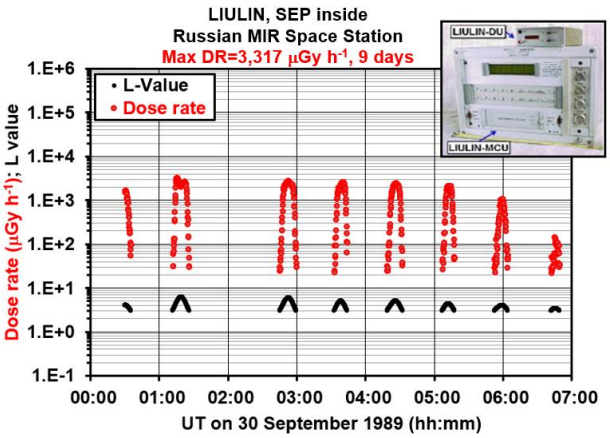

Fig. 2.

Figure 1a. *Daily Dst index variations;* ***Figure 1b.*** *Daily GCR, IRB, ORB and SEP dose rate variations as measured by R3DR2 instrument on Russian segment of ISS. Some of the extreme events studied in the paper are marked.* ***Figure 2.*** *External view of the LIULIN dosimeter radiometer and dose rate data dynamics during the SEP on 30 September 1989.*

The reason for the reduction of the SEP dose rates, toward lower L values is the geomagnetic shielding, measured by the vertical cutoff rigidity [Smart & Shea, 2005]. The vertical cutoff rigidity decreases at the higher L values. As a result, large amount of SEP protons, including the low-energy protons, penetrates to the MIR orbit altitude and produces the high latitude maximum in the absorbed SEP dose rate. In the region of lower L-values due to the large magnetic field and respectively vertical cutoff rigidity, the low-energy SEP particles are deflected by the magnetic field outside the magnetosphere and dose rate is decreased.

3.2. SEP event observed by Liulin-5 DT instrument on ISS on 12 March 2012

Liulin-5 DT instrument (see Fig. 3) [Semkova et al., 2007, 2012] was launched to the Russian segment of ISS in May 2007. Measurements with Liulin-5 were conducted in the spherical tissue equivalent phantom of Matroshka- R experiment located in the PIRS-1 module of the Russian segment of ISS.

During the SEP events of 7-12 March 2012 at L>3 the particle flux and dose rates increased in all three detectors of Liulin-5 charged particle telescope located at 40, 60 and 165 mm depths

along the radius of the tissue-equivalent spherical phantom in MIM1 module of Russian segment of ISS.

Fig. 3 presents 30-sec resolution data obtained in the time interval between 12:59 and 19:29 hour UT on 7 March 2012 when the maximal SEP dose rate was observed [Semkova et al., 2012]. The dose rate data are presented in the same way as in Fig. 2. Simple comparison show that the dose rates in the 2012 SEP event are about 1 and half order of magnitude smaller than the 1989 dose rates, independently that the GOES 6 and GOES 16 proton fluxes for energies larger than 10 MeV are similar (pls. see first column of Table 1).

3.3. SEP event observed by R3DR2 instrument in ESA EXPOSE-R2 platform outside Russian segment of ISS on 22 June 2015

Fig. 4 presents 10-sec resolution data obtained by R3DR2 instrument in the time interval between 16:57 and 22:27 hour UT on 22 June 2015 [Dachev et al., 2016]. The green line in Fig. 3 presents the measured on GOES-16 >10 MeV proton flux when the maximal SEP dose rate was observed.

The studied SEP event is remarkable by the low energy proton fluxes. The method for estimation of the proton energy [Haffner, 1971, Dachev et al., 2017] allowed to be calculated the energy of the SEP protons at the surface of the R3DR2 instrument detector. The blue points in Fig. 4 shows that close to the SEP maxima the proton energy have a local minimum with mean energies of 7-8 MeV. The small energy of the SEP protons in June 22 event is confirmed by Prof. Semkova. She mentioned in a private communication that the Liulin-5 DT inside RS of ISS do not observe enhanced proton flux during the time of the event.

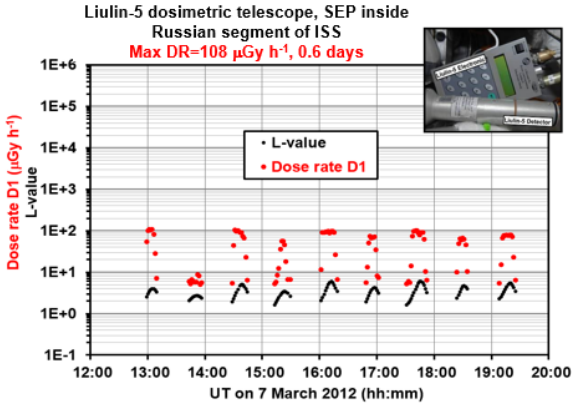

Fig. 3.

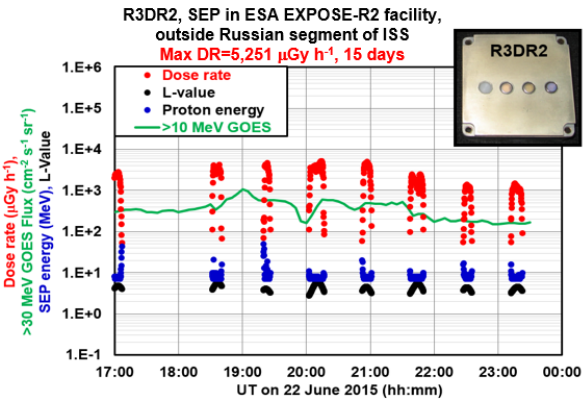

Fig. 4.

Figure 3. *External view of the Liulin-5 dosimetric telescope and dose r1te data dynamics during the SEP on 7 March 2012.* ***Figure 4.*** *External view of the R3DR2 dosimeter and dose rate data dynamics during the SEP on 22 June 2015;*

3.4. SEP event observed by Liulin-MO dosimetric telescope in 400 km Mars circular orbit outside ESA-Roscosmos ExoMars TGO satellite in February 2022

Solar prominence was seen by the Full Sun Imager of the Extreme Ultraviolet Imager on board the ESA/NASA Solar Orbiter spacecraft at about 22:00 UT on 15 February 2022 (https://www.esa.int/ESA_Multimedia/Images/2022/02/Solar_Orbiter_captures_giant_solar_eruption). This is the largest solar prominence eruption ever observed in a single image together with the full solar disc. The coronal mass eruption (CME) propagated in northeast direction, includes the ecliptic. Its speed was about 1000 km s^{-1} and the consequent shock wave accelerated the SEP that reached Mars orbit where Liulin-MO instrument worked outside ESA-Roscosmos ExoMars TGO satellite.

Fig. 5 presents 60-sec resolution SEP dose rate data in the Liulin-MO dosimetric telescope (DB direction of the telescope) [Semkova et al., 2018]. The data was obtained at 400 km Mars circular orbit outside ESA-Roscosmos ExoMars TGO satellite. All data set between 12 UT on 15 February and 12 UT on 17 February is shown with heavy black line, while the 6 hours and

30 minutes similar to EVA time interval close to the maximum of the SEP event with heavy red line.

In the left part of Fig. 5, the small dose rate data present the GCR conditions, which is characterized by average dose rate value of 15.8-μGy h^{-1}. Further, the dose rate increase in result of registration of solar energetic protons, reach maximal value of 1,355-μGy h^{-1} and slowly decrease toward GCR levels out of the time shown in Fig. 5.

3.5. Inner and other Radiation belts observation by RADOM instrument outside Indian Moon satellite Chandrayaan-1 on 22 October 2008

The Indian Moon Chandrayaan-1 spacecraft was launched on 22 October 2008 and injected into a 255-22,860 km preliminary orbit. The **RAD**iati**O**n **M**onitor (RADOM) is a miniature (110x40x20 mm, 0.1 kg) dosimeter-spectrometer (pl. see fig 6), which was switched "ON" two hours after the launch. In Fig. 6 dose rate, dose to flux and altitude data are presented in the UT time interval 18:00-00:30 on 22 and 23 October 2008.

The analysis shows that in the left part of Fig. 6 are observed high doses and fluxes with time resolution of 10-sec. We interpret these dose rates as generated by predominating relativistic electrons in the ORB at altitude above 20,000 km, because the specific doses are less than one nGy cm^2 $particle^{-1}$ [Haffner, 1971]. The doses here reach maximum values of 43,568-μGy h^{-1}. Gradually from left to right in Fig. 6 when the satellite moves toward the slot region and next reached the IRB maximum where high-energy protons are observed. The dose rate here reaches 125,699-μGy h^{-1}, while the dose to flux is few nGy cm^2 $particle^{-1}$.

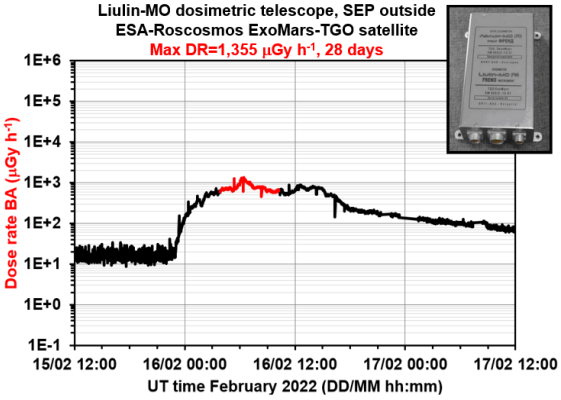

Fig. 5.

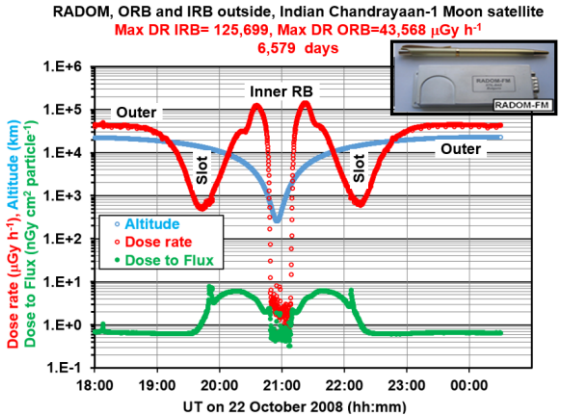

Fig. 6.

Figure 5. *External view of the Liulin-MO dosimetric telescope and dose rate data dynamics during the SEP on 16 February 2022.* ***Figure 6.*** *External view of the RADOM dosimeter and dose rate data dynamics during the crossings of the inner and outer radiation belts on Indian Chandrayaan-1 Moon satellite on 22 June 2015.*

When the satellite crosses the altitudes of about 2000 km, a drastic decrease of doses and fluxes occur because it moves below the ORB maximum. Further motion of the satellite toward the perigee brings the minimal observed dose rate values of about 12-μGy h^{-1} corresponding to the usual GCR dose rates. After the crossing of the perigee region at about 250 km, altitude the satellite starts to move back to the proton and electron belts where the dose rates rise again to the values observed at the left part of Fig. 6.

3.6. Relativistic electron enhancements observation by R3DR1/R2 instruments in ESA EXPOSE-R1/R2 facilities outside Russian segment of ISS

Fig. 7 presents 10-sec resolution data obtained by R3DR1 instrument in the time interval between 05:31 and 11:58 hour UT on 9 April 2010. It is seen that the maxima in the dose rate correlate well with the L-value and anticorrelate by the Dose to Flux value, showing minima less than 1 nGy cm^2 $particle^{-1}$. This according to Heffner's formulae [Heffner, 1971] confirm that the predominate particle population in the dose rate maxima are relativistic electrons. The

REE in April 2010 collected data simultaneously with real EVA-1 of STS-131, April 9 2010 between 05:31 and 11:58 UT (https://www.nasa.gov/pdf/440897main_sts_131_press_kit.pdf).

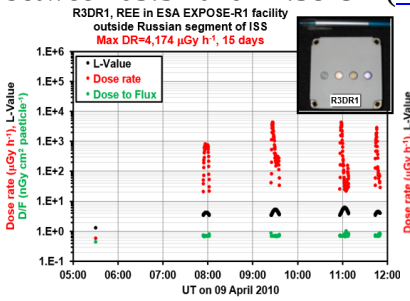

Fig. 7.

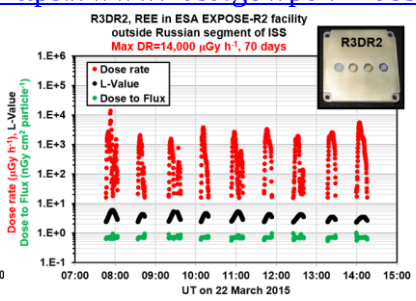

Fig. 8.

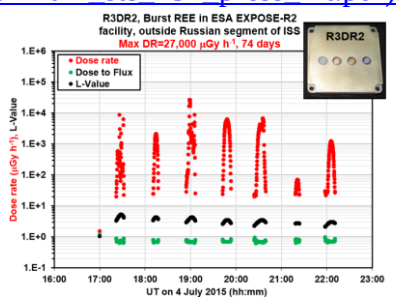

Fig.9.

Figure 7. *External view of the R3DR1 dosimeter and dose rate data dynamics during the REE1 on 9 April 2009;* ***Figure 8.*** *External view of the R3DR2 dosimeter and dose rate data dynamics during the burst REE2 on 4 July 2015;* ***Figure 9.*** *External view of the R3DR2 dosimeter and dose rate data dynamics during the REE2 on 22 March 2015.*

Table 1. Summarized data for SEP (red) and REE (blue) events. The ISS daily averaged dose of 177-μGy h^{-1} in the last column is averaged value from data in Table 2 of Reitz et al., 2005.

Instrument name and its shielding. GOES >10 MeV proton or >2 MeV electron flux (cm^2 s^{-1} sr^{-1})	Event type, Date UT from-to	Max. Observed dose rate/Min. allow. (μGy h^{-1}) Remark	Accumulated dose (mGy) for 6h and 30m	Calculated number of days inside ISS
Inside "MIR" SS; >15 g cm^2; "LIULIN" GOES-6: >10 MeV proton flux=1000-2000 >100 MeV proton flux=300-400	SEP, 30/09/1989 00:30-07:00	3,317/20 The largest dose rate on MIR.	1.72	10
Inside RS of ISS; >20 g cm^2; "Liulin-5" (First detector). GOES-15: >10 MeV proton flux=1000-2000 > 100 MeV proton flux=30-40	SEP, 07/03/2012 12:59-19:29 6 h 30 m	108/5	0.114	0.6
Outside ISS ESA, inside EXPOSE-R2 0.25-0.5 g cm^2; R3DR2 GOES-15: >10 MeV proton flux=200-500 >100 MeV proton flux=0.01-0.02	SEP 22/06/2015 16:57-22:27	5,251 The largest observed on ISS proton dose rate	2.84	16
Outside ESA-Roscosmos ExoMars 0.5-1 g cm^2; Liulin-MO	SEP, 16/02/2022	DB=1,355 DC=1,375	5.07	28
Outside Indian Moon Chandrayaan-1 0.5-1 g cm^2; RADOM	IRB & ORB, 22-23/10/2008 18:00:00:30	125,699 43,568	1,184	6,690
Outside ISS, inside ESA EXPOSE-R1 0.25-0.5 g cm^2; R3DR1 GOES-15 electron flux=10^4-10^5	REE1, 09/04/2010 05:31-11:58 (in the time of STS-131 EVA-1)	4,174	2.66	15
Outside ISS, inside R3DR2 in ESA EXPOSE-R2, 0.25-0.5 g cm^2; GOES-15 electron flux=10^2-10^3	Burst type REE 04/07/2015 17:00-23:30	27,020 The largest observed on ISS electron dose!	13.3	75
Outside ISS, inside ESA EXPOSE-R2 0.25-0.5 g cm^2; R3DR2	REE2, 22/03/2015 07:46-13:46	14,000	12.6	71

Fig. 8 and Fig. 9 looks very similarly to Fig. 7 because similar REE events are observed. It is necessary to mention that the Burst REE on 4 July (Fig. 8) is the only one seen in the Liulin data. It is formed by seven maxima, classified as "Precipitation bands" [Dachev, 2018]. The PB were identified as rapid (10-40-sec) dose rate enhancement from the normal (20–200 μGy h^{-1}) ORB level and similar fast return to the same low level. Only PB that have in the time profile dose rates larger than 10,000-μGy h^{-1}, identical to flux larger than 4000 cm^{-2} s^{-1}, for 10 or more seconds were selected. 23 PB were found in the R3DR1/R2 data sets.

Conclusions

The main conclusion of the presented data is that the REE events bring more accumulated dose in 6 hour and 30 minutes. The maximal SEP accumulated dose of 15 mGy outside ISS is equal to the minimal REE1 accumulated dose. The fact that the new phenomena of burst REE brings the maximal accumulated dose of 74 mGy was unexpected. From other hand, the much

smaller penetration of the relativistic electrons in the bodies of astronauts brings much smaller health effects.

Although the obtained relativistic electron doses do not pose extreme risks for the astronauts, being on EVA, they have to be considered as a permanently detected radiation source, which requires additional comprehensive investigations.

The accumulated doses during all studied extreme events on the MIR, ISS and in Mars orbit are incomparable with the doses during the crossings of the IRB and ORB maxima at 3,000 and 22,000 km respectively. This explain why the manned missions at low earth orbit are kept at altitudes below 500 km.

Acknowledgements

The work in Bulgaria is partially supported by grant KP-06-Russia 24 (Project No. 129 for bilateral projects with Russia) of the National Science Fund of Bulgaria.

References

Dachev, T.P., Matviichuk, Y.N., Bankov, N.G., Semkova … Machmutov, V.S., 1992. MIR Radiation dosimetry results during the solar proton events in September–October 1989. Advances in Space Research, 12(2-3), pp.321-324. https://doi.org/10.1016/0273-1177(92)90122-E

Dachev T.P., Tomov… F., Spurny, (2002). Calibration Results Obtained With Liulin-4 Type Dosimeters. Adv. Space Res. 30, No 4, 917-925. http://dx.doi.org/10.1016/S0273-1177(02)00411-8.

Dachev, T.P., Tomov, B.T., Matviichuk … Angelis G.De, (2011). An overview of RADOM results for Earth and Moon Radiation Environment on Chandrayyan-1 Satellite, Adv. Space Res., 48, 5, 779-791. http://dx.doi.org/10.1016/j.asr.2011.05.009

Dachev, T.P., Semkova…Kubancak, I. N. (2015). Overview of the Liulin type instruments for space radiation measurement and their scientific results. Life Sciences and Space Research, 4, 92–114. https://doi.org/10.1016/j.lssr.2015.01.005.

Dachev, T. P., Tomov, B.T., Matviichuk, Y.N., Dimitrov, P.G., & Bankov, N.G., (2016). High dose rates obtained outside ISS in June 2015 during SEP event, Life Sciences in Space Research, 9, 84-92. http://dx.doi.org/10.1016/j.lssr.2016.03.004.

Dachev, T.P., Bankov, N.G., Tomov, B.T., Matviichuk, Y.N., Dimitrov, P.G., Häder, D.-P, Horneck, G., (2017). Overview of the ISS radiation environment observed during the ESA EXPOSE-R2 mission in 2014–2016. Space Weather, **15**, 1475–1489. https://doi.org/10.1002/2016SW001580.

Dachev, T.P., (2018). Relativistic electron precipitation bands in the outside radiation environment of the international space station. Journal of Atmospheric and Solar-Terrestrial Physics, 177, pp.247-256. https://doi.org/10.1016/j.jastp.2017.11.008

Dachev, T.P., Tomov, B.T., Matviichuk, Y.N., Dimitrov, P.G., Semkova, J.V., Koleva, R.T., Jordanova, M.M., Bankov, N.G., Shurshakov, V.A. and Benghin, V.V., (2020). Solar modulation of the GCR flux and dose rate, observed in space between 1991 and 2019. Life Sciences in Space Research, 26, 114-124, 2020. https://doi.org/10.1016/j.lssr.2020.06.002.

Haffner, J.W., (1971). Yadernoe izluchenie i zashchita v kosmose, pp 115, Atomizdat, Moscow.

Reitz, G., Beaujean, R., Benton, E., Burmeister, S., Dachev, T., Deme, S., Olko, P., (2005). Space radiation measurements on-board ISS-the DOSMAP experiment. Radiat Prot. Dosimetry 116, 374–379. https://doi.org/10.1093/rpd/nci262.

Semkova, J., R. Koleva… I. Chernykh, Status and calibration results of Liulin-5 charged particle telescope designed for radiation measurements in a human phantom onboard the ISS, Advances in Space Research, 40, 2007, 1586–1592. http://dx.doi.org/doi:10.1016/j.asr.2007.01.008.

Semkova, J., Koleva, R., Maltchev, St., Bankov, N., Benghin, V., et al., (2012). Depth dose measurements with the Liulin-5 experiment inside the spherical phantom of the Matroshka-R project onboard the International Space Station, Adv. Space Res., 49, 471–478. http://dx.doi.org/10.1016/j.asr.2011.10.005.

Semkova, J., Koleva, … Malakhov, A., (2018). Charged particles radiation measurements with Liulin-MO dosimeter of FREND instrument aboard ExoMars Trace Gas Orbiter during the transit and in high elliptic Mars orbit, Icarus, 303, pp.53-66. https://doi.org/10.1016/j.icarus.2017.12.034.

Shurshakov, V.A., Petrov, V.M., Ivanov, Y., Bondarenko, V.A., Tzetlin, V.V., Makhmutov, V.S., Dachev, T.P. and Semkova, J.V., (1999). Solar particle events observed on MIR station. Radiation measurements, 30(3), 317-325. https://doi.org/10.1016/S1350-4487(99)00058-X

Smart, D.F. and Shea, M.A., (2005). A review of geomagnetic cutoff rigidities for earth-orbiting spacecraft. Advances in Space Research, 36(10), 2012-2020.

Observation of Solar Energetic Particle Events Onboard ExoMars TGO in July 2021-March 2022

Semkova J.[1], *Koleva R.*[1], *Benghin V.*[3], *Krastev K.*[1], *Matviichuk Yu.*[1], *Tomov B.*, *Bankov N.*[1], *Dachev T.*[1], *Maltchev S,*[1], *Mitrofanov I.*[2], *Malakhov A.*[2], *Kozyrev A.*[2], *Golovin D.*[2], *Mokrousov M.*[2], *Sanin A.*[2], *Litvak M.*[2], *Nikiforov S.*[2], *Lisov D.*[2], *Anikin A.*[2], *Shurshakov V.*[3], *Drobyshev S.*[3]

[1]Space Research and Technology Institute, Bulgarian Academy of Sciences, Sofia, Bulgaria, jsemkova@stil.bas.bg
[2]Space Research Institute, Russian Academy of Sciences, Moscow, Russia
[3]State Research Center, Institute of Biomedical Problems, Moscow, Russia

1. Abstract

The dosimeter Liulin-MO for measuring the radiation environment onboard the ExoMars TGO is a module of the Fine Resolution Epithermal Neutron Detector (FREND). Here we present results from measurements of the charged particle fluxes, dose rates and estimation of dose equivalent rates at ExoMars TGO Mars science orbit, provided by Liulin-MO since May 2018. The period of measurements covers the declining and minimum of the solar activity in 24th solar cycle and the inclination phase of the 25th cycle. Particular attention is drawn to the observation of the solar energetic particle (SEP) events in July, September and October 2021, February and March 2022 as well as their effects on the radiation environment on TGO during the corresponding periods. The SEP event on 15-19 February 2022 is the most powerful event observed in our data. Compared are the time profiles of the particle fluxes and count rates measured by Liulin-MO and the neutron detectors of FREND during these events. The data for SEP events on TGO in July 2021-March 2022 contribute to the details for the solar activity at a time when Mars is on the opposite side of the Sun from Earth.

Keywords: *dosimetric measurements; Mars orbit; solar energetic particles*

2. Introduction

The exploration of Mars gets on a new wider scale nowadays. The radiation environment during the transit, on Mars and its vicinity can be very hazardous for future human exploration of the red planet. Because of its thin atmosphere and the lack of global intrinsic magnetic field, Mars is very exposed to space radiation. In the interplanetary space and on Mars orbit the radiation field consists of two types of primary particles: galactic cosmic rays (GCRs) and solar energetic particles (SEPs). SEPs are sporadic and impulsive events and take place much more frequently during the active phase of the solar cycle. SEPs are mainly protons, electrons and α particles with energy typically ranging from 10 to several hundreds of MeV. GCRs generally originate from outside the Solar System, e.g. in supernova remnants, and their composition consists [Badhwar and O'Neill, 1992] mainly of protons (85%–90%) and α particles (about 11%), with about 1% electrons and another 1% heavy ions. In the Solar system GCR flux is isotropic and in the long term their flux and spectra show modulation that anti-correlates with the solar activity, the modulation being more efficient to the low-energy GCR.

The radiation environment on a transit orbit to Mars and on Mars surface have been studied since 2012 by MSL RAD instrument [Zeitlin et al. 2013, Guo et al, 2017, 2021].

The radiation environment at Martian orbit has been previously measured onboard Mars Odyssey, whose radiation detector, the Martian Radiation Environment Experiment, stopped working under the SEP event of October 2003, but data could still be retrieved from the Gamma Ray Spectrometer and the scintillator component of the High Energy Neutron Detector (HEND)

[Zeitlin et al., 2010]. Recent studies have also analyzed data from Mars Express [Knutsen et al., 2021]. The ExoMars TGO spacecraft launched in April 2016 carries the FREND instrument, one module of the latter being the Liulin-MO dosimeter [Mitrofanov et al., 2018], that has provided and providing in-situ measurements of the radiation environment during the TGO interplanetary travel and in Martian orbit [Semkova et al., 2018, 2021]. Since May 2018 Liulin-MO investigates the radiation conditions in Mars Science Orbit (MSO). MSO is an almost circular orbit with 400 km altitude (varies within ±25 km in every orbital pass), 74^0 inclination, ~ 2 hours orbit period.

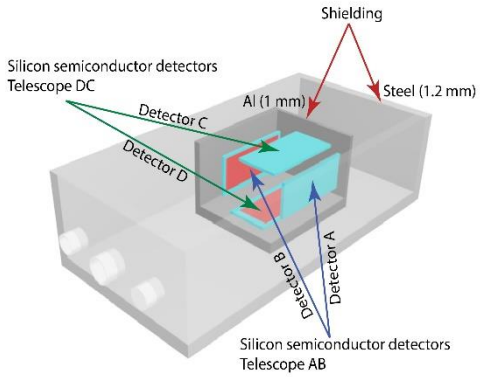

Figure 1. *A schematic view of Liulin-MO detectors' location in the dosimeter box [Semkova et al., 2021]*

The Liulin-MO dosimeter contains two dosimetric telescopes- BA and DC arranged at two perpendicular directions. Figure 1 is a sketch of the sensor unit. Each pair of the dosimetric telescopes consists of two 300 μm thick, 20x10 mm area rectangular Si PIN photodiodes. The parameters, provided by Liulin-MO simultaneously for two perpendicular directions have the following ranges: absorbed dose rate from 10^{-7} Gy h^{-1} to 0.1 Gy h^{-1}; particle flux in the range 0 - 10^4 cm^{-2} s^{-1}; energy deposition spectrum in the range 0.08 - 190 MeV. The dose rates and the fluxes are resolved every minute, while the energy deposition spectra are resolved every hour. The instrument also provides data for the linear energy transfer spectra, radiation quality factors and dose equivalent rates in two perpendicular directions. In this paper we use the data provided by single detectors B(A) and D(C) in the energy deposition range > 0.08 MeV. All events with energy deposition > 190 MeV are registered and are considered as events with 190 MeV energy deposition in the subsequent calculations. Data must be understood in the context of the shielding from the free-space radiation environment provided by the mass of materials surrounding the instrument's detectors. The shielding distribution covers a thickness range from 0.9 to 178 g cm^{-2}. The first momentums of the shielding distribution probability density is about 20 g cm^{-2}. The energy threshold for the minimum shielding is 1.7 MeV for electrons, 30 MeV for protons and 6.8 GeV for iron ions.

3. Liulin-MO data in TGO Mars science orbit and discussion

3.1. Particle fluxes and dose rates from GCR in the period May 2018-June 2022

The fluxes and dose rates recorded in the single perpendicular detectors B(A) and D(C) of Liulin-MO and the proton flux>30 MeV measured by SIS instrument on ACE satellite for the period from May 2018 to June 2022 are shown in Figure 2.

Increase of the dose rates and fluxes from May 2018 to February 2020 which corresponds to the increase of GCR intensity during the declining of the 24^{th} solar cycle is observed. The averaged dose rate for the period is 15 μGy h^{-1}, the averaged particle flux is 3.14 $cm^{-2}s^{-1}$. In March-August 2020 the radiation values are maximal, corresponding to the minimum of the 24^{th} cycle and transition to the 25^{th} cycle. The dose rate is 15.9 μGy h^{-1}, flux is 3.3 cm^{-2} s^{-1}. Dose equivalent rate is 72 μSv h^{-1}. Since September 2020 a decrease of the dose rates and fluxes is seen corresponding to the increasing phase of the 25^{th} solar cycle.

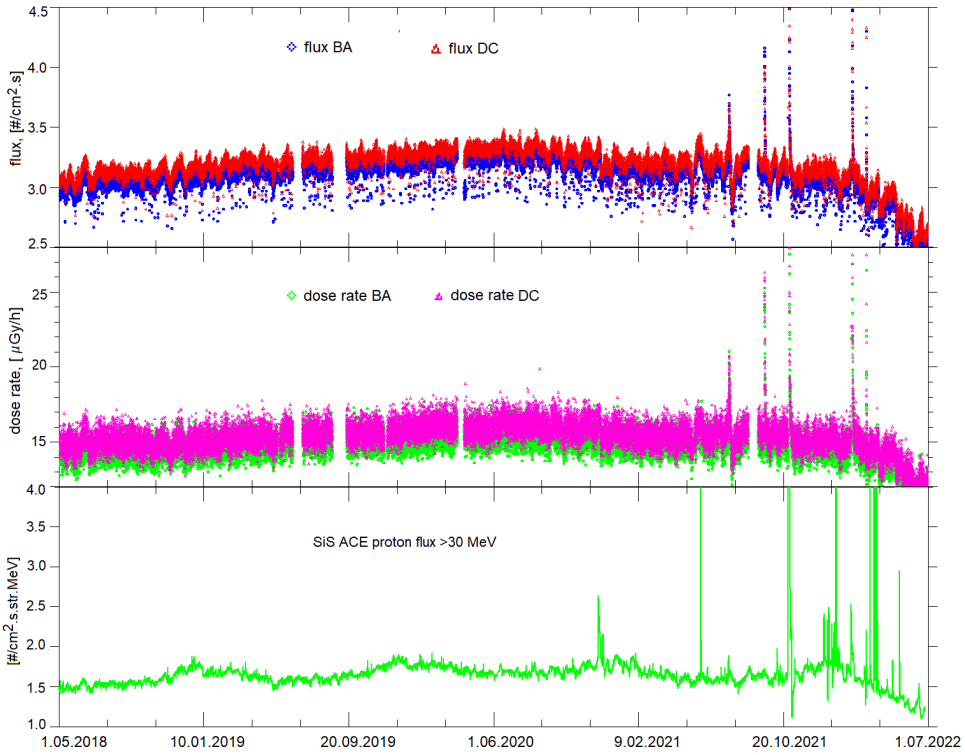

***Figure. 2**. Fluxes (top) and dose rates (middle) measured by Liulin-MO in MSO and SIS-ACE proton flux>30 MeV (bottom) in the period 01 May 2018 – 30 June 2022*

Until July 2021 the dosimeter measured the dosimetric parameters of GCR. No solar particle events (SPE) were registered.

Five SEP events are observed from July 2021 to March 2022. SEP events in October 2021 are observed also on ACE. During all these SEP events Earth and Mars are on opposite sides from Sun.

The data for the parameters of the coronal mass ejections (CMEs) related to the observed on TGO SEP events discussed below are taken from the catalogue SEEDS (http://spaceweather.gmu.edu/seeds/).

• 3.2. SEP event and Forbush decrease of GCR observed on 17-28 July 2021

This event was discussed in more details in Krastev et al, 2021. A CME responsible for the increase of Liulin-MO flux and dose rates could be that observed by LASCO (SOHO) coronagraph C2 at 05:24. The time at which it was ejected from the sun surface is about 04:55 UT. Later CME developed as a halo CME. The speed of the CME was over 1000 km s^{-1}.

On 17.07.2021 at 07: 12 UTC started an increase in the flux and dose rate of Liulin-MO due to SEP. During 20-28.07.2021 a Forbush decrease of GCR is observed. The time profiles of the particle flux and dose rate during the event are shown in Figure 3. For the entire event from 17 to 28.07.2021 a decrease of the dose rate by 0.5 μGy h^{-1} compared to quite conditions before the event is observed.

3.3. SEP event observed on 17-18 September 2021

A high speed CME (over 1000 km s^{-1}) directed to Mars with onset about 04:00 UT was registered by SOHO and STEREO-A on 17th September 2021.

The time profiles of the particle flux and dose rate measured by Liulin-MO during this event are shown in Figure 4.

The total dose from SEP received during 17-18 September 2021 event is 156 μGy which is less than the half of daily dose from GCR.

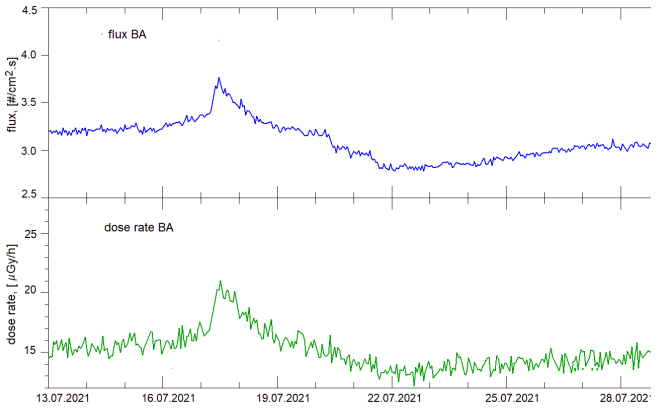

Figure 3. *Time profiles of the particle flux (top) and dose rate (bottom) during SEP event on 17-28 July 2021*

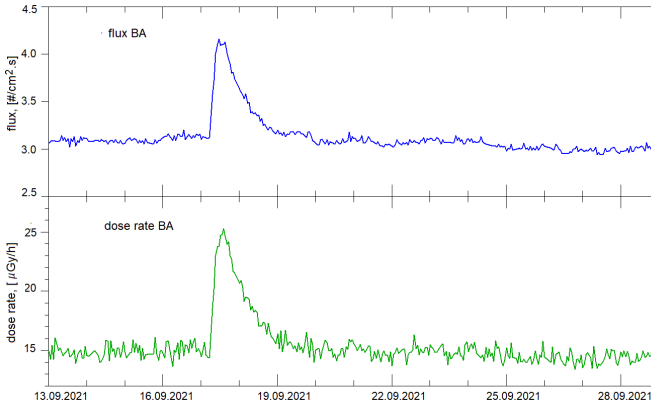

Figure 4. *Time profiles of the particle flux (top) and dose rate (bottom) during SEP event on 17-18 September 2021*

3.4. SEP event observed on 28-31 October 2021

Both LASCO and STEREO A registered the launch of a halo CME on 28 October 2021.

A fast CME originated from the southern hemisphere and caused strong SEP events over a wide longitude range from Earth, STEREO-A, to Mars (Xiaolei Li et al, 2022).

During this event the first ground level enhancement (GLE) of Solar Cycle 25 was observed (Papaioannou et al, 2022).

The time profiles of the particle flux and dose rate measured by Liulin-MO during this event are shown in Figure 5. On 28.10.2021 at 16:55 UT began a large increase in Liulin-MO flux and dose rates which lasted till 31.10.2021.

The total dose from SEP for 28-31 October 2021 event is about 7 mGy, which is equal to the dose received from GCR for 19 days during quite conditions. At the peak of the event the dose rate is about 30 times larger and the flux is about 15 times larger than the corresponding values of GCR. The dose equivalent from SEP during this event is 10 mSv.

3.5. SEP event observed on 15 February 2022

On 15 February 2022 Solar Orbiter has captured the largest solar prominence eruption ever observed in a single image together with the full solar disc according ESA press release. The eruption have originated from the side of the Sun facing away from Earth. The eruption was registered by all coronagraphs at about 22 UTC. The CME propagated in northeast direction, includes the ecliptic. Its speed was about 1000 km s^{-1} and the consequent shock wave accelerated the SEP that could reach Mars.

The time profiles of the particle flux and dose rate measured by Liulin-MO during this event are shown in Figure 6. The increase of the dose rate and flux is observed from 15.02.2022 22:23 UT to 19.02.2022 04:23 UT.

The SEP dose measured by Liulin-MO during this event is 14.2 mGy - equal to the dose for 38.5 days from GCR in quite conditions. At the peak of the event the dose rate is about 2 orders

larger than the dose rate in quite conditions. The dose equivalent from SEP during this event is 27.6 mSv. This is the most powerful event observed in our data.

One can see a short burst, after that a drop and another period of increase in the time profiles of the flux and dose rate. This is sometimes observed when an interplanetary shock wave passes near a spacecraft.

3.6. SEP event observed on 14 March 2022

Liulin-MO flux and dose rates start to increase at 17:55 UTC on 14 March 2022, the increase is modest in comparison with 28 October 2021 and 14 February 2022 events.

3.7 Comparison of measurement of different detectors in Mars orbit during February 2022 SEP event

Compared are the time profiles of the normalized count rates of Liulin-MO, neutron detectors of FREND instrument on ExoMars TGO and the neutron detector HEND aboard Mars Odyssey spacecraft (Mitrofanov et al, 2003) during February 2022 SEP event (Figure 7). A very good agreement between the measurements of the different detectors located on different spacecrafts in Mars orbit during this event is observed.

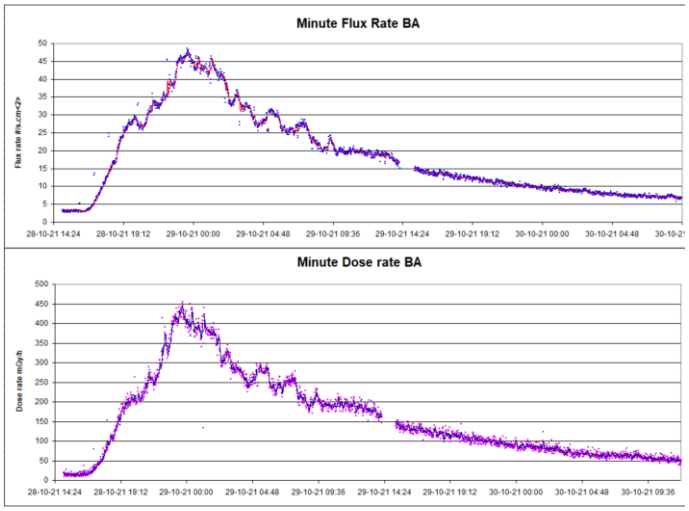

Figure 5. *Time profiles of the particle flux (top) and dose rate (bottom) during SEP event on 28-31 October 2021*

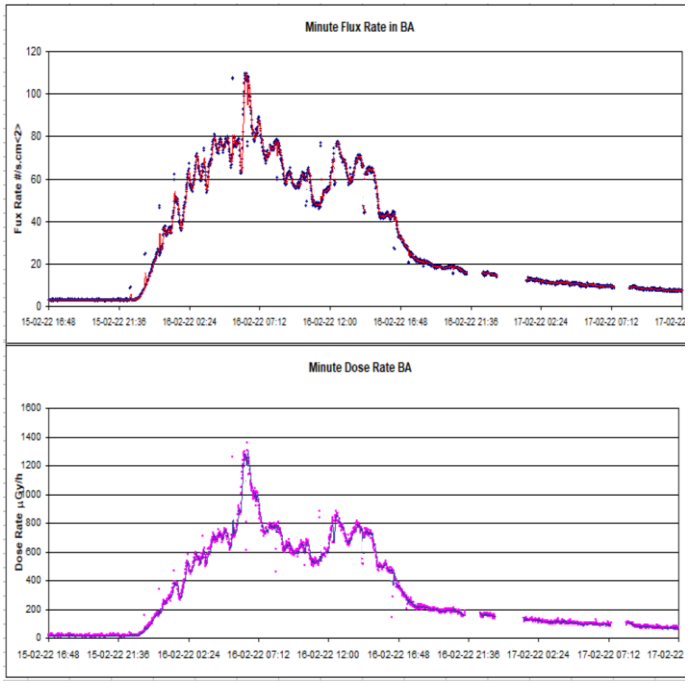

Figure 6. *Time profiles of the particle flux (top) and dose rate (bottom) during SEP event on 15-19 February 2022*

Conclusions

The measurements of the radiation environment on ExoMars TGO Mars science orbit show that: At the minimum of 24th and transition to 25th solar cycle the dose rate from GCR is 15.9 μGy h^{-1}, particle flux is 3.3 cm^{-2} s^{-1}, dose equivalent rate is 72 μSv h^{-1}; The total dose from SEP for 28-31 October 2021 event is about 7 mGy (in Si). The dose equivalent from SEP is 10 mSv; The SEP dose from 15-19 February 2022 SEP event is 14.2 mGy (in Si). The dose equivalent from SEP is 27.6 mSv; The SEP events in July 2021, September 2021 and March

2022 have no significant effect on the radiation environment on TGO; The dosimeter and the neutron detectors on TGO and Mars Odyssey spacecrafts show similar time profiles of SEP count rates.

The data for SEP events on TGO in July 2021 – March 2022 contribute to the details for the solar activity at a time when Mars is on the opposite side of the Sun from Earth.

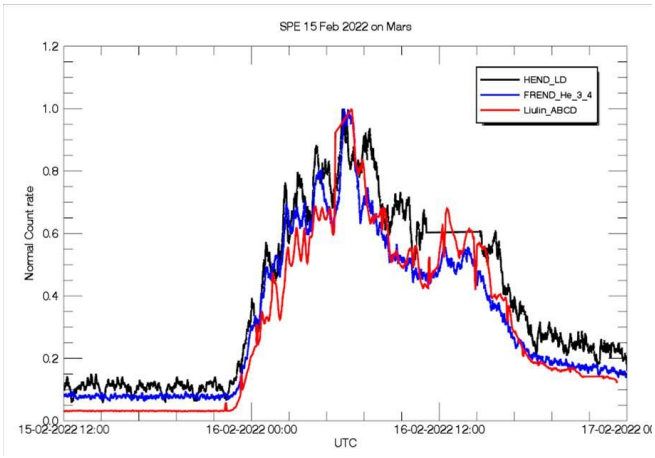

Figure 7. *Time profiles of the normalized count rates of FREND neutron detectors (blue), Liulin-MO (red) and HEND-Mars Odysee (black) during 15-17 February 2022 SPE*

Acknowledgements

The work in Bulgaria is supported by grant KP-06-Russia 24 (Project No. 129 for bilateral projects with Russia) of the National Science Fund of Bulgaria.

References

Badhwar, G. D, O'Neill, P. M., 1992. An improved model of galactic cosmic radiation for space exploration missions. Nucl. Tracks Radiat. Meas., 20, 403–410. DOI: 10.1016/1359-0189(92)90024-P

Guo, J., C. Zeitlin, R. Wimmer-Schweingruber, D. M. Hassler et al. Measurements of the neutral particle spectra on Mars by MSL/RAD from 2015-11-15 to 2016-01-15. Life sciences in space research, 14, 12–17, 2017

Guo, J., Zeitlin, C., Wimmer-Schweingruber, R. F., et al (2021). Radiation environment for future human exploration on the surface of Mars: The current understanding based on MSL/RAD dose measurements. Astronomy and Astrophysics Review, 29(1), 1–81, https://doi.org/10.1007/s00159-021-00136-5

Knutsen, E. W., O. Witasse, B. Sanchez-Cano et al, Galactic cosmic ray modulation at Mars and beyond measured with EDACs on Mars Express and Rosetta, A&A 650, A165 (2021)

Krastev K., et al, Temporal Analysis of the GCR Flux Obtained from the Liulin-MO Instrument in Orbit around Mars, Proceedings of the Thirteenth Workshop "Solar Influences on the Magnetosphere, Ionosphere and Atmosphere" September, 2021, pp.40-45, https://www.spaceclimate.bas.bg/ws-sozopol/pdf/Proceedings2021Final.pdf

Mitrofanov I.G., Litvak M.L., Kozyrev A.S. et al, 2003. Search for water in Martian soil using global neutron mapping by the Russian HEND instrument onboard the US 2001 Mars Odyssey spacecraft, Solar System Research, Volume 37, Issue 5, pp. 366-377

Mitrofanov I., A. Malakhov, B. Bakhtin et al., 2018. Fine Resolution Epithermal Neutron Detector (FREND) onboard the ExoMars Trace Gas Orbiter, Space Science Reviews, August 2018, 214:86, https://doi.org/10.1007/s11214-018-0522-5

Papaioannou, A., A. Kouloumvakos, A. Mishev et al., The first ground-level enhancement of solar cycle 25 on 28 October 2021, A&A 660, L5 (2022), https://doi.org/10.1051/0004-6361/202142855

Semkova J., R. Koleva, V. Benghin et al, Charged particles radiation measurements with Liulin-MO dosimeter of FREND instrument aboard ExoMars Trace Gas Orbiter during the transit and in high elliptic Mars orbit, Icarus, 303, (2018) 53–66, https://doi.org/10.1016/j.icarus.2017.12.034

Semkova J., R., Koleva, V.,Benghin et al, Results from radiation environment measurements aboard ExoMars Trace Gas Orbiter in Mars science orbit in May 2018 - December 2019, Icarus, June 2021, 114264, https://doi.org/10.1016/j.icarus.2020.114264

Xiaolei Li, Yuming Wang, Jingnan Guo et al., Solar Energetic Particles Produced during Two Fast Coronal Mass Ejections, The Astrophysical Journal Letters, 928:L6 (8pp), 2022 March 20, https://doi.org/10.3847/2041-8213/ac5b72

Zeitlin, C., W. Boynton, I. Mitrofanov et al, Mars Odyssey measurements of galactic cosmic rays and solar particles in Mars orbit, 2002–2008, SPACE WEATHER, VOL. 8, S00E06, doi:10.1029/2009SW000563, 2010

Zeitlin, C., D. M. Hassler, F. A. Cucinotta et al, 2013. Measurements of energetic particle radiation in transit to Mars on the Mars Science Laboratory. Science 340, 1080, 2013. DOI: 10.1126/science.1235989.

Solar Influence on Ozone Variations over ENSO Regions

Chapanov Y.[1]

[1]Climate, Atmosphere and Water Research Institute, Bulgarian Academy of Sciences;
yavor.chapanov@gmail.com

Abstract.

The most important source of ENSO (El-Nino Southern Oscillation) excitation is the influence of harmonics of solar activity cycles. The solar activity is reveling mainly by the Total Solar Irradiance (TSI) variations, solar wind and variations of solar magnetic field. While the TSI variations affect directly earth surface temperature, the solar wind and magnetic field modulate changes of the heliosphere, geomagnetic field and cosmic ray variations. The cosmic ray variations drive ozone production in low stratosphere near the tropopause, and next a chain process affects surface temperature. These effects are proved in polar and ENSO regions. In previous studies, a strong correlation has been found between ozone and El Nino variations; and between the variations of indices of N-S solar asymmetry and Nino 3.4. So, the possible transmitter between solar signals and ENSO event is low stratospheric ozone, whose variations are affected by solar activity. The solar influence on ozone variations over ENSO regions is investigated by means of time series of solar activity indices and ozone variations at 70 HPa over Nino 3.4 regions around equatorial part of Pacific Ocean. The common harmonics of solar and ozone cycles are determined by means of recently developed Method of Partial Fourier Approximation, where the trigonometric coefficients are estimated by the Method of Least Squares. The results of common frequency bands with interannual, decadal and centennial periodicity of solar and ozone data may improve models of solar influence on Pacific temperature anomalies and recent climate change.

Keywords: N-S solar asymmetry; ozone; ENSO**.**

Introduction

The solar activity affects all geosystems, including climate and weather. The TSI cycles are the main source of climate indices variations. Recently a new mechanism of climate modulation, based on cosmic rays variations has been proposed (Kilifarska et al., 2005, 2008; Kilifarska 2011; Velinov et al., 2005). This mechanism is based on chain processes near tropopause at 70 hPa geopotential height, approximately 17 km above sea level. The several steps of ozone production, due to cosmic rays are followed by temperature variations, vertical winds and water content change. The last step of this chain affects surface temperature, because the atmospheric water is one of the most powerful greenhouse gas. This model provides an explanation for the cascade processes in which CR, whose total energy is relatively small, cause climatic effects with much more energy. The solar activity cycles modulate CR directly by the heliosphere and indirectly by the geomagnetic field changes, whose effect is visible mainly at high latitudes.

The solar activity affects terrestrial systems by means of direct radiation over Earth surface, solar wind, and the solar magnetic field. The solar wind directly affects Earth magnetic field, ionosphere and atmosphere. The variations of solar magnetic field modulate solar wind and cosmic rays in the frame of the heliosphere. The cosmic rays near Earth are modulated by Earth magnetic field variations, too. The variations of solar magnetic field are presented by the Index of North-South Solar Asymmetry (N-S SA). A strong correlation between variations of N-S solar asymmetry and ENSO has been discovered in (Chapanov, 2021, 2022). The changes of

ENSO phase due to near-tropopause ozone has been discover in (Kilifarska and Velichkova, 2021). According to these results, the possible transmitter between the variations of N-S solar asymmetry and ENSO event is low stratospheric ozone.

Data and Methods

The solar data are presented by the Total Solar Irradiance (TSI) and North-South solar asymmetry variations. The daily reconstruction of TSI data since 1850 is a composite of SATIRE-T reconstruction from (Krivova et al., 2014) for 1850 to 22 August 1974; and SATIRE-S reconstruction from (Yeo et al., 2014) for 23 August 1974 onwards (Fig.1). The 0.1-year values of TSI are calculated by means of robust Danish method (Juhl, 1984; Kegel, 1987; Kubik, 1982). This method allows to detect and isolate outliers and to obtain accurate and reliable solution for the mean values.

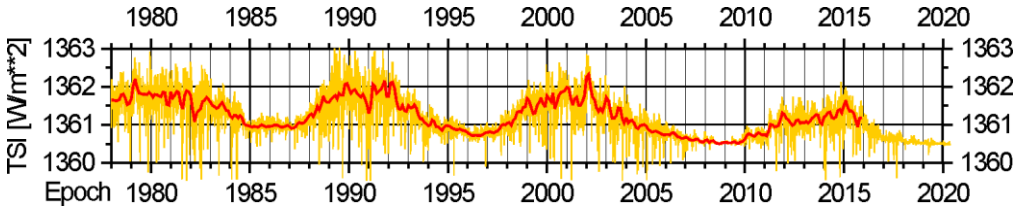

Figure 1. Time series of 0.1-year (in orange color) and daily values (in yellow color) of TSI.

The North-South solar asymmetry (Fig. 2) is determined from the relation $(S_n\text{-}S_s)/(S_n+S_s)$, where the S_n and S_s are monthly sunspot area on the Northern and Southern solar hemispheres, respectively (in units of millionths of a hemisphere). The data since 1874 are observed by the Royal Greenwich Observatory and merged after 1976 with the US Air Force (USAF) and the US National Oceanic and Atmospheric Administration (NOAA) data by D. Hathaway (https://solarscience.msfc.nasa.gov/greenwch.shtml).

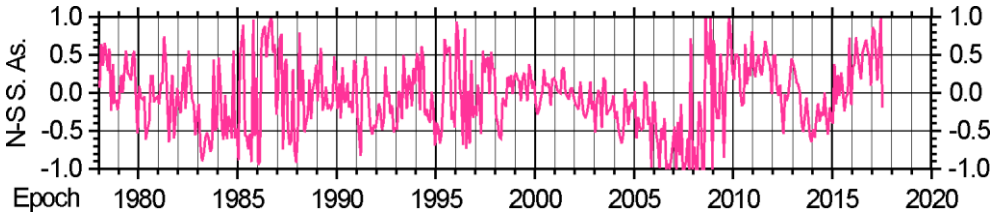

Figure 2. Time series of North-South solar asymmetry.

The ozone and air temperature data are taken from Copernicus servers (Hersbach, 2019) over the region between 5° South - 5° North and 120° - 170° East of ENSO Index Nino 3.4. The time series of ozone and air temperature at 70 hPa over ENSO region are compared in Fig.3. It is remarkable their strong correlation and in phase annual oscillations, which is in full accordance with the Kilifarska's model of ozone influence on climate variations.

The comparison between stratospheric ozone variations and surface temperature at 1000 hPa is shown in Fig.4. It is visible that the maxima of ozone cycles correspond to minima of temperature oscillations. This result corresponds to the Kilifarska's model of ozone influence on climate variations, too.

To prove that the possible transmitter between the variations of N-S solar asymmetry and ENSO event is low stratospheric ozone, the solar and ozone oscillations in narrow frequency bands will be compared. The solar and atmospheric cycles will be retrieved by means of the Method of Partial Fourier Approximation (PFA), whose details are described in (Chapanov et

al., 2017).

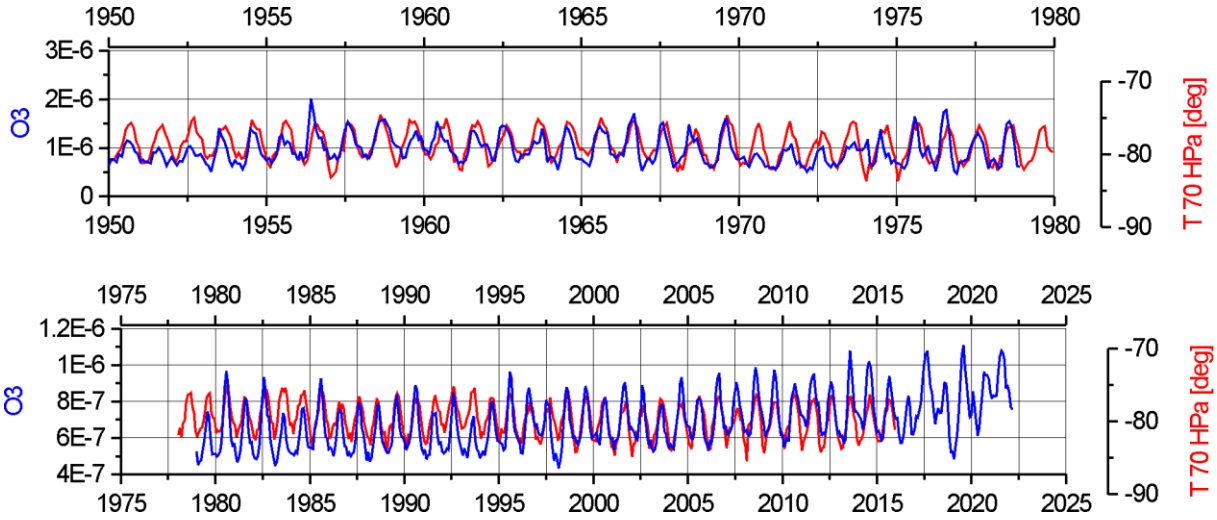

Figure 3. Time series ozone (O3, blue color) and air temperature (red color) at 70 hPa over ENSO region for periods 1950-1979 (upper graph) and 1979-2016.

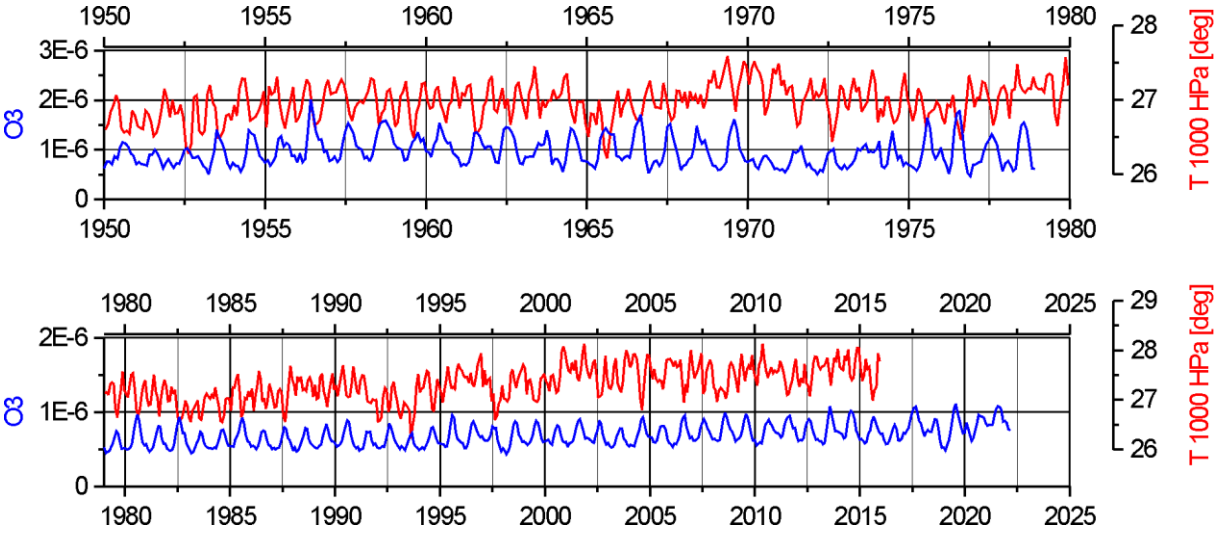

Figure 4. Time series comparison of ozone at 70 hPa and air temperature at 1000 hPa for periods 1950-1979 (upper graph) and 1979-2016.

Results

- ***Time series spectra***

The time series spectra of solar indices and stratospheric ozone (Fig.5) are calculated by Fast Fourier Transform (FFT). The spectrum of N-S solar asymmetry has better coherence with ozone spectrum, then the TSI – ozone spectra, especially for the ENSO frequencies, whose periods are between 2 and 8 years. Other decadal oscillations of N-S solar asymmetry may modulate the amplitude of ENSO variations.

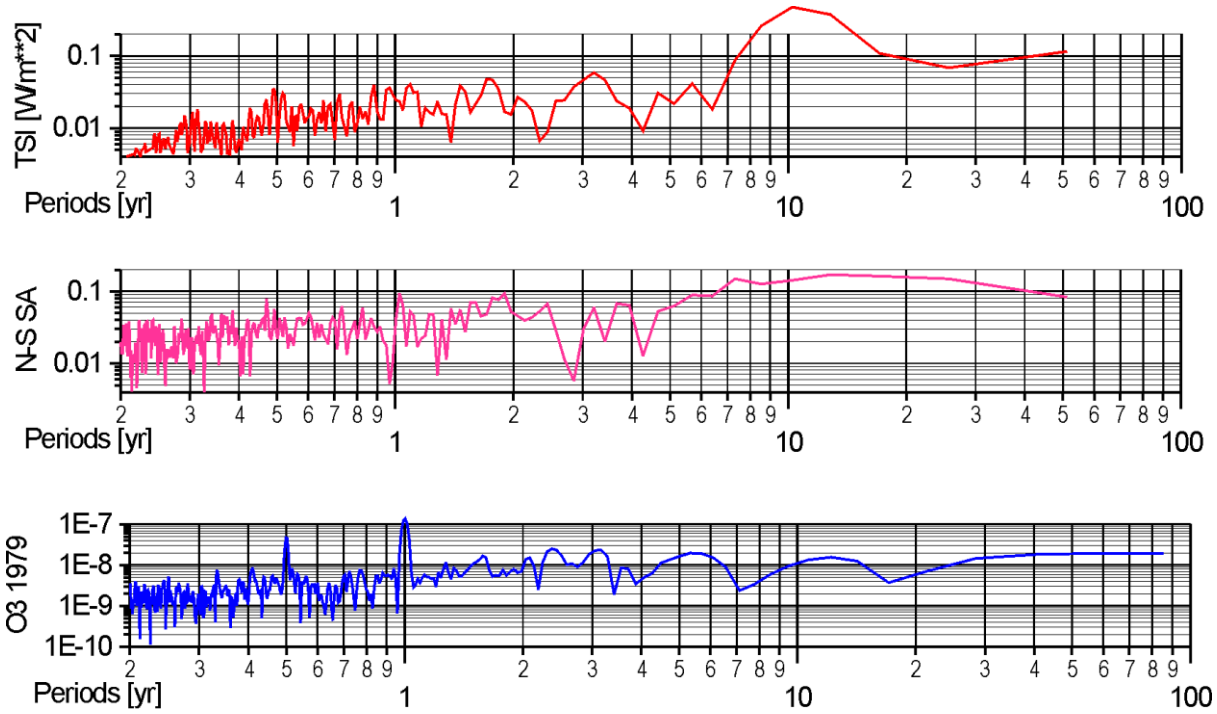

Figure 5. Time series spectra of solar indices and stratospheric ozone variations.

- ***Solar influence on ozone variation at 70 hPa geopotential height***

Common solar and ozone cycles are divided into narrow frequency bands by superposition of neighbor harmonics of their Partial Fourier Approximations. The accuracy of PFA trigonometric coefficients is better than 0.03 for N-S solar asymmetry and better than 3×10^{-9} for ozone data. The influence of N-S solar asymmetry on long-term oscillation of stratospheric ozone is visible in Fig.6, where relatively good agreement exists between solar and ozone cycles in antiphase with periodicity 21.5-43.0 years.

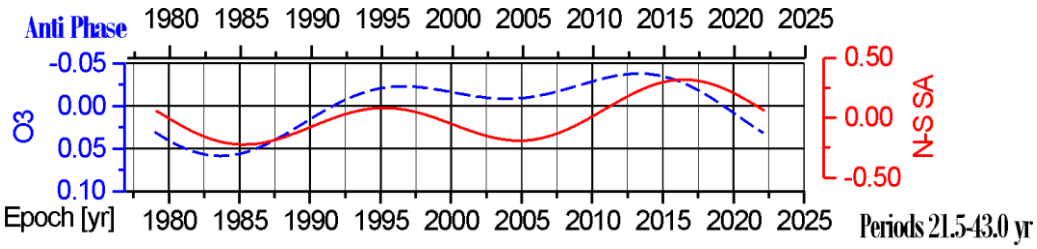

Figure 6. Time series spectra of solar indices and stratospheric ozone variations.

The decadal and short-term influence of N-S solar asymmetry on stratospheric ozone is shown in Figs. 7-9, where common solar-ozone cycles are divided into 9 narrow frequency bands, whose periods are: 2.2-2.4; 2.7-2.9; 3.3-3.6; 3.9-4.3; 4.3-4.8; 4.8-5.4; 6.2-7.2; 7.2-8.6; 10.8-14.4 years. A half of these common bands represent in phase solar and ozone cycles, while the other half represent antiphase cycles. Possible reason of this behavior is different connection of outer and inner radiative belts with the oscillations of solar wind and solar magnetic field. Most of these periods correspond to the essential ENSO frequencies and part of their amplitude modulation.

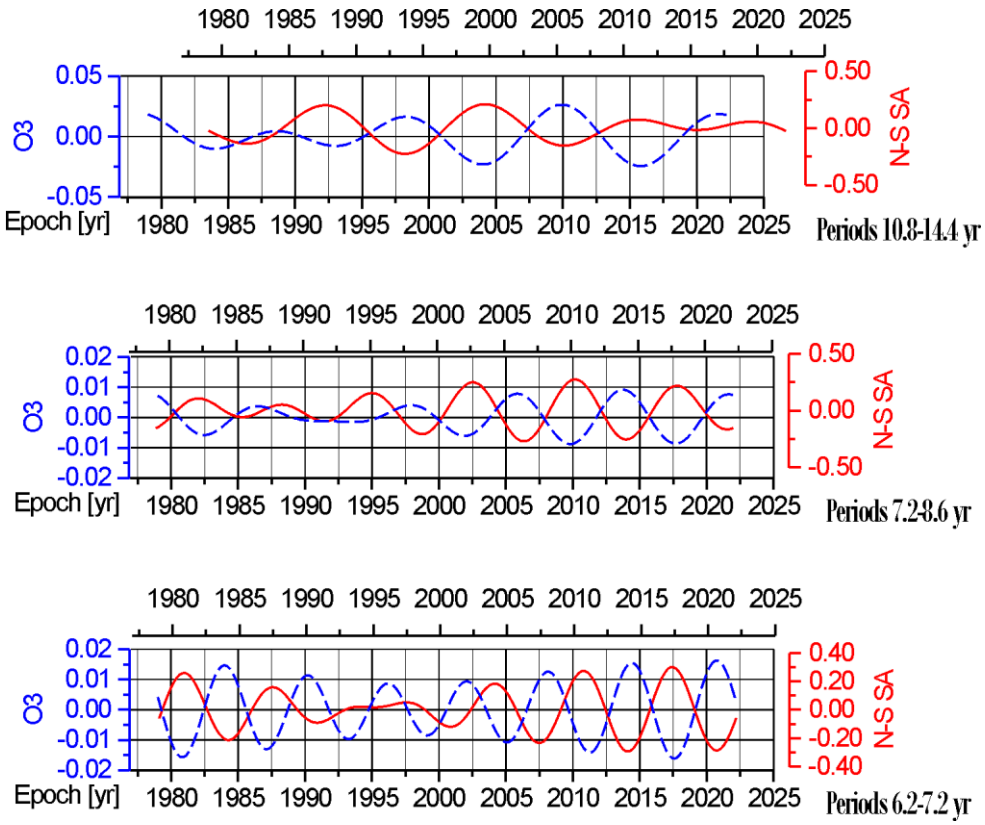

Figure 7. Common solar and ozone cycles with decadal and sub-decadal periods.

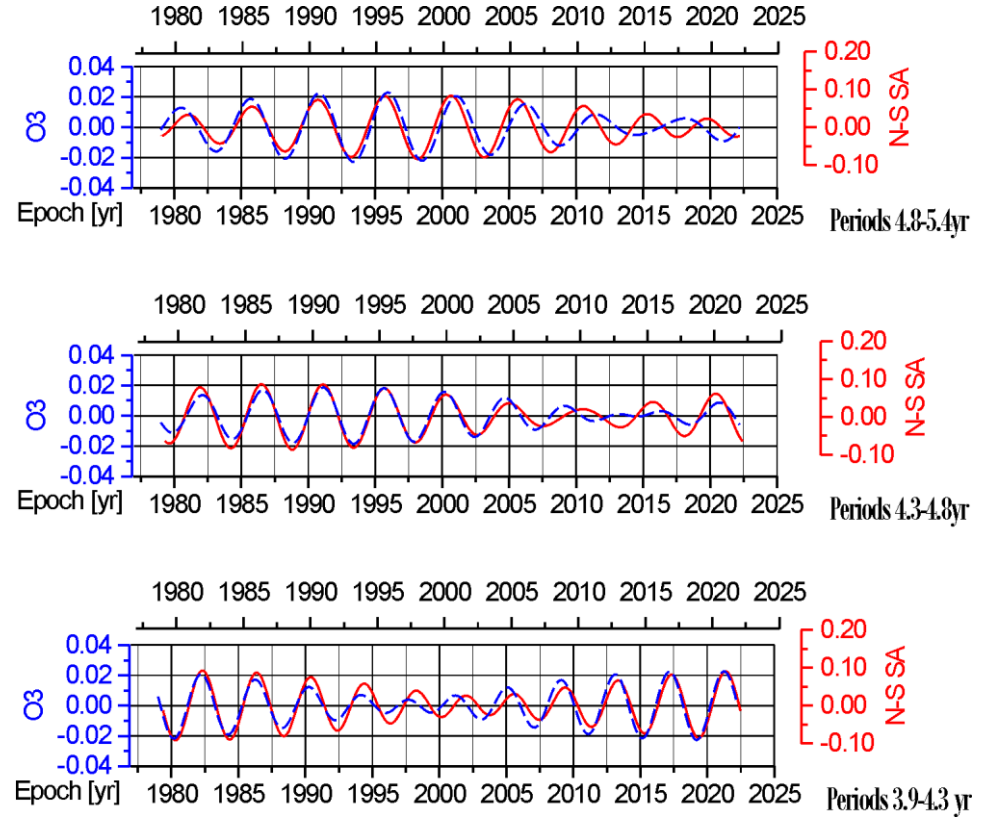

Figure 8. Common solar and ozone cycles with sub-decadal periods between 3.9 and 5.4 years.

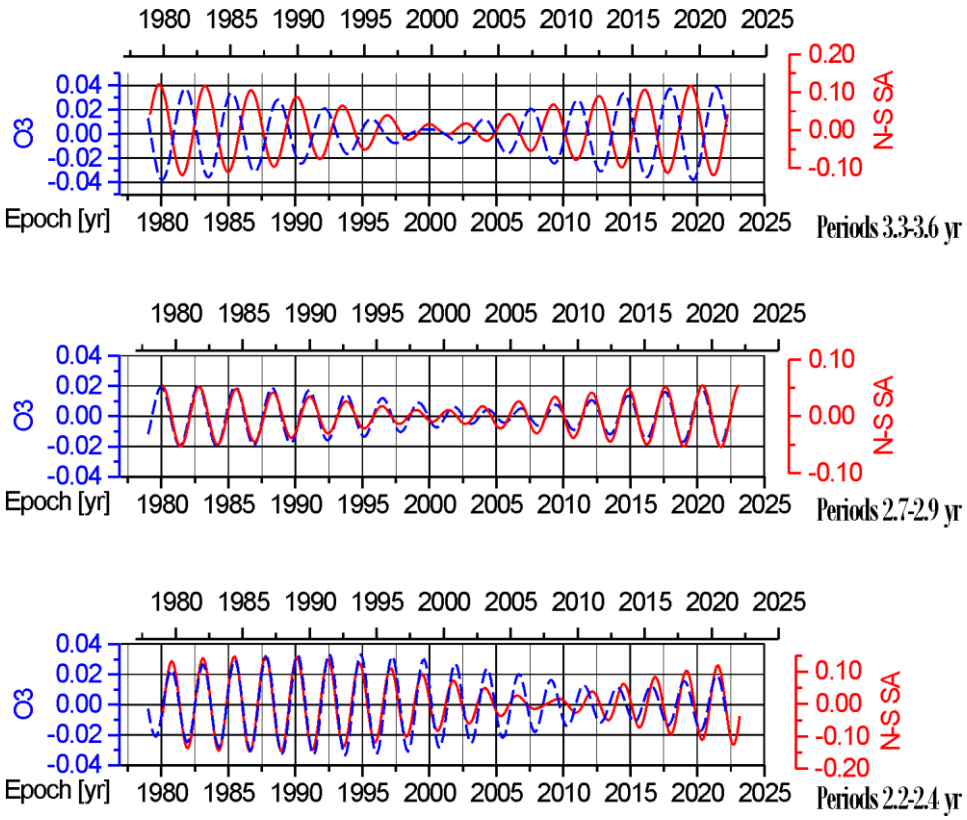

Figure 9. Common solar and ozone cycles with sub-decadal periods between 2.2 and 3.6 years.

Conclusions

The time series of ozone variations at 70 hPa, approximately 17 kilometers above sea level, have been analyzed together with time series of air temperature at 70 hPa and 1000 hPa. The data is calculated over the regions of Enso Index Nino 3.4. The ozone and air temperature have common in phase annual oscillations at 70 hPa height, while some annual oscillations of the surface air temperature at 1000 hPa have antiphase cycles with the annual ozone cycles. These facts confirm Kilifarska's model of stratospheric ozone influence on climate, where the maxima of ozone variations correspond to minima of surface temperature.

The solar magnetic influence on stratospheric ozone variations, over the region of Nino 3.4, is determined in 10 narrow frequency bands, whose periods are in the range of ENSO oscillations between 2 and 8 years, and decadal cycles with periodicity 10.8-14.4 and 21.5-43.0, whose role in ENSO variations is decadal modulation of ENSO amplitude. The last results also confirm the Kilifarska's model of energetic particles influence on ozone and climate variations.

The obtained results may improve our knowledge about important processes in low stratosphere and near tropopause, connected with the climate change.

Acknowledgments

The study is supported by the National Science Fund of Bulgaria, Contract KP-06-N34/1 /30-09-2020 "Natural and anthropogenic factors of climate change – analyzes of global and local periodical components and long-term forecasts"

References

Chapanov Y., Ron C., Vondrák J., 2017, Decadal cycles of Earth rotation, mean sea level and climate, excited by solar activity. Acta Geodyn.Geomater., 14, No. 2 (186), 241–250, DOI: 10.13168/AGG.2017.0007

Chapanov Ya., 2019, ENSO Variations Driven by Solar Cycles, Expressed by N-S Solar Asymmetry, Proc. of Eleventh Workshop "Solar Influences on the Magnetosphere, Ionosphere and Atmosphere, Primorsko, Bulgaria, DOI:10.31401/WS.2019.proc, 152-157.

Chapanov Ya. 2021. Solar Harmonics and ENSO Variations. EAGE, Volume 2021, European Association of Geoscientists & Engineers, 2021, DOI:10.3997/2214-4609.202149BGS42, 1-5.

Farrell, W.M., Desch, M.D. 2002. Solar proton events and the fair weather electric field at ground, Geophys. Res. Lett., Vol 29, No 9, pp. 1323- 1326, DOI: 10.1029/2001GL013908.

Hersbach, H., Bell, B., Berrisford, P., Biavati, G., Horányi, A., Muñoz Sabater, J., Nicolas, J., Peubey, C., Radu, R., Rozum, I., Schepers, D., Simmons, A., Soci, C., Dee, D., Thépaut, J-N. 2019: ERA5 monthly averaged data on pressure levels from 1959 to present. Copernicus Climate Change Service (C3S) Climate Data Store (CDS). (Accessed on 01-Jun-2022), 10.24381/cds.6860a573

Hozworth, R.H. Norville, K.W., Williamson, P.R. 1987. Solar flare perturbations in stratospheric current systems, Geophys. Res. Lett., Vol. 14, No. 8, pp. 52-855.

Juhl, J. 1984. The "Danish Method" of weight reduction for gross error detection. In: XV ISP Congress proc., Comm. III, Rio de Janeiro

Kegel, J. 1987. Zur Lokalizierung grober Datenfehler mit Hilfe ROBUSTER Ausgleichungsfervahren. Vermessungstechnik 35, Berlin, 348-350

Kilifarska, N.A. and Haight, J.D.: 2005, The impact of solar variability on the middle atmosphere in present day and pre-industrial atmospheres. J. Atmos. Solar Terr. Phys., 67, 3, 241-249. DOI: 10.1016/j.jastp.2004.10.003

Kilifarska, N.A., Tassev, Y.K. and Tomova, D.Y.: 2008, Cosmic ray showers and their relation to the stratospheric sudden warmings. Sun and Geosphere, 3, 1, 10-17.

Kilifarska, N.A.: 2011, Long –term variations in the stratospheric winter time ozone variability – 22 year cycle. Comptes rendus de l'Académie bulgare des Sciences, 64, 6, 867-874.

Kilifarska, N. and Velichkova, T., 2021, Near-tropopause Ozone – a Driver of the El Nino Southern Oscillation's Phase Changes, European Association of Geoscientists & Engineers, Conference Proceedings, 11th Congress of the Balkan Geophysical Society, Volume 2021, p.1 – 5, ISSN 2214-4609, DOI: https: -- -- doi.org -- 10.3997 -- 2214-4609.202149BGS37

Krivova N.A., Vieira L.E.A., Solanki S.K. 2010. Reconstruction of solar spectral irradiance since the Maunder minimum. J. Geophys. Res. 115 (A12112), 1-11.

Kubik, K. 1982. An error theory for the Danish method. In: ISP Symposium, Comm. III, Helsinki.

Yeo K.L., Krivova N.A., Solanki S.K., Glassmeier K.H. 2014. Reconstruction of total and spectral solar irradiance from 1974 to 2013 based on KPVT, SoHO/MDI and SDO/HMI observations. Astron. Astrophys. 570 (A85), 1-18

Velinov, P.I.Y., Mateev L. and Kilifarska N.A.: 2005. 3-D model for cosmic ray planetary ionisation in the middle atmosphere. Ann. Geophys., 23, 9, 3043-3046. DOI: 10.5194/angeo-23-3043-2005

Space weather and its effects on spacecraft charging

Kirov B., Georgieva K., Asenovski S.

Space Research and Technology Institute BAS, Sofia, Bulgaria, e-mail: bkirov@space.bas.bg

Abstract.

In the current work we describe the Langmuir Probe (LP) and its operation on board the International Space Station. This instrument is a part of the scientific complex "Ostonovka". The main goal of the complex is to establish, on one hand how such big body as the International Space Station affects the ambient plasma and on the other how Space Weather factors influence the Station. The LP was designed and developed at BAS–SRTI.

Keywords: *Space weather; spacecraft charging*.

1. Studies on spacecraft charging

Studies on the spacecraft charging began after several occasions of anomalous behavior of satellites in the early 1970s, and especially after the loss of the US military satellite DSCS-9431 in 1973 [Bedingfield et al., 1996]. A large program was jointly conducted by NASA and the U.S. Air Force to investigate the problem. The USAF P78-2 Spacecraft Charging at High Altitudes (SCATHA) satellite operating between March 1979 and June 1980 was specially designed to obtain environmental and engineering data to allow the creation of design criteria, materials, techniques, tests and analytical methods to control charging of spacecraft surfaces [Mullen and Gussenhoven, 1983]. Its orbit was close to geostationary (apogee 43 240 km, perigee 27 550 km, inclination 7,9°). The satellite had a mass of 227 kg, diameter of 1.3 m, length of 1.5 m. There were several booms for instruments' sensors. The scientific tasks included the determination of the electric potential at the surface of different materials widely used for spaceborne instrumentation, measurement and analysis of electrostatic disturbances caused by electrical discharges on the surface, study of the degradation of the outer surface of the satellite and evaluation of the surface pollution by the vehicle's own atmosphere. The electron gun with 3 KV maximum accelerating voltage and 6 mA current allowed to induce charging of the satellite with respect to the surrounding plasma, similar to the charging in active experiments. During the operation of the electron gun, electrical discharges were registered and even failures in two of the instruments, coinciding in time with the most intense discharges. This was a direct confirmation of the possibility of instrument failures due to electrical discharges on the satellite's surface. The first year of SCATHA operation showed a high level of elecrtization. For example, in the morning of 24 April 1979, even when the satellite was sunlit, the surface charged up to -340 V. When the satellite was in the shade for a short time on this same day, a surface potential of -8 V was registered.

Later experimental evidence has shown that electric potential differences as severe as -680 volts can develop between Defense Meteorological Satellite Program (DMSP) polar-orbiting (840 kilometers) spacecraft and their high-latitude environment, an analysis was performed using DMSP F6, F7, F8, and F9 satellite precipitating particle and ambient plasma measurements taken during the winters of 1986-87 (solar minimum) and 1989-90 (solar maximum) to explore space vehicle charging in this region. Solar cycle dependence was found with charging occurring more frequently and with greater severity during the period of solar minimum [Frooninckx, 1991]. The joint Air Force/NASA Combined Release and Radiation Effects Spacecraft (CRRES) which was launched in July 1990 into a geosynchronous transfer orbit further investigated the effects on microelectronic elements of space radiation.

Data for the time distribution of anomalies and failures of the payload of geostationary satellites, as well as results of direct measurements of the satellite surface potential show that disturbances in the instrument operation due to charging to high negative potentials occur mainly at nighttime and in the morning hours. Moreover, a correlation is found with the level of geomagnetic activity.

2. Space weather and its effects on spacecraft charging

What mainly determines the spacecraft charging and therefore the safe operation of the electronic devices in space is the space weather. "Space weather" is usually understood as the conditions and processes occurring in space which have the potential to affect the near Earth environment. Space weather processes can include changes in the interplanetary magnetic field, interplanetary plasma parameters like plasma speed, density and temperature, and disturbances in the Earth's magnetic field. All these changes have their origin in processes occurring on the Sun. Space weather is very similar in context to atmospheric weather. Atmospheric weather is a set of phenomena occurring in the terrestrial atmosphere. Space weather is the set of phenomena occurring in the solar atmosphere. The Earth, together with the whole Solar system, is inside the atmosphere of the Sun. Sun is a variable star, and the varying solar radiation, magnetic fields and charged particles interact with the Earth and result in variations in geomagnetic activity, weather and climate, telecommunications, space flight and air flight security, power supply stability, down to seismic activity and human physiological state. The best known manifestation of solar variability is the ~11-year cycle of the number of sunspots (Fig.1). Actually, sunspots themselves are not "geoeffective" – they have no effect on the Earth, but they are the manifestation of the evolution of the solar magnetic field. Related to this magnetic field are solar total and spectral irradiance which vary in the 11-year solar cycle together with the number of sunspots (Fig.2).

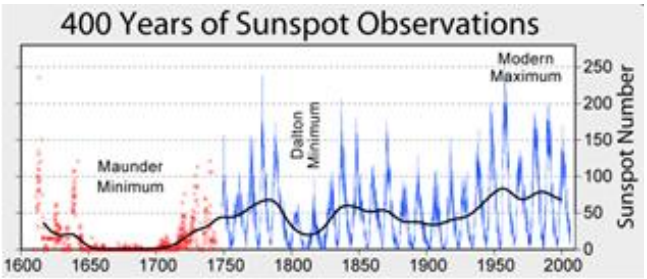

Figure 1. *Yearly number of sunspots showing a ~11-year cycle superposed on longer-term secular variability. A figure borrowed from Wikipedia.*

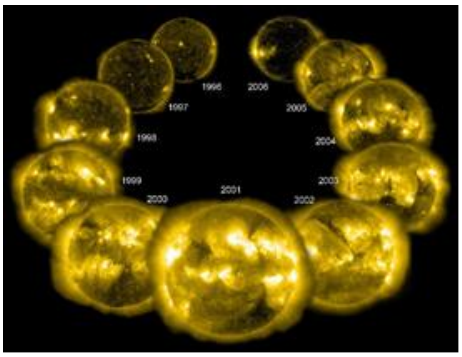

Figure 2. *An image in the 284 Angstrom wavelength of extreme UV light from each year of nearly an entire 11-year solar cycle. Courtesy: EIT instrument, Solar and Heliospheric Observatory (SOHO) http://sohowww. nascom.nasa.gov/.*

Also related to sunspots are the Coronal Mass Ejections (CMEs) – powerful explosions sending into space huge bubbles of gas threaded with magnetic field (Fig.3). The number and intensity of CMEs are greatest during periods with maximum number of sunspots.

Apart from this sunspot-related solar activity, another manifestation of solar activity are high speed streams of charged particles (the so called solar wind) emanating from solar coronal holes - areas of open magnetic field lines where the Sun's corona is colder, and has lower-density plasma than average, so they look darker in X-ray images (Fig.4). The number and intensity of high speed solar wind streams are greatest on the declining phase of the sunspot cycle.

Variations in total and spectral solar radiation are important for the chemistry and dynamics of various atmospheric regions, and are related to climate change. Coronal mass ejections and high speed solar wind streams both lead to geomagnetic disturbances which may disrupt telecommunications and power supply and damage space-borne and air-borne instrumentation. But their effects are not the same. CMEs cause the strongest geomagnetic storms during all phases of the sunspot cycle, but they are relatively rare and short-lasting.

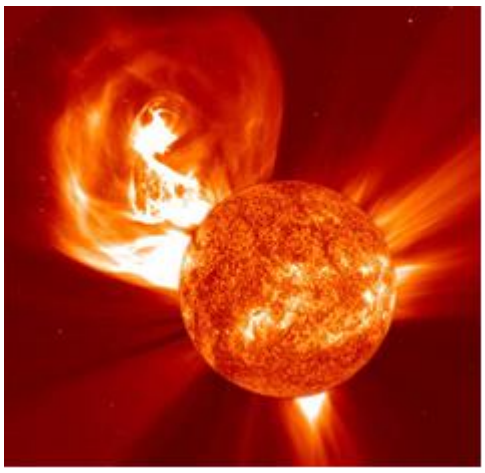

Figure 3. *An EIT image of the Sun in extreme UV light, taken on January 4, 2002, enlarged and superimposed on LASCO C2 coronagraph image. Courtesy: EIT and LASCO C2 instruments, Solar and Heliospheric Observatory (SOHO) http://sohowww.nascom.nasa.gov/.*

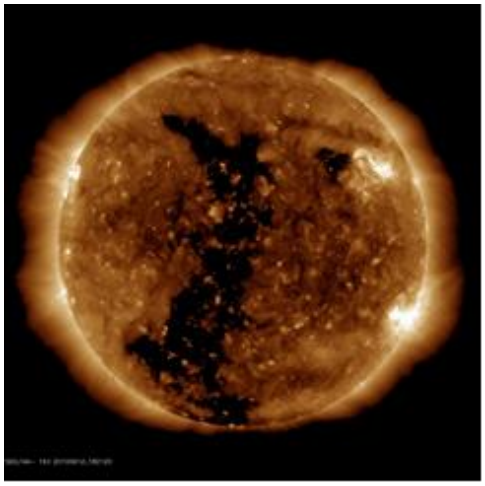

Figure 4. *An X-rat image of the Sun showing a big solar coronal hole (the dark ares). Credit: SDO/AIA.*

Storms caused by high speed solar wind streams are as a rule weaker but longer lasting, and because they are related to long-lived solar structures (coronal holes), they are recurrent – reoccurring every about 27 days, the period of solar rotation, when their parent coronal holes rotate to face the Earth. The spacecraft charging that occurs during storms driven by high speed solar wind streams is evaluated to be more severe than it is for CME-driven storms: the voltages attained are higher, the region of local time over which the severe charging occurs is wider, and the high voltages persist longer (days) [Borovsky and Denton, 2006]. This conclusion, however,

is made on the basis of a limited number of events: 78 CMEs and 32 high speed solar wind streams.

3. Spacecraft effects on plasma

Not only surrounding plasma affects a body immersed into it. The body also disturbs the plasma, creating a sheath – a region surrounding the body - with a thickness proportional to the Debye length $\lambda_D = (\varepsilon_0 K T_e / e^2 n)^{1/2}$ where (ε_0 is the permittivity of free space, K the Boltzmann's constant, T_e, e and n the electron temperature, charge and density, in which the plasma is perturbed by the presence of the body. Besides, a moving body the piles plasma in front of it creating a wake with depleted plasma. Of particular interest is the case when the body's velocity is intermediate between the electron and ion thermal velocities, characteristic for the low orbiting vehicles like manned spacecraft. This has been first confirmed by an experiment aboard AE-C satellite.

All earlier studies have been conducted for relatively small and homogenous spacecraft, while with the launch and gradual build-up of the International Space Station we face the problems of the interaction of a super-large structure at a low orbit with its environment. For the first time we have a structure which is not only that large but also so much energy consuming and emitting. The surface floating potential reaches tens of volts which causes serious problems: On the one hand, the interpretation of the results from the scientific instruments measuring plasma parameters, electric and magnetic fields, becomes practically impossible. On the other hand, the most dangerous effect of the spacecraft charging is the electrostatic discharge during which very strong currents may flow in a short time. As many instruments measure currents of the order 10^{-7} – 10^{-11} A, a much stronger current will lead to the breakdown of the device's input. Of course, each device is protected against such overload, but the problem is the time reaction of the protection circuit. Such current impulses can create false signals in the logical schemes and to lead to the failure of the instrument. For example, twice during the docking of the Shuttle to the ISS, a whole group of computers failed. The possible explanation is a current impulse as a result of the different potentials of the Shuttle and the ISS. Several times there were difficulties during the undocking of the Soyuz spacecraft from the ISS, and one of the hypotheses is the electrostatic charging. To mitigate these problems, a special device - Plasma Contactor Unit (PCU) - has been constructed by NASA to keep the potential under 40 volts. While the PCU limits the space station potential, it neither measures the space station's floating potential, nor characterizes the plasma environment. A Floating Potential Probe is designed for the American module of ISS to monitor the station structure's electrical potential with respect to its local plasma environment and assess the effectiveness of the PCU, and to measure the local plasma parameters. However, the station is a very complex construction which moreover is not fully metalized, so both the surface charging and the ambient disturbed plasma parameters are different in different points, and their special distribution is not known.

Nevertheless, it is important to acknowledge that the inherent nonlinearity [Damgov and Trenchev, 2001; Damgov and Trenchev, 2003; Damgov and Trenchev, 2004] resulting from diverse factors and uncertainties adds a layer of complexity to most processes, challenging our ability to accurately model and comprehend their behaviors using conventional linear frameworks.

4. "Obstanovka" experiment onboard ISS

The goal of the Plasma Wave Complex (PWC) ("Obstanovka" experiment) for wave and plasma parameters measurements in the ISS environment planned onboard the Russian segment of ISS, is to monitor the surface charging and the noises and disturbances in the surrounding plasma induced by the station and by the experiments conducted on it [Klimov and Korepanov,

2004]. PWC is composed of multiple units, which are integrated into two measuring blocks with nearly identical sensors installed outside ISS and the third one inside ISS:

- two combined wave sensors
- two flux gate magnetometers
- two Langmuir probes
- two spacecraft potential monitors
- a plasma discharge stimulator
- a correlating electron spectrograph (10eV – 10KeV)
- a radio frequency analyzer
- a signal analyzer and sampler
- two data acquisition and control units
- a block of storage of telemetry information
- grounding support equipment

During the first stage of the experiment (“Obstanovka-1”), a database of electromagnetic fields and of plasma-wave processes occurring in the ISS near-surface zone will be compiled to account for the influences of the plasma component factors of near-Earth space, including influence of artificial origin. The results will be used in the field of applied geophysics, ecology, space weather monitoring, and also for the updating of operational requirements used in space engineering and technology.

5. Deriving the spacecraft charging with a Langmuir probe

The Langmuir probe is one of the classical instruments for plasma diagnostics [Mott-Smith and Langmuir, 1926] and among the first space-borne instruments. Langmuir probes have been successfully used aboard a number of rockets and satellites for in situ measurements of thermal plasma parameters in the terrestrial ionosphere [Brace, 1998], at other planets [Krehbiel et al. 1980] and comets [Grard et al., 1998].

In principle, a Langmuir probe can be any conducting body introduced into the plasma. Voltage is applied to the probe, changing over a certain range, and the probe current is measured. The dependence of the probe current on the voltage is usually referred to as "probe characteristic" or "volt-ampere curve" (Fig.5). The plasma parameters are derived from the form and amplitude of this volt-ampere curve. When the probe potential is negative enough to repel all the electrons (region A in Fig.5), the probe current is due only to the ions which are accelerated towards the probe, and the current's amplitude is proportional to the ion concentration. When the probe potential is less negative (region B in Fig.5), the more energetic electrons overcome it, and produce an electron current, exponentially increasing when the voltage is further decreased. The net current is a sum of the ion and electron currents, and when the ion current is extracted based on extrapolation of region A, the electron temperature is derived from the slope of the volt-ampere curve in this electron retardation region. When the probe is positive with respect to the plasma, the ion current is negligible while the electrons are accelerated, and the amplitude of the current is a function of the electrons concentration.

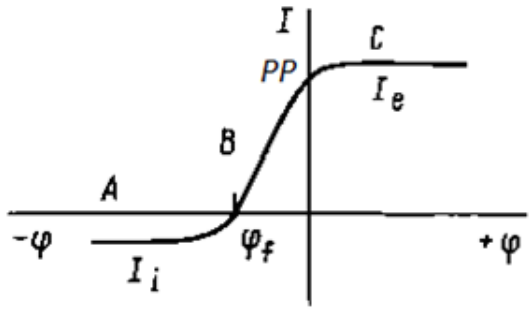

Figure 5. *A typical volt-ampere characteristic from the cylindrical Langmuir probe.*

The point marked PP in Fig.5 is an inflection point in the volt-ampere curve. It corresponds to the plasma potential with respect to the spacecraft, or the spacecraft potential with respect to the plasma. The determination of this potential is equivalent to measuring the electrization of the spacecraft, which is actually our goal.

But the detection of PP, at least as an initial task, is quite difficult. For this reason, instead of the detection of the structure's potential with respect to the plasma, as an initial task the instrument's algorithm is aimed at the detection of the floating potential φ_f - the potential at which the currents due to positively and negatively charged particles to the structure are equal, so the net current is zero. Practically, we apply a sweep voltage to the probe and determine, with accuracy better than 3 mV, φ_f - the voltage at which the current changes sign from positive to negative. For the expected temperature range at the altitudes where the International Space Station operates, the difference between the floating potential φ_f and the station's potential with respect to the plasma PP does not exceed 1.5 V. Further, we apply to the probe a sweep voltage in the range φ_f -$U1$ to φ_f +$U2$, with $U1$ and $U2$ being functions of the slope of the probe characteristic dI/dU in the electron retardation region - that is, in the voltage range between φ_f and PP where the current I is an exponential function of the applied voltage U. At low plasma temperatures the voltage difference between φ_f and PP is too small, and if the data points are uniformly distributed in the measured range, very few points will be derived in the electron retardation region, and the electron temperature will not be correctly determined. To be sure we will have enough data points in the electron retardation region so that we could correctly derive the electron temperature, we divide each of the ranges from φ_f -PP to φ_f (the ion acceleration region), from φ_f to $U2$ (the electron retardation region), and from $U2$ to $U2$+$U3$ (the electron acceleration region) into 20 equidistant points, and measure the probe current in each of these voltage values.

The foreseen modes of operation and the adaptive sweep voltage algorithm may not be enough to account for all different situations that can occur due to the station's charging and the disturbances introduced by the structure itself and by the operation of the numerous systems and instruments into the plasma in the near-surface zone of the station. For this reason, a possibility is foreseen for remote upgrading of the mode of operation of the Langmuir probe, which can be used for remote upgrading of any space-borne instrument in order to maintain the scientific experiments in real time. The communication between the station and the Earth is realized through the telemetry information channels based on radio-frequency connection. Apart from scientific data from the instruments, these channels will be also used for transmitting of commands from the Earth (about the instruments' modes of operation), as well as information blocks (containing object code) for changing the processing and control programs. It allows combining several functions:

- deriving data (in real time) for the observed physical parameters and saving the measured parameters to the onboard computer;

- maintaining an information channel between the ground-based stations and the onboard computer;
- providing access to the derived information and adjusting the specialized software of the orbital scientific instruments using a virtual network (in Internet).

Each scientific program is realised as a state machine and is controlled in real time by its state variables and by the values of the measured parameters.

5. Effect of shading

The ion concentration Ni measured by LP1 on 23.04.2013 does not exceed 4.1010 m-3 (Fig. 6) while the concentration obtained by ground-based data and measured by NLP instrument [Barjatya et al., 2009] at the same time is around 1.1012 m^{-3}.

The difference is due to the fact that NLP is located in the front part of the station and all measurements are performed in undisturbed plasma. On the other hand, LP1 is located on "Zvezda" module in the backside of the station, and just in front of LP1 along the velocity vector is the MLM module, which actually leads to a significant decrease of the plasma density in the vicinity of LP1. Such a decrease of the plasma density in the shadow of a space vehicle was shown in 1965 [Brace et al., 1965].

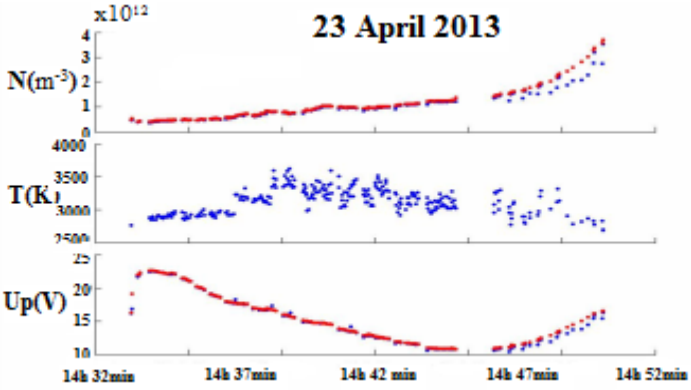

Figure 6. *Ion concentration Ni – upper panel, electron temperature Te – middle panel, and flowing potential Up – bottom panel measured on 23 April 2013 by LP1.*

6. Effect of eclipse exit

When the ISS crosses the eclipse, the observations show a jump of the floating potential. In the case shown in Fig. 3 the potential Up(V) (third panel in Fig. 7) suddenly changed from 10 to 25V (i.e. the floating potential of the station became -25V). According to our American colleges [Mott-Smith and Langmuir, 1926] such a jump is caused by "charging due to additional electron collection on the exposed edges of solar cells".

7. Effect of the Equator crossing

Over the Equator area there are regions with high plasma concentration. One example is shown in Fig. 8. Here the station crosses the Equator at 14:25. The station enters a region of high concentration (upper panel in Fig. 8) which leads to a sharp drop in the flowing potential.

7. Variation of the Flowing potential during a geomagnetic storm

On 23.04.2013, a high speed solar wind stream (HSS) reaches the Earth and causes a geomagnetic storm. Kp starts to increase in the early hours of 23.04.2013 (Fig. 9), while Dst increases a couple of hours later. At the same time the flowing potential jumps from -10 to -15V (Fig. 10). Dst drops around 21:00 UT.

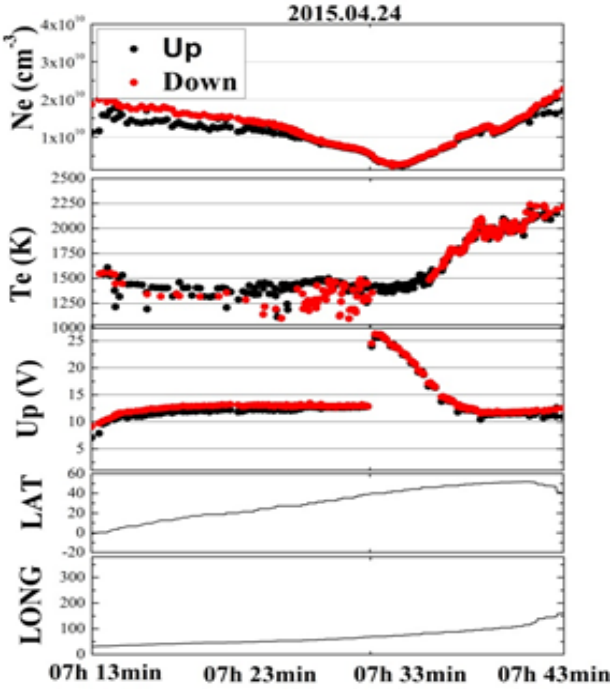

***Figure 7**. Ne (cm^{-3}) – upper panel; Te (K) second panel; Up (V) – third panel; orbital parameters – bottom two panels.*

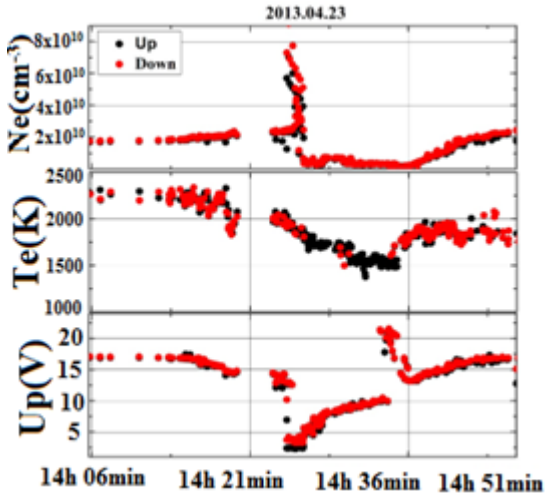

***Figure 8.** Plasma concentration (upper panel), electron temperature (middle panel), and flowing potential (bottom panel) during the Equator crossing.*

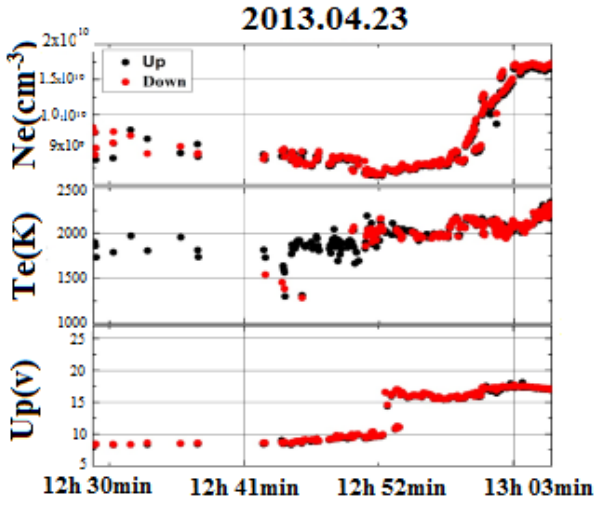

***Figure 9**. Variations of the plasma parameters and spacecraft potential around noon UT on 23.04.2013: Ne (upper panel), Te (middle panel), Up (bottom panel).*

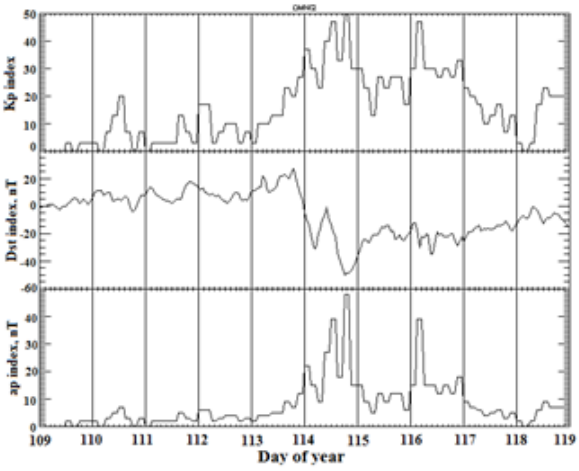

***Figure 10**. The geomagnetic storm on 23.04.2013: Kp-index (upper panel), Dst-index (middle panel), Ap-index (bottom panel).*

Conclusions

Because of the big size of the International Space Station and its complex shape, the plasma density in its vicinity can differ by as much as two orders of magnitude.

In spite of the differences in the plasma density in different locations, their variations are similar.

The spacecraft potential is always negative with respect to the plasma and varies between 0 and -25 V.

The spacecraft potential can change sharply during passages of the eclipse and the equatorial anomaly, and at the beginning of geomagnetic storms.

Acknowledgements

This study is supported by the National Science Fund of Bulgaria, Contract KP-06-N44/2 /27-11-2020 “**Space weather over a period of the century solar activity descending**”.

References

Barjatya, A., Swenson, C.M., Thompson, D.C., Wright, K.H. (2009). Data analysis of the Floating Potential Measurement Unit aboard the International Space Station, REVIEW OF SCIENTIFIC INSTRUMENTS 80, 041301, 80, 041301 (1-11).

Bedingfield, K.L., Leach, R.D. Alexander, M.B. (1996) Editors, “Spacecraft System Failures and Anomalies Attributed to the Natural Space Environment”, NASA Reference Publication 1390, 1996, Marshall Space Flight Center MSFC, Alabama 35812.

Borovsky, J.E., Denton, M.H. (2006). Differences between CME-driven storms and CIR-driven storms, J. Geophys. Res. 111, A07S08, doi:10.1029/2005JA011447.

Brace, L.H. (1998). Langmuir Probe Measurements in the Ionosphere. In: Pfaff, R.F., Borovsky, J.E., Young, D.T. (Eds.), Measurement Techniques in Space Plasmas -- Particles: Geophysical Monograph 102. AGU, Washington, DC USA, pp. 23-35.

Brace, L.H., Spencer, N.W., Dalgarno, A. (1965). Detailed Behavior of the Midlatitude Ionosphere from the Explorer XVII Satellite, Planet. Space Sci., vol 13 pp 647-666.

Damgov, V., Trenchev, P. Phenomenon of “Quantized” Oscillation Excitation. In: Abdullaev, F., Bang, O., Sørensen, M.P. (eds) Nonlinearity and Disorder: Theory and Applications. NATO Science Series, Springer, Dordrecht, 2001, v.45, pp. 397-409, ISBN: 978-1-4020-0192-5, DOI:doi.org/10.1007/978-94-010-0542-5_33.

Damgov, V., Trenchev, P. Class of kick-excited self-adaptive dynamical systems: Quantized oscillation excitations. Chaos, Solitons and Fractals, 2003, 17, 1, pp. 11-40, ISSN: 0960-0779, DOI: https://doi.org/10.1016/S0960-0779(02)00445-9.

Damgov, V., Trenchev, P., Sheiretsky, K. "Oscillator-wave" model: properties and heuristic instances. Chaos, Solitons and Fractals, 2003, 17, 1, pp. 41-60 ISSN: 0960-0779, DOI: https://doi.org/10.1016/S0960-0779(02)00446-0, 41-60.

Frooninckx, T.B. (1991). High-Latitude Spacecraft Charging in Low-Earth Polar Orbit, Master's thesis, Utah University.

Grard, R., Laakso, H., Pedersen, A., Trotignon, J.G., Mikhailov, Y. (1998). Observations of the plasma environment of Particles: Geophysical Monograph 102. AGU, Washington, DC USA, pp. 23-35.

Klimov, S.I., Korepanov, V.Ye. (2004). The "Obstanovka" experiment aboard the International Space Station. Kosmichna Nauka i Tekhnologiya 10 (2/3), 81-86, (In Russian).

Krehbiel, J.P., Brace, L.H. Theis, R.F. et al. (1980). Pioneer Venus Orbiter Electron Temperature Probe. J. Geophys. Res. GE-18, 49-54.

Mott-Smith, L.R., Langmuir, I. (1926). The theory of collectors in gaseous discharges. Phys. Rev. 28 (4), 727–763.

Mullen, E.G., Gussenhoven, M.S. (1983). “SCATHA (Spacecraft Charging at High Altitudes) Environmental Atlas”, Final scientific rept. Force Geophysics Lab Hanscom AFB MA Report Number: A654131.

Peculiar Atmospheric Electric Field Response at High Latitude to Three Major SEP Events in 2001 and Possible Interpretation

Tonev P.T.

Space Research and Technology Institute BAS, Sofia, Bulgaria, e-mail: ptonev@bas.bg

Abstract.

The results are analyzed here from measurements of the atmospheric electric field (AEF) E_z at ground level which had been obtained at high-latitude observatory in Apatity (geomagnetic latitude 63.8°) during three major solar proton events (SPE) with GLE in 2001 (on 15.04, 18.04, and 04.11, respectively). We find strong AEF peculiarities and propose a hypothetical interpretation for them. For each of the SPE E_z demonstrates specific extremely large and unusual variations in two separate time periods: a) during SPE; and b) before the SPE and its causative solar flare. The AEF behaviour cannot be explained by classical theory for the global atmospheric electrical circuit. To interpret the peculiarities we propose hypothetically that the energetic proton flux into atmosphere at polar and high latitudes leads to creation and enlargement of aerosol layers and dramatic decrease of conductivity which causes re-balance in the global electric circuit and to the observed peculiar modifications of E_z at ground level at high latitudes. E_z peculiarities before SPEs can be explained in similar way.

Keywords: *Aerosol creation; conductivity modification; uncompensated electric charge*.

1. Introduction

Our goal in this paper is to consider and hypothetically interpret the effects during three major solar proton events (SPEs) in 2001 accompanied by ground level enhancement (GLE) on the vertical atmospheric electrical field (AEF) E_z at ground level at high latitudes, derived from experimental measurements in Apatity, Russia (geomagnetic latitude Λ=63.8°) [Shumilov et al. (2015)]. The experimental results for AEF E_z have been obtained for SPEs on 15 April (case 1), 18 April (case 2), and 4 November (case 3), respectively. Variations of the electric field E_z demonstrate peculiarities of several types which occur during SPE, but also can are found long before SPE. The experimental data [Shumilov et al. (2015)] are analyzed. Peculiarities during and before SPE are classified in Sections 2 and 4, respectively. Hypothetical interpretations for these two time periods are proposed in Sections 3 and 4.

2. Analysis of experimental data [Shumilov et al. (2015)] during SPE

The results of [Shumilov et al. (2015)] are presented in Figure 1 for each case 1–3. The uppermost panel presents the E_z variations during the entire day of the SPE. The middle panel is for X-ray variations according to GOES-10 data in ranges 0.1–0.8 nm and 0.05–0.4 nm (curves 1 and 2). The lower panel shows the integral fluxes, derived from GOES-10 data, of: *i*) E>2 MeV electrons (curve 1); *ii*) protons with energies E>1 MeV, >10 MeV and >100 MeV (curves 2-4, respectively). Surprising peculiarities in variations of AEF E_z take place which comprise two separate time periods:

- Time period (***A***) when the energetic proton flux is sufficiently high. It is characterized by strong deviations of AEF E_z from its usual behavior, as response to SPE.
- Time period (***B***) **b**efore (***A***): it precedes the SPE onset and the related solar flare and can start several hours before the flare). Unusual and extremely big E_z oscillations can be observed during period (***B***). No obvious agent of sun-earth links presents in this case.

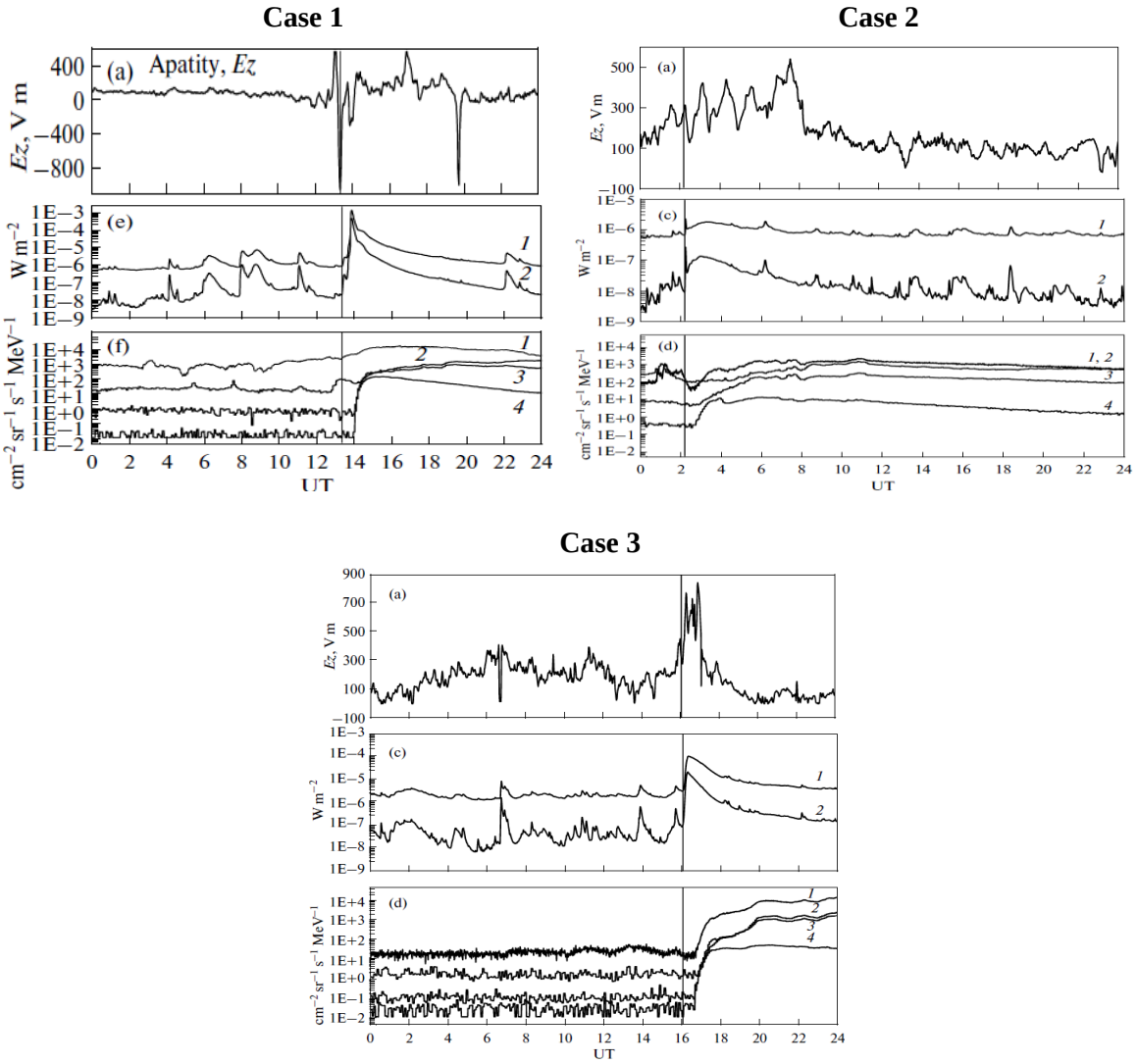

Figure 1. *Results from measurements in Apatity of AEF E_z response to three SPE/GLE in 2001: on 15.04 (case 1); 18.04 (case 2); and on 04.11 (case 3). For each case variations of E_z are presented in panels (a) (E_z >0 corresponds to downward Ez orientation). Panels (b) show X-ray variations in ranges 1–8 Å (curve 1) and 0.5–4 Å (curve 2). Panels (c) are for integral fluxes of E>2 MeV electrons (curve 1), and protons of energies E>1 MeV, E>10 MeV, and E>100 MeV (curves 2-4, respectively) from GOES-10 data) [Shumilov et al., 2016].*

During time period (***A***) (**a**fter the SPE onset) the following main peculiarities take place:

1. There are two separate phases of E_z variations which approximately correspond to the rise and decay phases of SPE: 1) During its first phase E_z is positive (downward) and has unusually large and fast variations; 2) On the second phase E_z reaches much smaller positive peaks, but can have reversals to upward direction with unusually high peaks reached.

2. During the first phase of SPE AEF Ez reaches extremely large (several times bigger than the usual ones) and persisting (indication for non-transient variations) positive values.

i) In case 1 (15 April): a) soon after the onset of SPE at ~1400 UT AEF E_z reaches a double peak larger than 300 V/m; b) at ~1650 UT E_z rises above 600 V/m. Large E_z peaks persist for more than half an hour, thus indicating for non-transient variations.

ii) In case 2 (18 April) E_z has four separate peaks close to or larger than 400 V/m before reaching its mean peak, E_{zp}>500 V/m.

iii) In specific case 3 (4 November) AEF E_z reaches two large peaks on the first phase: ~400 V/m and ~300 V/m at 1700 and 1750 UT, respectively.

3. On the second phase of AEF variations E_z can reverse to upwards (E_z<0) and reach extremely large negative values. The following peculiarities are observed:

i) In case 1 the second phase begins at ~1730 UT. E_z becomes upward for ~20 minutes (seemingly, non-transient variation) and reaches a negative peak value −1 kV/m at 1945 UT;

ii) In case 2 the second phase begins close after 0800 UT. Close before midnight E_z has small transient reversal to upward direction;

iii) In case 3 the second phase begins after 1800 UT; E_z exhibits a series of reversals.

3. Possible hypothetical interpretation of peculiarities

According to classical theory of the global atmospheric electrical circuit (GEC) [Rycroft, 2012], AEF in cases 1-3 should be oriented downwards and should not exceed 150-200 V/m, since no local thunderstorm activity or electrified clouds take place. But actually, E_z large variations and E_z reversals strongly impair these theoretical limitations. The enumerated peculiarities do not seem to be result of local factors. On the other hand, SPE can affect parameters of GEC, schematically represented in Figure 2, due to ionization at polar and high latitudes which leads to modification of conductivity σ. Significant effect of SPE on conductivity at these latitudes takes place only above about 20-30 km, so that only the partial columnar resistance $r_{PH} = r_{PS} + r_{PM} + r_{PA}$ (Figure 2) can be affected. However, since $r_{P2} << r_P$, the r_{P2} change would affect the total resistance $r_P = r_{PT} + r_{PH}$ negligibly; also, modification of E_z can be up to 5% [Farrell and Desch, 2002].

To resolve the discrepancy between experimental data and theory we propose hypothetic generalized picture of physical processes excited during SPE which can have much stronger effects on AEF at polar and high latitudes than the predicted by [Farrell and Desch, 2002]. Two principal processes are considered: *i*) accumulation of large uncompensated electric charge (UC) in GEC; *ii*) dramatic decrease of conductivity in specific layers above ~40 km caused by: *a*) creation and growth of aerosol particles (AP), *b*) transportation of ions and charged APs caused by electric fields. Process *i*) is result of penetration of protons into atmosphere. The elementary positive charges, thus injected into atmosphere, cannot leave back to the magnetosphere because of the insufficient energy of their carriers after protons' energy loss. The total positive UC accumulated in atmosphere during a strong SPE can be significantly larger than the total electric charge in GEC [Tonev, 2021]. Additional electric fields and currents can be generated in GEC due to UC redistribution which can play role in *b*) and can explain the peculiarities in AEF at ground level. Processes *i*) and *ii*) occur in specific atmospheric layers at polar and high latitudes simultaneously with, and stimulated by the enhanced ionization during SPE.

The hypothetical assumption for strong decrease of conductivity σ in specific atmospheric layers above ~40 km during SPE is supported by experimental measurements. An evidence for severe drop of σ in layer L_S 45-57 km at high geomagnetic latitudes is demonstrated on the base of rocket-borne measurement data for the profile of vertical electric field E_z in strato/mesosphere at a late phase (54.5 hours from the onset) of the major SPE from 19 October 1989 [Zadorozhni and Tyutin, 1998]. The conductivity σ in layer L_S is estimated to be of the order of magnitude as low as $\sim 10^{-15}$ S/m [Tonev, 2021]. Such decrease of σ in layer L_S determines that $r_{??} >> r_T$, and thus, significant increase of the total columnar resistance r. [Zadorozhni, 2001] consider the formation of aerosol particles to explain the decrease of σ.

[Holzworth and Goldberg, 2004] found from rocket-borne data in a noctilucent cloud around ~81 km altitude in noctilucent clouds in mesopause unusually large vertical electric field E_z which indicates for extremely low conductivity there (4×10^{-12} S/m). They assumed

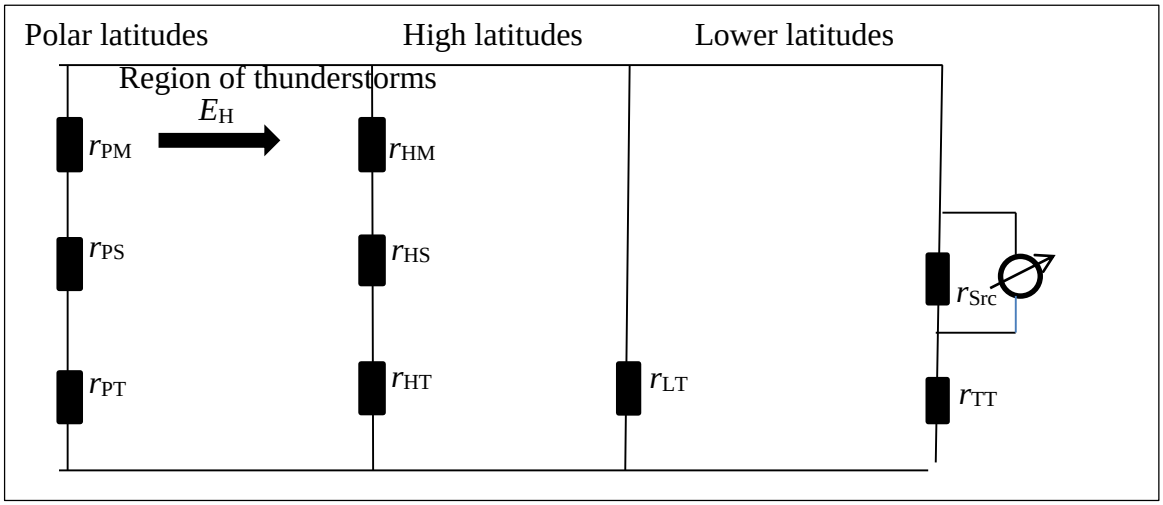

***Figure 2**. Equivalent GEC during SPE. Vertical links are for polar, high, and lower latitudes; and region of troposphere electric activity. r_* are partial columnar resistances with first index P/H/L for latitude, and second index T/S/M for troposphere/ strato- and mesosphere. SPE can lead initially to increase of r_{PM} to value $>r_{PT}$, and next to increase of r_{HM}, r_{PS}, and r_{HS}.*

that this decrease is caused by aerosol particles readily created in summer mesopause where ice crystals play role of nuclei. [Shumilov et al., 1996; Mironova and Usoskin, 2014] find experimentally appearance of aerosol particles in stratosphere after (tens of hours) SPE.

We assume that at initial phase of SPE creation and growth of APs is intensified gradually in an atmospheric layer L_{AP} at polar latitudes where the processes *i*) and *ii*) are active. Layer L_{AP} is initially presented mainly by the polar mesopause. Formation of an AP originates from a cosmic dust particle or a water ice crystal playing role of nuclei. Creation of an AP is determined mainly by the coefficients of attachment β_* to it of smaller particles of different type: neutral molecules (β_{nir}), electrons (β_{eir}), positive and negative ions ($\beta_{\pm ir}$), and larger particles (neutral or carrying electrical charge). These coefficients depend on the AP's size determined by the AP's radius *r*, and on the number of elementary electric charges *i* carried by AP ($i>0$ if charges are positive, and vice-versa; $i=0$ for neutral AP), $-m \le i \le m$ where *m* is the maximum number of charges carried by AP. *m* depends on the AP's size; we accept that *m* increases proportionally with the surface of AP, i.e. with r^2. Further, we hypothesize that in layer L_{AP} the attachment coefficients β_* significantly increases during SPE under the applied electric field E_H (Figure 2) which causes the initial slow growth of APs. By neglecting the detachment from APs we assume stable APs whose life is from many hours to few days: usually longer than the time period of interest of processes *i*), *ii*). Also, the gravitational sedimentation of APs is slow and can be neglected. We describe approximately further growth of an AP with time *t* by the equation:

$$dV_{AP}/dt = \gamma_0 S_{AP} \quad (1)$$

Here V_{AP} is the AP volume, S_{AP} is its surface, γ_0=const. According to Eq.(1), the attachment rate (cross-section) of a particle (molecule or ion) is proportional to the area of the AP's surface. By assumption for spherical AP we have $S_{AP} \sim 4\pi r^2$, $V_{AP} \sim 4/3\pi r^3$ where *r* is the AP's radius. In this case Eq.(1) is represented as an ordinary differential equation for *r* (here *r* is function of time *t*). Its solution yields linear increase of the AP radius *r* with time *t*:

$$r \propto t, \quad (2)$$

Then, the attachment coefficients will increase as t^2:

$$\beta_* \propto t^2, \tag{3}$$

and the increase of the AP mass m_{AP} will be as t^3. These simplest estimations concern neutral APs. If take into account the number i of its electric charges and its increase at least with r^2, as well as the fact that the AP and the smaller ionized particles are polarized in the applied electric field E_H, the increase of parameters r, β_*, m_{AP} will be faster, at least, according to:

$$r \propto t^2, \qquad \beta_* \propto t^4, \qquad m_{AP} \propto t^6 \tag{4}$$

under assumption that two polarized particles attach easier to each other. These estimations show that AP grows ever faster with time according to a strong positive feedback. Hence, we hypothesize that the density and average size of APs can increase enough in few hours during SPE in order to realize bite-outs of small ionized particles. In this case the time for attachment of electrons and ions to APs is quite short because of large coefficients β_*.

With the account of ionized APs the total conductivity σ is:

$$\sigma = \sigma_e + \sigma_+ + \sigma_- + \sum_{j=r_1}^{r_2} \sum_{i=-m}^{m} \sigma_{Aij} \tag{5}$$

Here σ_e, σ_+, and σ_- are conductivities of free electrons, and positive and negative ions. σ_{Aij} is conductivity of aerosol particles of (i,j) type where index j corresponds to the AP's radius r when it varies from r_1 to r_2; i shows the sign and number of elementary charges carried by the AP. The conductivity σ_s of charged particles of any type in Eq.(5) is represented in the form $\sigma_s = q_s \mu_s N_s$ where q_s is the amount of elementary charges carried, μ_s is the mobility of the particle reciprocal to its mass m_s, N_s is the particle number density. We note that the last term in Eq.(1) will be negligible under quiet conditions (without SPE) since the large mass of APs which determines their actual immobility ($\mu_s \sim 0$), as well as their low density. However, during SPE first three conductivities σ_e, σ_+, σ_- in (5) in layer L_{AP} can undergo dramatic decrease as result of decrease of their densities N_e, $N_\pm$, as predicted above, so that the total conductivity σ can drop to values many orders of magnitude smaller than usually: the relative absence of small ions and the large AP mass determine extremely low σ. As result of the drastic drop of σ the resistance r in GEC (Figure 2) can increase sufficiently to become dominant in the total columnar resistance r_P. In such case downward electric field E_A and current J_A in atmosphere below layer L_{AP} will be generated by the positive UC accumulated in L_{AP}. The AEF E_z below layer L_{AP} will be:

$$E_z = E_{z0} + E_A > E_{z0} \tag{6}$$

where E_{z0} is the electric field under quiet conditions. This case corresponds to the first phase of AEF variations considered in Section 2 and explains it. During the second phase of declining SPE there are periods when conductivity σ in layer L_{AP} recovers to larger values which leads to fast drop of resistance $r_{HM} + r_{HS}$. This causes rearrangement of atmospheric spatial charges and of electric currents. This can yield reversals of the electric field E_A at ground level to large enough negative values to obtain upward total electric field E_z.

Another effect of SPE considered here is the gradual extension of layer L_{AP}, controlled by electric field E_H, to lower latitudes (i.e. it comprises high latitudes besides polar latitudes). The result is generation of an additional electric field E_A also at these lower latitudes, and validity of the upper conclusions for variations of the total AEF E_z.

4. Analysis of AEF variations before SPE

Main peculiarities of AEF E_z in time period ***B*** are extremely large and unusual E_z fast oscillations with AEF reversals to upward direction ($E_z < 0$). In case 1 E_z oscillates from 1300 UT until 1410 UT between extremely large positive ($E_z > 600$ V/m) and negative ($E_z \sim -1.1$ kV/m) values. In case 2 E_z oscillations are smaller, between 100 and 320 V/m, one hour before the solar flare. In case 3 E_z oscillations have large amplitude between +100 and +850 V/m, and occur from 1600 UT (solar flare time) until 1705 UT (before the proton flux rise). We also note the significant X-ray variations, especially in cases 1 and 3 which, in general, may be an indicator for unknown processes on sun preceding solar flare and affecting earth.

These peculiarities cannot be explained by theory of GEC. They resemble those during SPE, however E_z multiple fast oscillations are typical for time period ***B*** with larger amplitudes (>1 kV/m). They can be interpreted as conducted by similar mechanism, as the described one n Section 3 for time period ***A***, but under assumption that energetic electron precipitation takes part at polar latitudes. The proposed mechanisms for both ***A*** and ***B*** time periods are subject of our future publications.

Conclusions:

- Atmospheric electric field E_z at geomagnetic latitude 63.8° (Apatity) during three GLE in 2001 (on 15.04, 18.04, and 04.11) show peculiar variations during solar proton event (SPE), as well as in long time period before SPE.

- During SPE two phases of typical AEF behavior are discriminated: *i*) in first one E_z is downward and reaches unusually large (600 V/m) peaks; *ii*) in the second phase AEF E_z can have alternating direction with extremely large (~ –1 kV/m) upward peaks;

- AEF peculiar modifications during SPE are hypothetically interpreted as result of accumulation of uncompensated electric charge in the polar and high-latitude atmosphere, and of creation, growth, and charging of aerosol particles, and their transportation, together with extreme increase of the average mass of charge carriers.

- Before SPE E_z demonstrates big oscillations which hypothetically can be result of EEP.

References

Farrell, W.M., Desch, M.D. (2002). Solar proton events and the fair weather electric field at ground, Geophys. Res. Lett., Vol 29, No 9, pp. 1323- 1326, DOI: 10.1029/2001GL013908.

Holzworth, R.H. and Goldberg, R.A. (2004). Electric field measurements in noctilucent clouds. J. Geophys. Res. 109: doi: 10.1029/2003JD004468.

Mironova, I. A., I. G. Usoskin (2014). Possible effect of strong solar energetic particle events on polar stratospheric aerosol: a summary of observational results, Environ. Res. Lett. 9 (2014), doi:10.1088/1748-9326/9/1/015002

Rycroft, M.J., K. A. Nicoll, K. L. Aplin, R. G. Harrison (2012). Recent advances in global electric circuit coupling between the space environment and the troposphere, J. Atmos. Solar-Terr. Phys., 90–91 (2012), 198–211, http://dx.doi.org/10.1016/j.jastp.2012.03.015

Shumilov, O. I., E. A. Kasatkina, K. Henriksen, E. V. Vashenyuk (1996). Enhancement of stratospheric aerosols after solar proton event, Ann. Geophysicae 14, 1119-1123 (1996).

Shumilov O.I., Kasatkina E.A., A. V. Frank-Kamenetsky (2015). Effects of Extraordinary Solar Cosmic Ray Events on Variations in the Atmospheric Electric Field at High Latitudes, Geomag. Aeron., 2015, Vol. 55, No. 5, pp. 666–674 doi: 10.1134/S0016793215050151.

Tonev, P.T. (2021). Detecting Common Origin of Atmospheric Electric Responses during SEP, Proc. 13-th Workshop "Solar Influences on the Magnetosphere, Ionosphere and Atmosphere", Primorsko, Bulgaria, 13-17 September, 2021.

Zadorozhny, A.M., A.A. Tyutin (1998). Effects of geomagnetic activity on the mesospheric electric fields, Ann. Geophys. 16, 1544–1551, 1998.
[EEP Polar]

Zadorozhny, A.M. (2001). Effects of charged dust on mesospheric electrical structure, Adv. Space Res. Vol. 28, No. 7, pp. 1059-1064, 200l.

Open Access Database for Different Types of Solar Wind

Asenovski S., Georgieva K., Kirov B.

Space Research and Technology Institute - Bulgarian Academy of Sciences, Sofia, Bulgaria
e-mail: asenovski@space.bas.bg

Abstract.

The presented open access database summarizes different types of solar wind and their duration in the near-Earth space, including high-speed solar wind streams and slow solar wind. The categorization of the different flows is based on criteria related to experimental data of the main solar wind parameters. The database uses physical conditions to clearly define the beginning and end of each event. The aim of this database is to cover the last four 11-year solar cycles (cycles 20 to 24 and partially 25) for which there are in situ satellite observations.

Keywords: *Open acces database, solar wind types.*

1. Introduction

Research related to space weather and space climate is based on available experimental data on solar activity, solar wind parameters, and geomagnetic activity. At present, several catalogs and databases exist for various aspects of solar activity:

- Hess & Zhang ICME-CME catalog (Hess and Zhang, 2017) - Available at http://solar.gmu.edu/heliophysics/index.php/GMU_CME/ICME_List/.
- Richardson & Cane ICME Catalog (Richardson and Cane, 2010) - Available at http://www.srl.caltech.edu/ACE/ASC/DATA/level3/icmetable2.htm.
- USTC ICME Catalog (Chi Y. et al., 2016) - Available at http://space.ustc.edu.cn/dreams/wind_icmes/.
- Jian's ICME and CIR Catalogs - Available at http://www-ssc.igpp.ucla.edu/~jlan/ACE/Level3/.
- Lepping & Wu MC and MCL lists (Lepping and Wu, 2010): Available at https://wind.nasa.gov/mfi/mag_cloud_pub1.html.
- Yermolaev's large scale solar wind phenomena catalog (Yermolaev Y.I., et al. 2009)- Available at ftp://www.iki.rssi.ru/pub/omni/.
- NASA - OMNI database (King and Papitashvili, 2005; Papitashvili et al., 2020).
- Data Analysis Center for Geomagnetism and Space Magnetism, Geomagnetic Equatorial Dst index, Kyoto University (Ahn et al., 2002) – Available at https://wdc.kugi.kyoto-u.ac.jp/dstdir/.

The information related to the various manifestations of solar activity is in large quantity and is constantly supplemented with new experimental data in these catalogues and databases. However, a complex approach is required for a number of studies, considering, for example, different types of solar wind simultaneously with geomagnetic disturbances. This was essentially the motivation for the creation of an open-access database that combine three main types of solar wind - the slow solar wind, High speed solar wind streams (HSS) and Coronal mass ejections (CMS) along with solar wind parameters, geomagnetic indices, sunspot numbers f10.7 and etc. The identification of the various solar events themselves will be based on the criteria already established. All identified events, as well as information on geomagnetic and ionospheric disturbances of various magnitudes, will be entered into a freely accessible database that will allow relatively easy access and rapid processing. This database will cover the last five 11-year solar cycles (cycles 20 to 24 and the beginning of 25) for which in situ satellite observations are available.

2. DATABASE for different solar wind types

The freely available database of the various manifestations of solar activity, including the slow solar wind, High speed solar wind, and Coronal mass ejection, can be accessed at the following address: https://spaceclimate.bas.bg/SW/catalogs.php.

In order to create a model of the catalog that meets the requirements of easy data processing, implementation of a suitable search engine, and at the same time a clean and sufficiently well-structured interface, extensive research was conducted on similar catalogs and databases on the Internet. The positive and negative sides of the investigated databases were systematized. From the point of view of quality-assured operational work with the database, a search engine was developed, through which it is possible to search for the individual physical parameters of the solar wind according to various criteria.

The database layout for searching individual solar wind events, was developed and structured as follows:

A) Search engine for solar cycle determination (***Fig. 1***)

Figure 1. *Interface of the DATABASE for Different Solar Wind Types.*

This featured search engine consists of 6 buttons that structure the available data into six 11-year solar cycles for the period from 1964 to 2022.

B) Detailed search for the available solar parameter data (***Fig. 2***)

After selecting data for a particular solar cycle, an active page opens with an implemented search engine pointing to the available experimental data for solar wind parameters. The search is performed by activating the "Add condition" button. The next step is to select the number and type of parameters to search for.

The search engine allows you to choose between 1 and all available parameters for the search. For each parameter, a specific condition can be entered to match the data.

C) Data visualization (***Fig. 3***)

Data visualization is actively linked to the search engine. After entering the numerical conditions for the various solar parameters as well as the time period, the average daily data corresponding to these conditions are visualized directly below the search engine. These data are displayed in tabular form. The size of the table can be additionally adjusted.

In detail, the database contains the following information: The first four columns correspond to the time range, respectively the first column gives information about the year (YEAR), the second about the day of the year (DOY), the third about the month (Month) and the fourth about the day of the month (Day). The fifth column (SW type) gives information about the type of solar wind (fast solar wind, slow solar wind and coronal mass ejections). The following columns

of the table visualize experimental data for different parameters of the solar wind and are respectively - properties of the magnetic field (scalar B [nT], Bx [nT], By [nT], Bz [nT]), the temperature (Temperature [K]), density (Density [N/cm^3]), speed (Speed [km/s]), pressure (Flow pressure), plasma beta (Plasma betta). Experimental data for geomagnetic indices (Kp index, Dst index [nT], ap index [nT], AE index [nT]) are also shown at the end of the table.

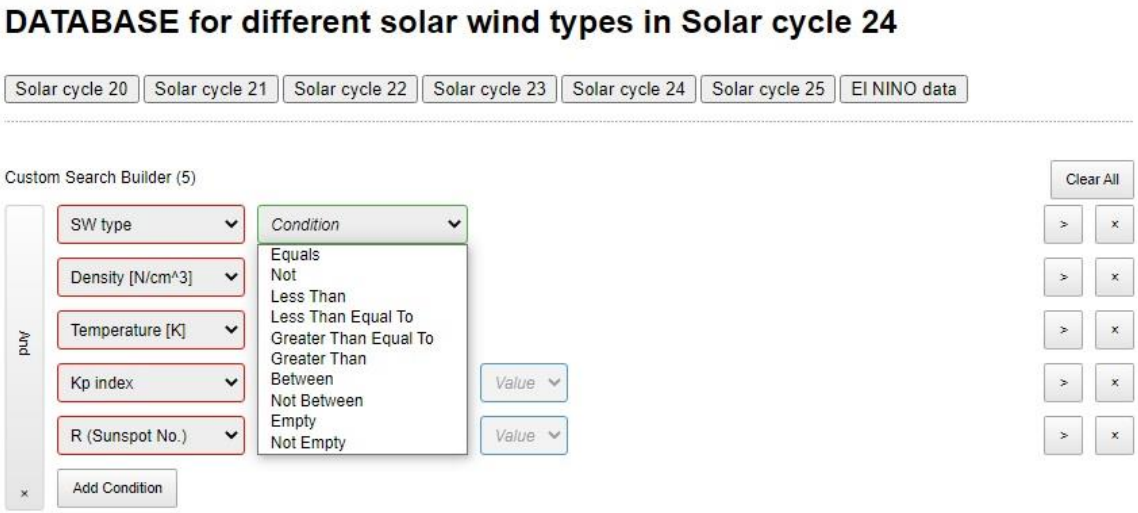

Figure 2. *Custom search builder.*

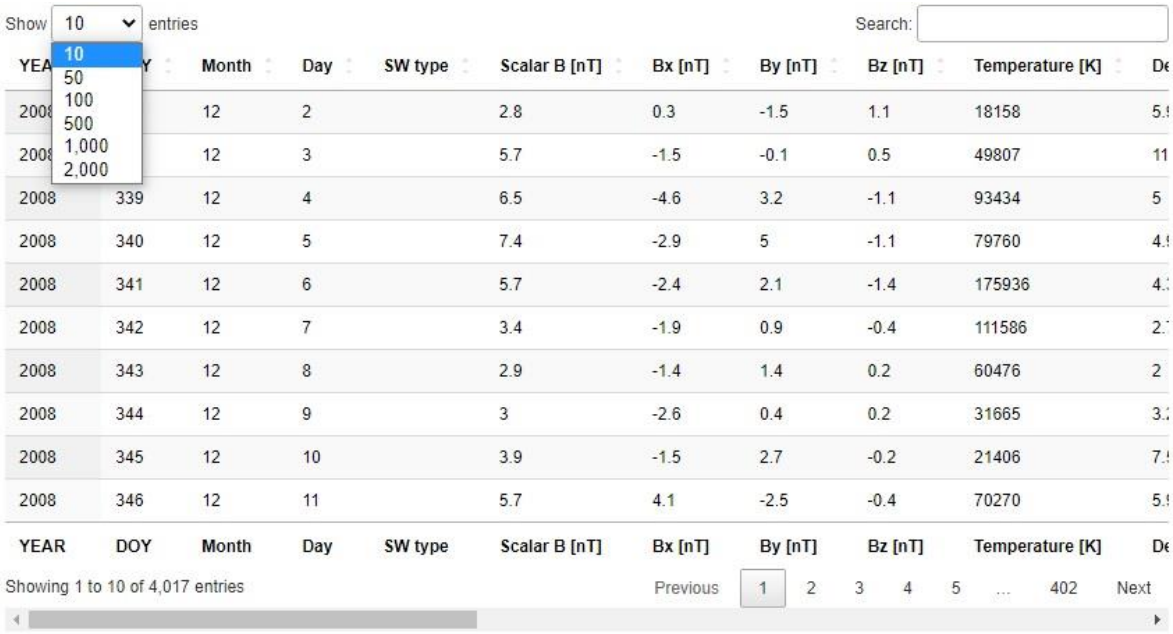

Figure 3. *Custom search builder.*

D) Download data

The system allows the visualized data to be downloaded in "*.csv" format.

The current filling of the catalog with raw data on solar activity, solar wind parameters, and geomagnetic activity follows the analysis of free experimental data and the application of criteria for determining solar wind fluxes. The data composing the catalog of solar events are contained in a suitable format on the server configuration storage space. The main source of

data related to solar wind parameters, sunspot numbers and part of geomagnetic indices is the database NASA:
- https://omniweb.gsfc.nasa.gov/form/dx1.html
The data for the geomagnetic indices Dst and AE are used from the Kyoto College database:
- https://wdc.kugi.kyoto-u.ac.jp/dstdir/

Conclusions

An open-access database of three types of solar wind fluxes and their associated solar plasma parameters and geomagnetic indices is presented.

The data presented are average daily values. Before being included in the database, the raw data are analyzed and the physical criteria developed to determine the periods of the various solar events are applied.

Acknowledgements

This study is supported by the National Science Fund of Bulgaria, Contract KP-06-N44/2 /27-11-2020 "**Space weather over a period of the century solar activity descending**".

References

Ahn, B.-H., G.-H. Moon, W. Sun, S.-I. Akasofu, G. X. Chen, and Y. D. Park (2002), Universal time variation of the Dst index and the relationship between the cumulative AL and Dst indices during geomagnetic storms, J. Geophys. Res., 107(A11), 1409, doi:10.1029/2002JA009257.

Chi, Y., Shen, C., Wang, Y. et al. Statistical Study of the Interplanetary Coronal Mass Ejections from 1995 to 2015. Sol Phys 291, 2419–2439 (2016). https://doi.org/10.1007/s11207-016-0971-5.

Hess, P., Zhang, J. A Study of the Earth-Affecting CMEs of Solar Cycle 24. Sol Phys 292, 80 (2017). https://doi.org/10.1007/s11207-017-1099-y.

King, J.H. and N.E. Papitashvili, Solar wind spatial scales in and comparisons of hourly Wind and ACE plasma and magnetic field data, J. Geophys. Res., 110, A02104, 2005, http://dx.doi.org/10.1029/2004JA010649.

Lepping C. C. Wu, Selection effects in identifying magnetic clouds and the importance of the closest approach parameter, Ann. Geophysicae, 28,1539-1552, 2010, www.ann-geophys.net/28/1539/2010/.

Papitashvili, N. E. and King, J.H. (2020), "OMNI Daily Data" [Data set], NASA Space Physics Data Facility, https://doi.org/10.48322/5fmx-hv56, Accessed on (DATE).

Richardson, I.G., Cane, H.V. Near-Earth Interplanetary Coronal Mass Ejections During Solar Cycle 23 (1996 – 2009): Catalog and Summary of Properties. Sol Phys 264, 189–237 (2010).

Yermolaev, Y.I., Nikolaeva, N.S., Lodkina, I.G. et al. Catalog of large-scale solar wind phenomena during 1976–2000. Cosmic Res 47, 81–94 (2009). https://doi.org/10.1134/S0010952509020014.

A Comparison Between the Solar Activity in the 11-Year Sunspot Cycles During the Last Two Centennial Solar Activity Minima. A Comparison of the Geomagnetic Activity During the Same Periods

Kirov B.[1], Georgieva K.[1], Asenovski S.[1], Madjarska M. S.[1], Dineva E.[2]

[1]Space Research and Technology Institute - Bulgarian Academy of Sciences, Sofia, Bulgaria
[2]Leibniz Institute for Astrophysics, Potsdam, Germany

Abstract.

When we talk about a change in solar activity, we usually mean a change in the number of sunspots which is known as the 11-year sunspot cycle. The beginning of the cycle is considered to be the time when there is a minimum number of sunspots which may be different for different cycles both in terms of duration and the number of sunspots. It is followed by an increase in the sunspot number until a maximum is reached, and a decrease again to the next minimum. This period lasts approximately 11 years. It has been established that there exists also a quasi-century-old cycle, called Gleissberg cycle. For about 100 years, the number of sunspots in the 11-year cycles changes with a gradual increase followed by a decrease and again an increase. For a long time, only the number of sunspots was a measure of solar activity. In the present work, we compare the number of sunspots in the different phases of penultimate 11-year solar cycles and compare them with the analogous period of the previous century minimum. We also study the development of geomagnetic activity in the indicated period of time.

1. Introduction

In the past, changes in climate were compared with the sunspot number [Sabine, 1852], and later with geomagnetic activity. It is now known that big sporadic (non-recurrent) geomagnetic storms are caused by coronal mass ejections (CMEs). The latter are related to the evolution of the solar toroidal field whose manifestations are sunspots. Thus during sunspot maximum, a maximum in geomagnetic activity is observed. Another source of geomagnetic activity are coronal holes, regions of the open unipolar magnetic field from which the high-speed solar wind emanates [Feynman, 1982]. Disturbances caused by high-speed solar wind are at maximum during the sunspot's declining phase, which leads to two geomagnetic activity maxima in the 11-year sunspot cycle.

2. Observational data

We compared the amplitudes of cycles 12, 13, 14, 23, 24, and 25 with the geomagnetic activity for the same period of time using the following indices:

1.The sunspot number (SSN). calculated by the Sunspot Index Data Center (https://www.sidc.be/silso/datafiles)

2. Geomagnetic index aa https://isgi.unistra.fr/indices_aa.php

3. ap index https://www.ngdc.noaa.gov/stp/geomag/kp_ap.html

3. Analysis and Results

3.1. Evolution of cycles 12 and 13:

Cycles 12 and 13 are the last two 11-year cycles in the preceding Gleissberg cycle. Naturally, their solar activity, measured by the number of sunspots, is lower than that in the middle of the Gleissberg cycle. Although the last cycle is 13, its activity is higher than that of the 12th cycle, but this is natural considering the Gnevishev-Ol rule that "every odd cycle is higher than the previous even cycle".

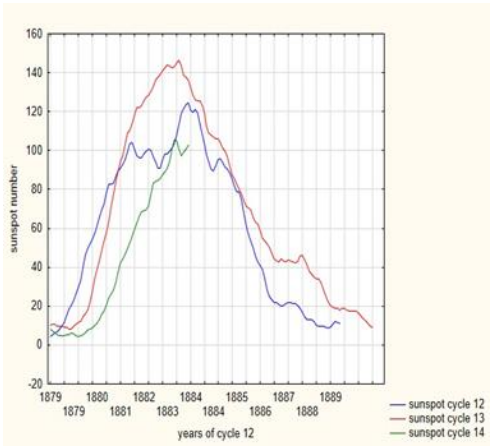

Figure 1. *Evolution of cycles 12, 13 and the beginning of 14.*

The next cycle, the 14th, almost repeats the development of cycle 12th (Fig. 1). after which a significant increase of the 11-year cycles begins. Therefore, we are possibly in one of the most powerful 100-year cycles.

3.2. Evolution of cycles 23 and 24

The period of the great maximum ends with cycle 23, for which the solar activity was the highest for several decades recorded by direct and indirect data in the last 8 thousand years (Solanki et al., 2004). The prolonged and deep minimum of solar activity in 2008-2009 (end of cycle 23 and beginning of 24) is generally considered to end this century-long maximum. Therefore, the question arises as to whether a Maunder-like minimum of solar activity awaits us. The completed 11-year cycle after it, as seen in Fig. 2, was significantly weaker than the previous one. The starting 25th cycle is predicted to be weaker than the previous cycle.

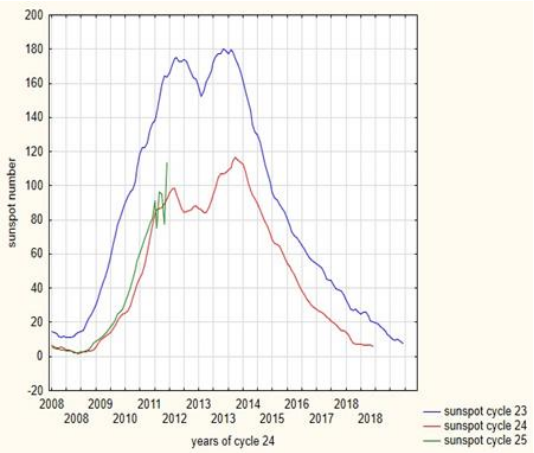

Figure 2. Evolution of cycles 23, 24 and the beginning of 25.

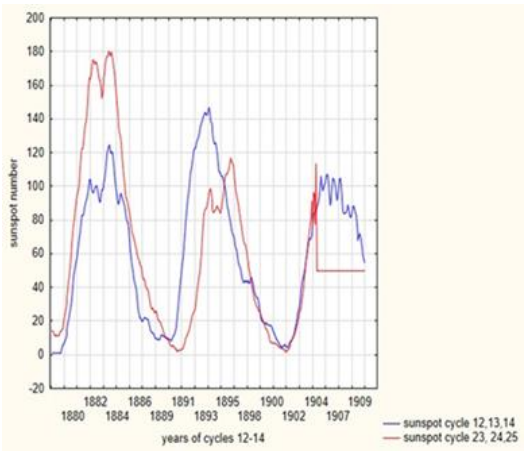

Figure 3. Evolution of cycles 23, 24 and the beginning of 25.

Based on the first data from this cycle, due to the relatively rapid increase in solar activity, it is believed that a significantly high maximum is expected. In fact, the rate of increase in solar activity is not significantly different from that of the 24th cycle, and it seems that these predictions are exaggerated. As it can be seen from Fig. 3, the 23rd cycle is significantly higher than cycle 12. These are the penultimate 11-year cycles in the respective 100-year cycles. However, the 13th cycle, in accordance with the rule of Gnevishev-Oll, is more powerful than

the 12th, while the 24th is significantly weaker than the 23rd which is a logical conclusion of the last Gleissberg cycle. While cycles 12 and 13 have single maxima, 23 and 24 have double maxim. As already shown by e.g. Georgieva [2011], the solar dynamo can operate in different regimes determined by the relative importance of diffusion and advection in the upper and bottom parts of the solar convection zone (e.g. Paul Bushby and Joanne Mason, 2004). Based on the estimations for the speed of the surface poleward meridional circulation and diffusion in the upper part of the convection zone, it has been demonstrated that the dynamo operates in a moderately diffusion-dominated regime, in which a part of the flux short-circuits the meridional circulation and diffuses directly to the bottom of the convection zone at mid latitudes. Another part makes a full circle to the poles, down to the base of the convection zone, and equatorward to sunspot latitudes. These two parts of the flux, when transformed by the differential rotation at the base of the convection zone, give rise to two peaks of sunspot activity, which are close but not exactly coinciding. In this way, the double-peaked sunspot cycle and the Gnevyshev gap have their natural explanation in the flux transport dynamo theory. Based on this, we can come to the conclusion that while during the 23rd and 24th cycles, the solar dynamo works in a moderately diffusion-dominated regime, the 12th and 13th are in the advection dominated regime.

The minimum solar activity in 2008-2009 (between the 23rd and 24th cycle) was extremely low and prolonged. This has led many scientists to wonder if the Sun is entering a new grand minimum. The present data the 25th cycle, however, do not show this trend.

3.3. Solar sources of geomagnetic activity

Since the beginning of geomagnetic research, it has been established that there is a relationship between the number of sunspots and the number of geomagnetic disturbances. However, as we know today, sunspots themselves have no effect on Earth, but the presence of more sunspots is associated with more CMEs (e.g. Lindsay G.M., et al. 1995). The latter cause powerful geomagnetic storms. In addition, there is another source of geomagnetic disturbances, namely high-speed solar wind flows, and their source are the so-called "coronal holes”.

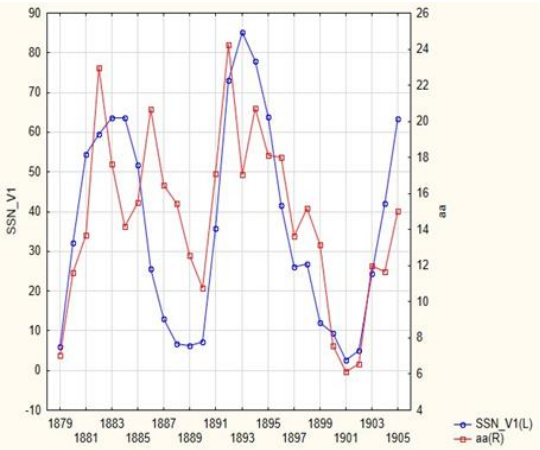

Figure 4. Geomagnetic activity during cycles 12, 13 and the beginning of 14.

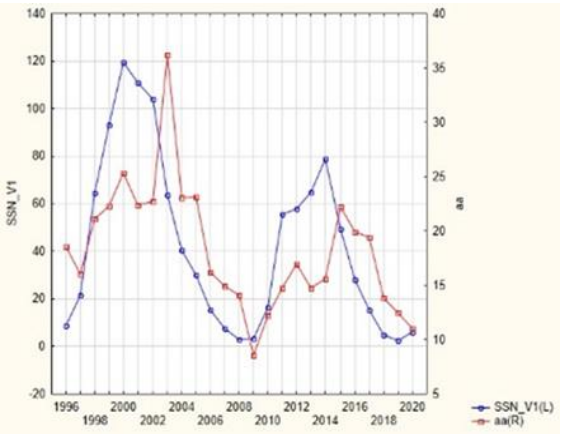

Figure 5. Geomagnetic activity during cycles 23 and 24.

Because most CMEs occur during solar activity maxima, and most geopotential coronal holes occur during the decline of the solar activity, the geomagnetic Fig. 4 Geomagnetic activity

during cycles 12, 13 and the beginning of 14 activity has two maxima during the solar cycle. Fig. 4 shows the geomagnetic activity against the sunspot number for cycles 12 and 13.

Looking at the same relationship, but for cycles 23 and 24 (Fig. 5), we see only one maximum of the geomagnetic activity during each of the cycles. This peak is observed to be during the decline of solar activity. This means that either the number of CMEs is not proportional to the number of sunspots or that the corresponding CMEs are not geoefficient.

3.4. How can we evaluate the relative influence of different types of solar activity on the Earth?

To establish the influence of various solar factors on the geomagnetic activity, Feynman examined the dependence of the aa index of geomagnetic activity on the number of sunspots and found that all values of aa lie above a straight line that obeys the equation:

$$aaR=a + b*R,$$

where R is the number of sunspots. According to Feynman, aaR is the geomagnetic activity due to the solar activity associated with sunspots. The values of aa above the line aaR (see Fig. 6) is the geomagnetic activity associated with the high-speed solar wind.

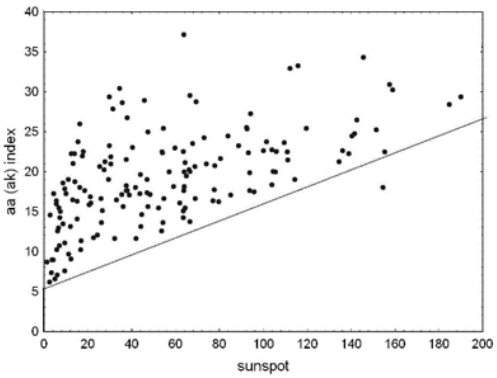

Figure 6. Dependence of the aa index of the sunspot number.

We introduce one additional term aamin, and so the geomagnetic activity at a given time is:

$$aa = aamin + aaT + aaP$$

- aamin - "floor" in geomagnetic activity
- aaT=b*R – geomagnetic activity due to sunspot-related solar activity
- b – sensitivity of geomagnetic activity to sunspot-related solar activity
- aap – geomagnetic activity due to non sunspot-related solar activity

The geomagnetic activity "floor" is the geomagnetic activity in the absence of any sunspots. Practically it is determined by the geomagnetic activity in the sunspot minimum. We can conclude that the geomagnetic activity "floor" is determined by non-sunspot-related solar activity.

We compare the geomagnetic activity with the number of sunspots for cycles 13 and 24 in Fig. 7 and 8, respectively. We see that the floor in cycle 13 is about two times lower than that in cycle 24, but on the other hand, the sensitivity of geomagnetic activity to the number of sunspots is significantly greater for cycle 13 than for cycle 24.

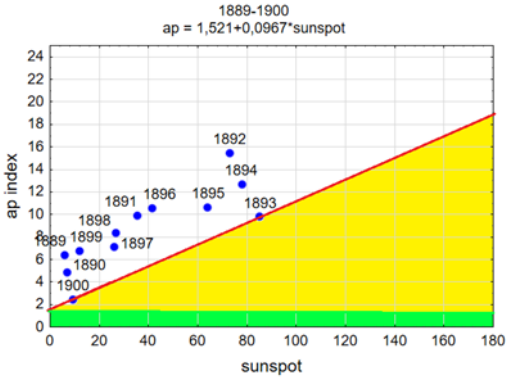

Figure 7. The same as Fig. 6 for cycles 12 and 13.

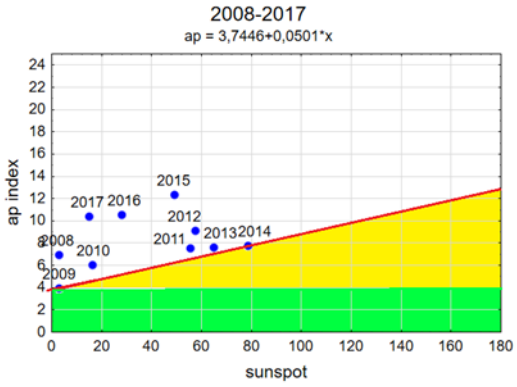

Figure 8. The same as Fig. 6 for cycles 23 and 24.

This once again confirms the conclusion that the solar dynamo operates in two different modes during cycles 12, and 13, and cycles 23 and 24.

Conclusions

The sunspot number at the beginning of cycle 25 follows the behaviour of the sunspot number in cycle 14. This is true for both the number and the rate of increase.

CMEs related to sunspots are less geoeffective during cycle 24. This is the reason for the weaker sensitivity of the geomagnetic activity to the number of sunspots.

During cycles 23 and 24, the solar dynamo works in a moderately diffusion-dominated regime, and during cycles 12 and 13, it is in an advection-dominated regime.

Acknowledgements

This study is supported by the National Science Fund of Bulgaria, Contract KP-06-N44/2 /27-11-2020 "**Space weather over a period of the century solar activity descending**".

References

Sabine E., "On Periodical Laws Discoverable in the Mean Effects of the Larger Magnetic Disturbances", Phil. Trans. R. Soc. Lond. January 1, 1852 142 103-124; doi:10.1098/rstl.1852.0009.

Feynman J., "Geomagnetic and solar wind cycles, 1900-1975", J. Geophys. Res. 87, 6153-6162 (1982).

Solanki S.K. et al., "Unusual activity of the Sun during recent decades compared to the previous 11,000 years", Nature, 431 (7012), 1084, 2004.

Georgieva K., "Why the Sunspot Cycle Is Double Peaked", International Scholarly Research Notices Volume 2011 | Article ID 437838.

Paul Bushby, Joanne Mason, "Understanding the solar dynamo", Astronomy & Geophysics, Volume 45, Issue 4, August 2004, Pages 4.7–4.13, https://doi.org/10.1046/j.1468-4004.2003.45407.x

Lindsay G.M., Luhmann J.G., Russell C.T., Gazis, P., Solar cycle variation of interplanetary shocks, coronal mass ejections, and stream interactions observed at 0.7 AU. Advances in Space Research 16 (9), 353-353, 1995.